

Dynamics Modeling and Conceptual Design of a Multi-tethered Aerostat System

by

Casey Marcel Lambert
BASc, University of Calgary, 1999


A Thesis Submitted in Partial Fulfillment of the
Requirements for the Degree of

MASTER OF APPLIED SCIENCE


in the Department of Mechanical Engineering.

We accept this thesis as conforming
to the required standard


Dr. M. Nahon, Supervisor (Dept. of Mechanical Engineering)


Dr. C. Bradley, Departmental Member (Dept. of Mechanical Engineering)


Dr. R. Lueck, Outside Member (Dept. of Earth and Ocean Sciences)


Dr. J.S. Collins, Outside Member (Dept. of Electrical Engineering)


Dr. P. Dewdney, External Examiner (National Research Council)

© CASEY MARCEL LAMBERT, 2002
University of Victoria

All rights reserved. This thesis may not be reproduced in whole or in part, by photocopy
or other means, without permission of the author.

Supervisor: Dr. M. Nahon

Abstract

Canadian researchers have proposed a design concept for a new radio telescope which uses a large multi-tethered aerostat to support and position the telescope's receiver. Based on encouraging results from an initial dynamics analysis of the system, it was decided to build a one-third scale experimental model of the system for further study. This work focuses on the development of both the dynamics model and the physical design of the scaled experimental system. The dynamics analysis began by scaling the original system using a dimensional analysis to ensure dynamic similarity. Several modifications were made to the dynamics model, broadening its capabilities and improving its approximation of the real system. These included accurate estimation of tether damping properties through experimental methods, the addition of vortex shedding oscillations with the spherical aerostat and the incorporation of a streamlined aerostat. A linear stability analysis of the streamlined aerostat was conducted. The conceptual design of the experimental system is also presented. The selection of the aerostat and tethers was based on choosing available components that provided the most favorable performance. A winching system for the tethers was designed based on results from the dynamics model.

Examiners:



Dr. M. Nahon, Supervisor (Dept. of Mechanical Engineering)



Dr. C. Bradley, Departmental Member (Dept. of Mechanical Engineering)



Dr. R. Lueck, Outside Member (Dept. of Earth and Ocean Sciences)



Dr. J.S. Collins, Outside Member (Dept. of Electrical Engineering)



Dr. P. Dewdney, External Examiner (National Research Council)

Table of Contents

Abstract	ii
Table of Contents	iv
List of Figures	vii
List of Tables	xi
Acknowledgements	xiii
1 Introduction	1
1.1 Background	1
1.2 Related Work.....	5
1.3 Research Focus.....	7
2 Dynamics Model	9
2.1 Original Dynamics Model.....	10
2.2 Scaling of Full Scale LAR System.....	13
2.2.1 Dynamic Similarity	14
2.2.2 Dimensional analysis.....	14
2.2.3 Reynolds' Number Scaling	18
2.2.4 Froude Number Scaling	20
2.2.5 Simulation Results.....	21
2.3 Tether Damping.....	25
2.3.1 Theory	25
2.3.2 Experimental Procedure	27
2.3.3 Results.....	29
2.4 Vortex Shedding of a Spherical Aerostat.....	33

2.4.1	Amplitude of Oscillation.....	35
2.4.2	Frequency of Oscillation	37
2.4.3	Applying the Oscillation to Dynamics Model.....	39
2.4.4	Results for Single-tether System	41
2.4.5	Results for Multi-tethered System	43
2.4.6	Minimizing Region Where Vortex Shedding is Observed.....	49
2.5	Dynamics of a Streamlined Aerostat.....	50
2.5.1	Equations of Motion.....	52
2.5.2	Component Breakdown Method	54
2.5.3	Aerodynamic Forces of the Fins	57
2.5.4	Aerodynamic Forces of the Hull	60
2.5.5	Added Mass.....	64
2.5.6	Tether Attachment.....	64
2.5.7	Physical Parameters.....	67
2.5.8	Results	72
3	Linear Stability Analysis	76
3.1	Linear Model	77
3.2	Decoupling	80
3.3	Eigenvalues and Eigenvectors.....	81
3.4	Results	83
3.4.1	Reference Frequencies	88
3.4.2	Performance Analysis	91
4	Experimental System Design	101
4.1	Aerostat	102
4.1.1	Aerodynamic Performance.....	102
4.1.2	Survivability	106
4.1.3	Cost and Availability.....	107
4.1.4	Ground Handling.....	108
4.1.5	Aerostat Selection	109
4.2	Tether Selection.....	109

4.2.1	Tether Materials	110
4.2.2	Tether Size.....	111
4.2.3	Tether Length and Layout.....	113
4.3	Instrument Platform.....	115
4.4	Winch Design.....	117
4.4.1	Tether Motion and Tension.....	117
4.4.2	Drive Components.....	124
5	Conclusions	146
5.1	Dynamics Model	146
5.2	Experimental System Design	149
5.3	Recommendations	151
	References	152
	Appendix A Arrangement of Dynamic Parameters into Dimensionless Terms	157

List of Figures

1.1: Artist's rendition of the LAR concept. A single reflector section and the receiver package are shown at the bottom of the figure.....	2
1.2: Tethered aerostat positioning system.	3
2.1: Discrete implementation of tethered aerostat dynamics model.	10
2.2: Schematic of visco-elastic internal forces for the tether model.	11
2.3: Control terminology.	12
2.4: Simulation results; error of receiver in and out of the focal plane and tether tension, for scaled model and prototype, using Re scaling.	23
2.5: Simulation results; error of receiver in and out of the focal plane and tether tension, for scaled model and prototype, using Fr scaling.....	24
2.6 Typical response with viscous damping.....	26
2.7: Experimental apparatus; a) rope attachment assembly with S-type load cell, b) full system with cement weight attached to tether.....	28
2.8: Sample of experimental results for tether test.....	30
2.9: Log of the peak tensions for case with $L = 1.775$ m and $m = 186$ kg.	30
2.10: Elongation vs. stress for Plasma 12 Strand from Puget Sound Rope [29].....	32
2.11: Tethered aerostat.	35
2.12: Normalized root-mean-square (y_{rms}/D) of transverse oscillations versus reduced velocity (V_R) for two mass ratios $M^* = 0.26(\Delta)$ and $M^* = 0.76(O)$ from [10].	37

2.13: Transverse oscillation frequency (f/f_n) versus reduced velocity (V_R) for $M^* = 0.76$. Also plotted for comparison, is the vortex shedding frequency of a sphere from Sakamoto and Hainu (1990) [10].....	38
2.14: Sinusoidal force amplitude related to wind speed.....	41
2.15: Aerostat position and tether tension for single tethered system with vortex shedding oscillations with $U = 6$ m/s.	42
2.16: Error of the payload and tether tension for tri-tethered system with vortex shedding effects, $U = 6$ m/s.....	44
2.17: Error of the confluence point and tether tension for multi-tethered system with and without vortex shedding, with turbulence and no active control, $U = 6$ m/s.	46
2.18: Error of the payload and winch power for multi-tethered system with and without vortex shedding, with turbulence and active control, $U = 6$ m/s.	48
2.19: a) Aeros Flightcam 21M aerostat, b) proposed aerostat for scaled system.....	51
2.20: Inertial and body-fixed coordinate frames for aerostat system.	52
2.21: Front and side view of aerostat with location and orientation of local frame at the center of pressure of each fin.....	56
2.22: Angle of attack, α_i , and sideslip angle β_i , for an airfoil.	57
2.23: Lift and drag forces relative to fin motion.	59
2.24: Schematic of aerodynamic parameters.....	61
2.25: Aerodynamic parameters with M_{nose} replaced by forces applied at center of pressure.....	62
2.26: Orientation of the hull motion and forces.	64
2.27: Connection point of tether and aerostat.	66
2.28: Rotation of aerostat in no-wind condition.....	67
2.29: Aerostat with dimensions.....	68
2.30: Position and orientation of streamlined aerostat on a single tether with $L = 100$ m, $U = 6$ m/s with turbulence.....	74
2.31: Payload error and aerostat position for tri-tethered case, $U = 6$ m/s with streamlined aerostat with turbulence and active control.	75

3.1: Comparison of linear and non-linear simulation results of aerostat motion for case with single tether of $L = 300$ m tether and $U = 10$ m/s.	79
3.2: Complex representation of eigenvalue.	82
3.3: Longitudinal and lateral modes for baseline case with $L = 300$ m, $\theta_0 = -4^\circ$	84
3.4: Eigenvectors for 4 lowest frequency lateral modes: a) pendulum, b) rolling, c) 1st tether harmonic and d) 2nd tether harmonic for baseline case at $U = 1$ m/s.	85
3.5: Longitudinal and lateral modes for case with $L = 100$ m, $\theta_0 = -4^\circ$	96
3.6: Longitudinal and lateral modes for case with $L = 33.3$ m, $\theta_0 = -4^\circ$	97
3.7: Longitudinal and lateral modes for case with $L = 300$ m and $\theta_0 = -7^\circ$	98
3.8: Longitudinal and lateral modes for case with $L = 300$ m, $\theta_0 = -1^\circ$	99
3.9: Longitudinal and lateral modes for case with $L = 300$ m, $\theta_0 = -4^\circ$ and $(Cd_e)_h = 0.28$	100
4.1: Two variable lift aerostats; Skydoc above and Helikite below.	103
4.2: Testing of Skydoc aerostat in Hood River, Oregon, November 2000.	104
4.3: Top view of tether layout for configuration with $\theta_{ze} = 60^\circ$, $\theta_{az} = 180^\circ$ and $\theta_w = 180^\circ$	106
4.4: Simulation results for payload error and tether tension for three different leash lengths with $U = 6$ m/s in symmetrical configuration (i.e. $\theta_{ze} = \theta_{az} = \theta_w = 0^\circ$).	114
4.5: Top view of instrument platform with tether hanger fittings, wind speed and wind direction sensors.	115
4.6: Underside of instrument platform.	116
4.7: Top view of LAR layout; shaded portion of operating range represents region of study.	119
4.8: Tether speed, acceleration, tension and winch power for tether 1 with $P_{max} = 1.5$ kW, $\theta_{az} = \theta_{ze} = 60^\circ$, $\theta_w = 150^\circ$, $k_p = 5$, $k_i = 1.5$, $k_d = 1.5$ and $U = 6$ m/s.	123
4.9: Front and side view of winch drum with tether wraps.	125
4.10: Rotational speed and acceleration for drum 1 with $w_d = 305$ mm for case 1 with $P_{max} = 1.5$ kW.	128

4.11: Winch motor system.	129
4.12: Family of motors used for conventional motion control applications.	133
4.13: Speed vs. torque curves for servo motors manufactured by a) Parker Automation (one set of curves for different voltages) [28] and b) Yaskawa [35].	135
4.14: Schematic of PC based motion control system for aerostat positioning system.	144

List of Tables

2.1: Physical parameters of prototype tethered aerostat system.....	13
2.2: Relevant parameters for tethered aerostat system.....	15
2.3: Physical parameters for scaled model with consistent Re scaling.	19
2.4: Physical parameters for scaled model with consistent Fr scaling.....	20
2.5: The average experimental results for the damping and elastic parameters.....	31
2.6: Parameters for tethered aerostat.	35
2.7: Vortex shedding oscillation characteristics and trial and error force inputs.....	40
2.8: Aeros physical parameters.	69
2.9: Aerodynamic parameters of aerostat.....	70
2.10: Tether parameters.....	72
3.1: Lateral eigenvectors for low frequency modes of baseline case at $U=1$ m/s.....	86
3.2: Comparison of theoretical and linear model results for period, τ_n of certain oscillatory modes for baseline case.....	90
4.1: Desired scaled tether properties from Chapter 2.....	110
4.2: Properties for braided tethers of several materials [4][9].....	111
4.3: Maximum error, e_{max} (cm) / max power, P_{max} (kW) for cases with $\theta_{ze} = 60^\circ$ during 80 s simulation with $k_p = 5$, $k_i = 1.73$, $k_d = 1.73$ and $U = 6$ m/s.....	120
4.4: PID gains for worst case configurations for maximum power levels of 1.5 kW and 3 kW.	121
4.5: Winch performance parameters for case 1 with maximum power levels of 1.5 kW and 3.0 kW.....	122
4.6: Winch drum dimensions.	126
4.7: Winch drum characteristics for tether 1 of case 1 for different drum widths.	127

4.8: Comparison of the rms and peak motor speed, torque and power requirements for two drum widths.	131
4.9: Specifications for selected servo motors [28] [35].	136
4.10: Common gearing types for DC motors	138
4.11: Motor requirements with actual motor characteristics and multiple gear stages for maximum power case of 1.5 kW.	139
4.12: Motor requirements with actual motor characteristics and multiple gear stages for maximum power case of 3 kW.	140
4.13: Minimum gear ratio required for each motor at both power levels	141

Acknowledgements

I would like to express my sincere gratitude to Meyer Nahon for his continuous guidance and support during this research. I would also like to acknowledge and thank a number of co-op students who brought fresh ideas and enthusiasm to the project every four months. These students are Marco Shüpfer, Scott Bumpus, Stefan Depner, Rusty Rook, Dusty Moi and Neil Wyper. Without their help, the experimental system would never have gotten off the ground. Also, I would like to acknowledge my appreciation for the collaboration and guidance from Peter Dewdney of the Dominion Radio Astronomy Observatory (DRAO). Several others have made contributions to this research that I would like to personally thank, including Gabriele Gilardi, Xiaohua Zhao and James Harrington.

Funding for this project was provided by the Canadian Fund for Innovation (CFI) and the National Research Council (NRC). My personal funding was from the Science Council of British Columbia (SCBC).

To my Mom and Dad,
for getting me here

Chapter 1

Introduction

1.1 Background

The international radio astronomy community presently has a great interest in drastically improving the capabilities of radio telescope technology. To overcome the sensitivity limitations of conventional telescopes that prevent study of the early universe, it will be necessary to design a revolutionary instrument [33][22]. The primary feature of the new instrument is an increase in collecting area of over thirty times that of the largest radio telescope in existence. Because a project of this magnitude requires cooperation and contributions from several nations, an international consortium of radio astronomers and engineers was established for the goal of building such an instrument. The project and the instrument are commonly known as the square kilometer array (SKA) [32]. The instrument will be comprised of many radio telescopes functioning together as an array with a total of one square kilometer of collecting area.

The Canadian radio astronomy community, led by the National Research Council of Canada, has put forward a novel design concept for the large scale telescope [22] known as the large adaptive reflector (LAR) which is depicted in Figure 1.1 . The LAR concept consists of two central components. The first is a 200 m diameter parabolic reflector with a focal length of $R = 500$ m, composed of actuated panels supported by the ground. The second component is the receiver package which is supported by a tension structure consisting of multiple long tethers and a helium filled aerostat.

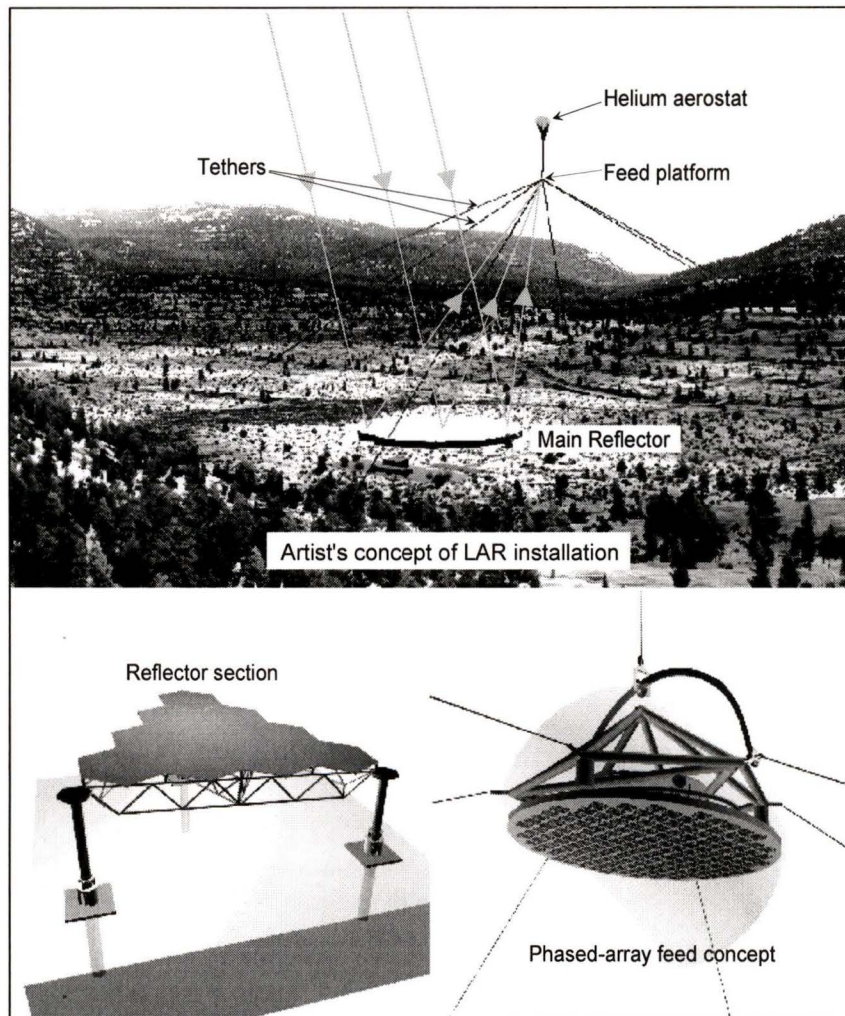


Figure 1.1: Artist's rendition of the LAR concept. A single reflector section and the receiver package are shown at the bottom of the figure [3].

The telescope can be pointed to different regions in the sky by simultaneously changing the lengths of the tethers and adjusting the orientation of the reflector panels. The focal length of the reflector is constant, and so the receiver will need to be positioned accurately at points on the hemispherical surface of radius R , centered at the midpoint of the reflector. For sufficient coverage of the sky, the system must be capable of positioning the receiver for a range of zenith angles from 0 to 60° ($0 \leq \theta_{ze} \leq 60^\circ$) for the full range of azimuth angles ($0 \leq \theta_{az} \leq 360^\circ$). A schematic of the layout of the tethered aerostat system is shown in Figure 1.2. The aerostat is attached to the payload/receiver by a single tether referred to as a leash, while the ground tethers run from winches on the ground up to the payload. The winches at the base of each tether are used to actively control the lengths of the tethers for the dual purpose of steering the receiver to a particular location and responding to disturbances such as wind gusts.

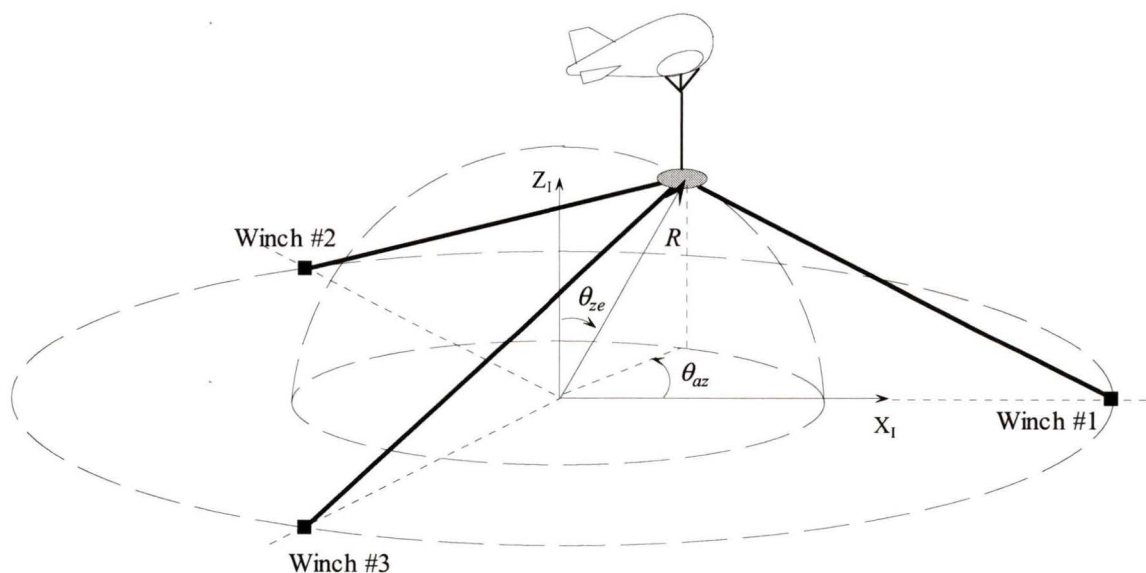


Figure 1.2: Tethered aerostat positioning system.

It is envisioned that the resulting tension structure is large enough to filter out all but the lowest frequency turbulence and also stiff enough to effectively resist wind forces. Preliminary investigations indicate that this telescope concept offers an order of magnitude reduction in cost per square meter of collecting area over traditional parabolic antennas [3]. This has inspired a proof of concept research phase involving many university researchers studying the various components. An initial investigation of the dynamics of the tethered aerostat system by Nahon presented encouraging results for the accuracy of the positioning system [25]. Based on the outcome of the initial research phase there was an agreement to proceed to a second and more detailed stage of analysis. Because the tethered aerostat positioning system is the most unconventional aspect of the LAR telescope and is thus the center of the uncertainty surrounding the viability of the concept, it was decided to pursue an experimental investigation of a scaled model of the tethered aerostat system.

There are two distinctly different goals for the study of the scaled system stemming from the uncertainty of both the dynamic positioning capability and the operational feasibility of the system. From a dynamics perspective, the goal of the scaled model is to measure the behavior of the system and compare the results with simulation results in attempt to validate the dynamics model. From an operational standpoint, the goal is to use the scaled model to study the logistics and feasibility of operating the tethered aerostat system. The results from both avenues of this effort will be critical for ascertaining the overall merit of the LAR concept. In order to satisfy both objectives, it was decided to construct the scaled system at one-third the size of the full system. This

size was chosen by striking a balance between the conflicting agendas of economics and practicality versus credibility.

1.2 Related Work

Tethered aerostat systems have received limited attention in the literature and most of the focus has been directed at large aerostats with long tethers (> 1000 m). DeLaurier in 1972 was first to study the dynamics of an aerostat attached to a comprehensive cable model [5]. This work considered only steady state wind conditions, but turbulence was later addressed by DeLaurier in 1977 [6]. The stability of the system was analyzed by showing that the motion decoupled into separate lateral and longitudinal motions. Lateral instabilities at low wind speeds were predicted (though later conversations with the author indicate these may have been due to spurious results). In 1973, Redd *et al* used experimental data to validate their linear model of a tethered aerostat in a steady wind [30]. A trend study of the stability of the aerostat indicated that certain physical parameters can have an important effect on the stability. Also in 1973, Leclaire and Rice of the US Air Force conducted the only study found on a multi-tethered aerostat system [21]. Through experimental results with a natural shaped aerostat, it was found that a payload with a tri-tethered system is subject to much lower displacements than with a single tethered aerostat. It was also found that separating the payload and the aerostat by a leash decreased the displacement further.

Progress with the dynamics modeling of aerostat was made by Jones and Krausman in 1982 when a 3-D nonlinear dynamics model with a lumped mass discretized tether was established [17]. Jones and Delaurier built on this basic model by using semi-

empirical data for estimating the aerodynamic properties of the aerostat [16]. Also, a panel method was introduced for modeling the aerostat. This entailed dividing the aerostat into vertical slices to account for the effects of turbulence variations along the length of the hull. Badesha and Jones in 1993 used this model to perform a stability analysis of a large commercial aerostat [1]. The stability analysis was conducted by linearizing the equations of motion of the nonlinear model. The results show the aerostat to be stable over a range of wind conditions. The dynamics model developed by Badesha and Jones was validated by Jones and Shroeder in 2001 with experimental data obtained from US Army flight tests [18]. This work demonstrated that it is possible to assess the fidelity of a dynamics model using real flight data, including recorded winds. Another 3-D tethered aerostat model was developed by Humphreys in 1997 [13]. This model uses a single partial differential equation to relate the motion and forces along the tether. Experimental validation of the dynamics model was achieved by performing tests with a scaled model in a tow tank.

In 1998, Etkin used a simplified linear approach to studying the stability of a towed body [8]. The generalized formulation of this approach provides relevance to a range of bodies constrained by a cable including that of a buoyant tethered aerostat. It was found that the instabilities did occur, but could be eliminated by proper positioning of the cable attachment point. In 1999, Nahon presented a 3-D nonlinear method for modeling a multi-tethered aerostat system using a lumped mass tether model [25]. This method was based on earlier modeling work with autonomous underwater vehicles [24], submerged cables [7] and towed underwater vehicle systems [2]. The reliability of the

towed vehicle dynamics model was established by Lambert *et al* through a comparison with experimental sea trials data [20].

1.3 Research Focus

The focus of the present work is the analysis and development of the scaled model of the multi-tethered aerostat system. This effort is split between investigation of the system's dynamics and providing the conceptual design for the experimental system.

The dynamics model developed by Nahon for a spherical aerostat formed the basis for the dynamics research presented here. A brief introduction to the dynamics model will be provided in Chapter 2. This will be followed by details of the several modifications that were made to the dynamics model to improve its capabilities. As a first step, the model was scaled using a systematic approach. Next, modifications were made to both the tether model and the spherical aerostat model to obtain more realistic conditions. Experimental data was used to improve the tether model's representation of internal damping and vortex shedding oscillations were added to the spherical aerostat model. Finally, a second more complicated aerostat with a streamlined shape was incorporated into the model.

In Chapter 3, a detailed examination of the performance of the streamlined aerostat was accomplished by utilizing the dynamics model to conduct a linear stability analysis. The linearized model is used to study the effects on stability of changing various system parameters.

Chapter 4 presents the conceptual design for the scaled aerostat system. The goal for the design of the experimental system is to provide high level decisions that will

advance the initial design concepts for the full system from the proof of concept stage to the point where the final detailed design can take place. The design for the experimental aerostat system occurred simultaneously with the dynamics model development. Like the dynamic analysis, the starting point of the experimental system design was the scaling results from the original LAR conceptual design. The primary components that were selected during the design process are the aerostat, the tethers and the winching system. The aerostat was chosen after a comparison of the expected performance of several distinct aerostat types. The selection of the tether material was made based on the strength and stiffness characteristics of available tethers. The design of the tether winching system relied heavily on simulation results from the dynamics model. Through exploitation of the simulation results, the dynamics model became a valuable design tool for designing the winch system since its requirements are directly related to dynamic behavior of the system.

Chapter 5 provides the conclusions of this research as well as recommendations for future work.

Chapter 2

Dynamics Model

The first step in modeling the dynamics of the scaled aerostat system was to choose the physical parameters of the system, using scaling laws, so as to maintain dynamic similarity. Once the basic physical characteristics of the scaled system were established, several additions were made to the existing dynamics model in order to improve its representation of the real system. These additions include:

- an accurate model of tether damping found through experimental trials,
- vortex shedding effects for the spherical aerostat,
- a model of a more complex aerostat with a streamlined shape.

This chapter will present the theory, procedure and results for scaling and dynamics modeling of the tethered aerostat system. The details of the original dynamics model developed previously by Nahon [25] will be outlined first.

2.1 Original Dynamics Model

The dynamics model is obtained by discretizing the tethers into a series of nodes and then simultaneously solving for the force and motion at each node using appropriate kinematic and dynamic relationships. A 2-D schematic of the original model for the tethered aerostat system is shown in Figure 2.1. The model consists of the following elements: a spherical aerostat, a leash joining the aerostat to the receiver, the receiver which is enclosed in a spherical shell, three discretized tethers and three idealized winches used to adjust the length of the tether. The aerostat was modeled as a spherical point mass at the upper node of the leash, subject to buoyancy, aerodynamic drag and gravity. The added mass of the aerostat was also included. The payload was modeled as a spherical point mass subject to gravity and aerodynamic drag.

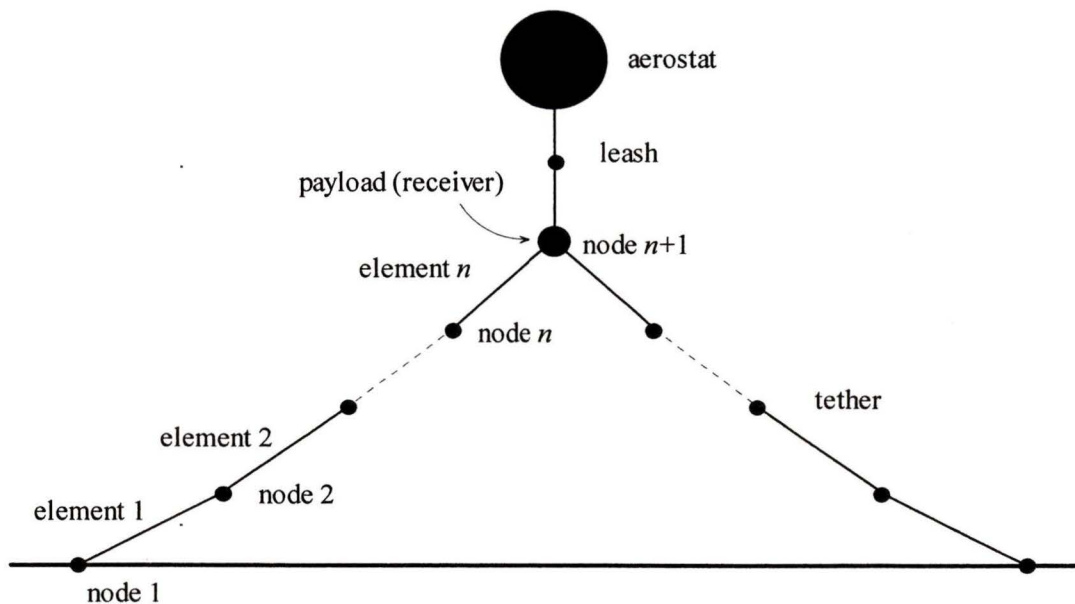


Figure 2.1: Discrete implementation of tethered aerostat dynamics model.

The leash and the tethers were modeled as a series of discrete tether elements connected by frictionless revolute joints as presented by Driscoll and Nahon [7]. The mass of each element was lumped into its respective end nodes. The forces in the tether model were separated into internal and external forces. The internal forces, generated within the tether, were due to axial stiffness and internal damping. Figure 2.2 shows the model for the internal tether forces. The external forces on the tether, imposed by the environment, consist of aerodynamic drag and gravity.

A wind model was incorporated to determine the aerodynamic influence on the system. The aerodynamic force on each tether element, the aerostat and receiver depended on the wind speed and direction at that particular location. The wind model consisted of a height dependent mean wind profile with superimposed turbulent gusts that were also height dependent. The mean wind speed profile was calculated using a power law profile representing the earth's boundary layer [25]. The turbulent gusts were generated using desired gust statistical properties, including turbulence intensity, scale length and spectra [25].

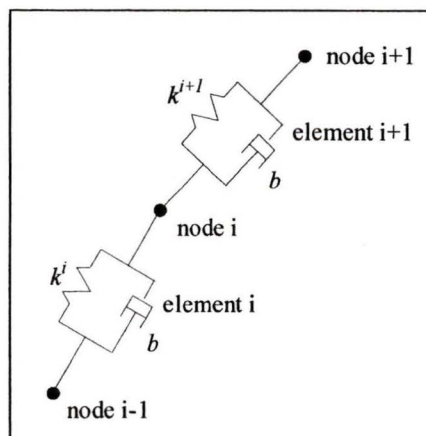


Figure 2.2: Schematic of visco-elastic internal forces for the tether model.

Ideal winches were included in the dynamics model by actively adjusting the tether length based on the position of the payload. A basic PID feedback control loop was implemented to achieve this. The controller output was based on the position error of the payload. The distance between each winch and the actual position of the payload, \mathbf{p} , was compared to the corresponding distance between the winch and the desired position, \mathbf{p}_d to generate an error signal, e_j for the PID controller:

$$e_j = \|\mathbf{p}_d - \mathbf{p}_{w_j}\| - \|\mathbf{p} - \mathbf{p}_{w_j}\|$$

A 2-D representation of the geometry is shown in Figure 2.3. The location of the j -th winch is represented as \mathbf{p}_{w_j} . The winch controller uses this error to compute the length change for each tether, ΔL_j using the following PID control law:

$$\Delta L_j = -k_d(\dot{e}_j) - k_p(e_j) - k_i \int e_j dt$$

where k_d , k_p and k_i are the derivative, proportional and integral control gains. The concept behind this approach is that if all three tether lengths correspond to be the desired tether lengths, then it is assured that the payload is in the desired location. The gains for the controller were found using trial and error.

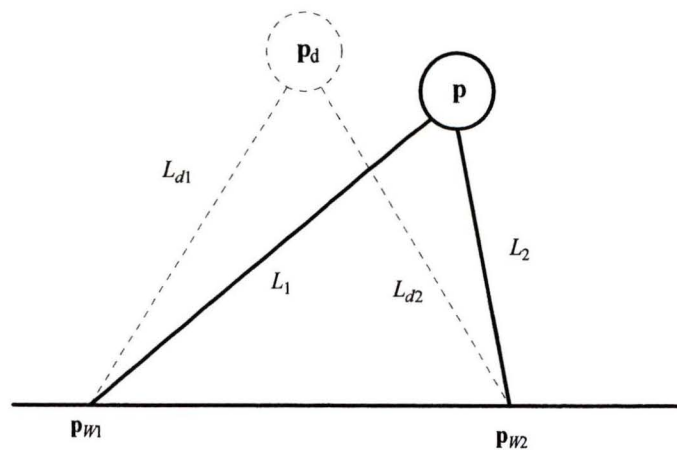


Figure 2.3: Control terminology.

2.2 Scaling of Full Scale LAR System

The technique of using a scale model (referred to as simply ‘model’) to predict the performance of a large dynamic system (referred to as ‘prototype’) is a common engineering practice. By constructing a model of the aerostat system and observing its behavior, valuable understanding of the performance of the prototype can be acquired without expending the time, cost and effort of actually building the full scale device. The physical parameters for the full scale prototype system were based on a static analysis of the system by Fitzsimmons *et al* [9] and are summarized in Table 2.1.

Table 2.1: Physical parameters of prototype tethered aerostat system.

tethers / leash	diameter	18.5 mm
	density	840 kg/m ³
	elastic modulus	16.8 GPa
	damping coefficient	10000 kg/s
aerostat	diameter	19.7 m
	mass	609.6 kg
	buoyancy	40876 N
receiver package	diameter	6 m
	mass	500 kg
overall system	focal length	500 m
	winch circle radius	1200 m

2.2.1 Dynamic Similarity

To ensure that the measured results of the model faithfully represent the behavior of the prototype, dynamic similarity must exist between the two. When dynamic similarity is attained, all the physical parameters of model and prototype pertaining to the dynamic behavior differ only by a scaling factor. Each parameter will have a unique scaling factor that depends on the combination of fundamental units or dimensions that comprise that parameter. Most physical parameters are characterized by the common dimensions of length ' L ', mass ' M ', time, ' T ' and sometimes temperature ' Θ ', raised to various powers. When dynamic similarity is satisfied, there is a single, constant scaling factor between the model and the prototype for each dimension. The scaling factor for a particular physical parameter is made up of a combination of the scaling factors of the dimensions that describe it. To illustrate this concept, consider the following equation for a characteristic force on the model, F_m in terms of a similar force on the prototype, F_p :

$$F_m = \lambda_F F_p, \quad \lambda_F = \frac{\lambda_M \lambda_L}{\lambda_T^2}$$

where the scaling factor for force, λ_F is a function of the scaling factors for mass λ_M , length, λ_L and time λ_T , since the units of force are mass·length/time².

2.2.2 Dimensional analysis

The goal of the scaling process is to determine the appropriate value of the scaling factor for every parameter that is relevant to the dynamics of the system. There are two basic steps of this process; the first is to choose the relevant parameters and the second is to perform a dimensional analysis on the chosen parameters.

2.2.2.1 Relevant Parameters

The success of the scaling exercise is dependent on choosing the appropriate scaling parameters. Since we are interested in the dynamic behavior of the system, any physical parameter that appreciably influences the dynamics must be selected. It should be mentioned that parameters for various components that are characterized by the same combination of fundamental units are only included once. For instance, the length parameter for the various mechanical components is represented only once and is termed the characteristic length, l . The list of 13 relevant parameters is given in Table 2.2.

Table 2.2: Relevant parameters for tethered aerostat system.

category	parameter	symbol	dimension
mechanical components	length	l	L
	mass	m	M
	moment of inertia	I	ML^2
	force	F	MLT^{-2}
	density	ρ	ML^{-3}
	tether elastic modulus	E	$ML^{-1}T^{-2}$
	tether damping coefficient	b	MT^{-1}
environment	velocity	U	MT^{-1}
	density	ρ_e	ML^{-3}
	viscosity	μ	$ML^{-1}T^{-1}$
	acceleration due to gravity	g	LT^{-2}
response	time	t	T
	frequency	f	T^{-1}

2.2.2.2 Buckingham Pi Theorem

The scaling factors for each relevant parameter can be found by arranging the parameters into dimensionless quantities. Since the dimensionless quantities or groups must be equal for the scale and prototype, the individual scaling parameters can be obtained. The Buckingham Pi theorem [19] states that if a physical problem includes n relevant parameters in which there are m dimensions, then these quantities can be arranged into $n - m$ independent dimensionless parameters. A formal representation of this theorem is presented next. Consider a function that is dependent on n quantities, $A_1, A_2, A_3, \dots, A_n$ such that:

$$\phi(A_1, A_2, A_3, \dots, A_n) = 0$$

These quantities can be arranged into $n - m$ independent dimensionless parameters, $\Pi_1, \Pi_2, \Pi_3, \dots, \Pi_{n-m}$ such that:

$$f(\Pi_1, \Pi_2, \Pi_3, \dots, \Pi_{n-m}) = 0$$

For the aerostat system, the number of relevant parameters is $n = 13$ while the number of dimensions is $m = 3$. Therefore, 10 dimensionless Π terms are required to describe the system. The procedure for arranging the relevant parameters from Table 2.2 into dimensionless Π terms is included in Appendix A. The resulting dimensionless Π terms are:

$$\Pi_1 = \frac{m}{\rho_e l^3}, \quad \Pi_2 = \frac{I}{\rho_e l^5}, \quad \Pi_3 = \frac{F}{\rho_e U^2 l^2}, \quad \Pi_4 = \frac{\rho}{\rho_e}, \quad \Pi_5 = \frac{E}{\rho_e U^2}$$

$$\Pi_6 = \frac{b}{\rho_e U l^2}, \quad \Pi_7 = \frac{\rho_e U l}{\mu}, \quad \Pi_8 = \frac{U^2}{gl}, \quad \Pi_9 = \frac{tU}{l}, \quad \Pi_{10} = \frac{fl}{U}$$

These particular dimensionless terms are only one set of numerous possible combinations that could be arranged for our system of variables. A closer inspection of these terms reveals some familiar dimensionless parameters: Π_7 is Reynolds' number, Re ; Π_8 is the Froude number, Fr ; and Π_{10} is Stouhal's number, St [34]. To ensure dynamic similarity between the model and the prototype, all Π terms must be equal for the two systems. Thus, the appropriate scaling factors for each variable can be determined using these equalities. Certain scaling factors are predetermined as the environmental testing conditions are established. Since the model and the prototype will both be operated in the same outdoor environment, the scaling factor for the environmental parameters are set to one. Hence the atmospheric density and viscosity and the acceleration due to gravity all have a scaling factor of one ($\lambda_{\rho_e} = \lambda_{\mu} = \lambda_g = 1$). The one-third length scale, $\lambda_l = 1/3$ is also predetermined. The base scaling factor, λ is equal to $\lambda_l = 1/3$.

A consequence of our inability to scale the environmental conditions is that strict equality of all the dimensionless terms cannot be satisfied. A conflict arises when considering the Π_7 and Π_8 terms. For consistent scaling of Re , the scaling factor for the velocity, $\lambda_U = 3$, but for consistent scaling of Fr , $\lambda_U = \sqrt{1/3}$. Since, in light of this conflict, it is not possible for us to build a model that will have strict dynamic similarity to the prototype, we must decide *which* dimensionless number should be matched so as to provide closer similarity.

This task is not straightforward since both dimensionless terms appear to have relevance to the aerostat system. The Re can be interpreted as a ratio of inertia forces to viscous forces while the Fr can be interpreted as the ratio of inertia forces to gravity forces. Therefore, understanding which dimensionless term is more significant can be

reduced to understanding which force has a greater influence on the aerostat system, viscous forces or gravity forces. For steady fluid flow applications Re similarity is more important as gravity effects are minimal compared to their viscous counterparts. Conversely, for fluid flow applications near stream boundaries, Fr similarity is more important as gravity effects dominate over viscous forces. For the tethered aerostat system, both the gravity forces and the viscous forces are expected to influence the dynamics. To investigate this matter further, it was decided to proceed with proper scaling of both Re and Fr separately in order to perform a quantitative comparison of the similarity of the two scaled systems.

2.2.3 Reynolds' Number Scaling

For proper scaling of Re , the corresponding scale factors for each parameter were calculated using $\lambda_{\rho_e} = \lambda_{\mu} = \lambda_g = 1$ and $\lambda_l = \lambda = 1/3$ and recognizing that the scaling factor of each Π term is 1. This process is demonstrated with the following equations:

$$\begin{aligned} \Pi_7 = 1 = \frac{\lambda_{\rho_e} \lambda_U \lambda_l}{\lambda_{\mu}} &\Rightarrow \lambda_U = \lambda^{-1}, & \Pi_1 = 1 = \frac{\lambda_m}{\lambda_{\rho_e} \lambda_l^3} &\Rightarrow \lambda_m = \lambda^3, & \Pi_2 = \frac{\lambda_l}{\lambda_{\rho_e} \lambda_l^5} &\Rightarrow \lambda_l = \lambda^5, \\ \Pi_3 = 1 = \frac{\lambda_F}{\lambda_{\rho_e} \lambda_U^2 \lambda_l^2} &\Rightarrow \lambda_F = 1, & \Pi_4 = 1 = \frac{\lambda_{\rho}}{\lambda_{\rho_e}} &\Rightarrow \lambda_{\rho} = 1, & \Pi_5 = 1 = \frac{\lambda_E}{\lambda_{\rho_e} \lambda_U^2} &\Rightarrow \lambda_E = \lambda^{-2}, \\ \Pi_6 = 1 = \frac{\lambda_b}{\lambda_{\rho_e} \lambda_U \lambda_l^2} &\Rightarrow \lambda_b = \lambda, & \Pi_9 = 1 = \frac{\lambda_l \lambda_U}{\lambda_l} &\Rightarrow \lambda_l = \lambda^2, & \Pi_{10} = 1 = \frac{\lambda_f \lambda_l}{\lambda_U} &\Rightarrow \lambda_f = \lambda^{-2}, \end{aligned}$$

The physical parameters of the scaled aerostat system can be obtained by applying the above scaling factors to the appropriate parameters of the prototype from Table 2.1. The results are given in Table 2.3. It should be noted that the model parameters presented are not physically realizable. This stems from the one-to-one scaling of the force which

dictates that the buoyancy of the aerostat for the model equal the buoyancy of the prototype's aerostat while undergoing a reduction in size by 1/3 (this corresponds to reduction in volume by $(1/3)^3$ or 1/27). Therefore the internal gas for the aerostat must provide the same lift as helium but with 27 times less volume. This is not possible since it would require a gas with a negative density. Although the model is not physically possible, the dynamics model was modified according to these parameters and simulation results were obtained. The results are presented and compared with results for proper Froude number scaling to ascertain which scaling strategy provides better similarity to the prototype.

Table 2.3: Physical parameters for scaled model with consistent *Re* scaling.

component	parameter	scaling factor	value
tethers / leash	diameter	$\lambda_l = 1/3$	6.17 mm
	density	$\lambda_\rho = 1$	840 kg/m ³
	elastic modulus	$\lambda_E = (1/3)^{-2}$	151.2 GPa
	damping coefficient	$\lambda_b = 1/3$	3333 kg/s
aerostat	diameter	$\lambda_l = 1/3$	6.57 m
	mass	$\lambda_m = (1/3)^3$	22.6 kg
	buoyancy	$\lambda_F = 1$	40876 N
receiver package	diameter	$\lambda_l = 1/3$	2 m
	mass	$\lambda_m = (1/3)^3$	18.5 kg
overall system	focal length	$\lambda_l = 1/3$	166.7 m
	winch circle radius	$\lambda_l = 1/3$	400 m
response	time	$\lambda_t = (1/3)^2$	0.111 $t_{prototype}$

2.2.4 Froude Number Scaling

The scaling factors for each parameter are calculated while maintaining Fr similarity as follows:

$$\Pi_8 = 1 = \frac{\lambda_U^2}{\lambda_g \lambda_l} \Rightarrow \lambda_U = \sqrt{\lambda}, \quad \Pi_1 = 1 = \frac{\lambda_m}{\lambda_{\rho_e} \lambda_l^3} \Rightarrow \lambda_m = \lambda^3, \quad \Pi_2 = \frac{\lambda_l}{\lambda_{\rho_e} \lambda_l^5} \Rightarrow \lambda_l = \lambda^5,$$

$$\Pi_3 = 1 = \frac{\lambda_F}{\lambda_{\rho_e} \lambda_U^2 \lambda_l^2} \Rightarrow \lambda_F = \lambda^3, \quad \Pi_4 = 1 = \frac{\lambda_{\rho}}{\lambda_{\rho_e}} \Rightarrow \lambda_{\rho} = 1, \quad \Pi_5 = 1 = \frac{\lambda_E}{\lambda_{\rho_e} \lambda_U^2} \Rightarrow \lambda_E = \lambda,$$

$$\Pi_6 = 1 = \frac{\lambda_b}{\lambda_{\rho_e} \lambda_U \lambda_l^2} \Rightarrow \lambda_b = \lambda^{\frac{5}{2}}, \quad \Pi_9 = 1 = \frac{\lambda_l \lambda_U}{\lambda_l} \Rightarrow \lambda_l = \sqrt{\lambda}, \quad \Pi_{10} = 1 = \frac{\lambda_f \lambda_l}{\lambda_U} \Rightarrow \lambda_f = \frac{1}{\sqrt{\lambda}},$$

Table 2.4: Physical parameters for scaled model with consistent Fr scaling.

component	parameter	scaling factor	value
tethers / leash	diameter	$\lambda_l = 1/3$	6.17 mm
	density	$\lambda_{\rho} = 1$	840 kg/m ³
	elastic modulus	$\lambda_E = 1/3$	5.6 GPa
	damping coefficient	$\lambda_b = (1/3)^{2.5}$	641.5 kg/s
aerostat	diameter	$\lambda_l = 1/3$	6.57 m
	mass	$\lambda_m = (1/3)^3$	22.6 kg
	buoyancy	$\lambda_F = (1/3)^3$	1514 N
receiver package	diameter	$\lambda_l = 1/3$	2 m
	mass	$\lambda_m = (1/3)^3$	18.5 kg
overall system	focal length	$\lambda_l = 1/3$	166.7 m
	winch circle radius	$\lambda_l = 1/3$	400 m
response	time	$\lambda_t = \sqrt{1/3}$	0.577 $t_{prototype}$

The physical properties for this case differ significantly from the previous system with *Re* scaling. The most notable difference is the scaling of the force. For this case, the force scales with the same factor as the mass which is consistent with the actual relationship between force and mass when acceleration is not scaled ($\lambda_g = 1$). As a result, the aerostat's internal gas density is the same for the model and the prototype.

2.2.5 Simulation Results

The dynamics model was used to compare the similarity of the two scaled systems to the prototype. The physical parameters of the system were modified according to the appropriate scaling factors and the following test case was run for the prototype:

- system in the symmetrical configuration ($\theta_{ze} = \theta_{az} = 0^\circ$) initially at equilibrium,
- wind speed is ramped from $U = 0$ to 10 m/s from $t = 5$ to 6 s
- wind speed constant with altitude.

Cases were also run for the two model systems, however the input wind speed and ramp time were adjusted to reflect the scaling factors for each model. Hence, for the model with *Re* scaling, the wind speed is ramped from $U = 0$ to 30 m/s from $t = 0.556$ to 0.667 s while for the model with *Fr* scaling, the wind speed is ramped from $U = 0$ to 5.77 m/s from $t = 2.89$ to 3.46 s.

For the similarity comparison with the prototype, the simulation output parameters from the model must be multiplied by the appropriate reciprocal scaling factor. For instance the results for tether tension in the model with *Fr* scaling must be multiplied by the reciprocal of the force scaling factor $[(1/3)^3]^{-1} = 27$. The simulation results are displayed in Figure 2.4 for the case with *Re* scaling and in Figure 2.5 for the

case with Fr scaling. The simulation output parameters presented for the comparison are the position error of the receiver package and the tension in each tether. The position error of the receiver is characterized by error in and out of the focal plane. The focal plane is defined as the planar surface that is perpendicular to the focal line which connects the center of the reflector to the receiver.

There are clear differences between the two sets of results. In Figure 2.4 the model and prototype do not show good agreement whereas in Figure 2.5 the model results closely mimic those of the prototype. The interpretation of these results is clear. The role of the Froude number on the system is much more significant than the role of Reynolds' number. This also implies that gravity forces play a greater role in the system's dynamics than viscous forces. The small discrepancy between the results for the model and prototype in Figure 2.5 indicate that complete dynamic similarity has not been achieved. This is expected since Reynolds number similarity was not maintained. The drag coefficient for the spherical aerostat depends primarily on Re and thus the relationship between the drag coefficient and Re for the model will not be consistent with the equivalent relationship for the prototype. The effects of this inconsistency are relatively small and overall the agreement between the model and prototype for the case with proper Fr scaling is good. The results suggest that a scaled model of the aerostat system is capable of accurately predicting the behavior of the full scale prototype. There is some uncertainty whether the exact physical parameters for the system components outlined in Table 2.4 are attainable with off the shelf components, but this issue will be addressed with the design of the experimental system in Chapter 4.

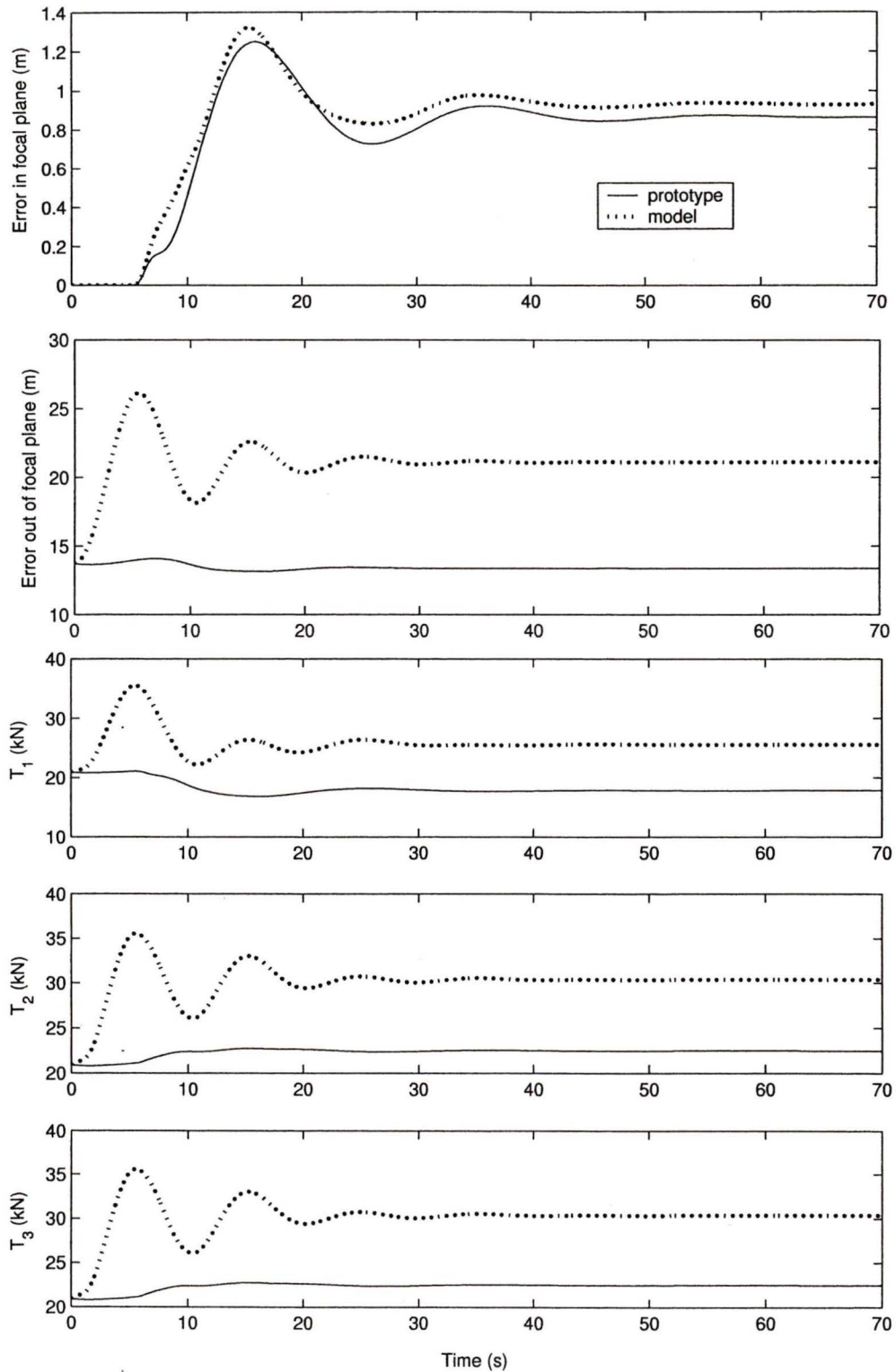


Figure 2.4: Simulation results; error of receiver in and out of the focal plane and tether tension, for scaled model and prototype, using *Re* scaling.

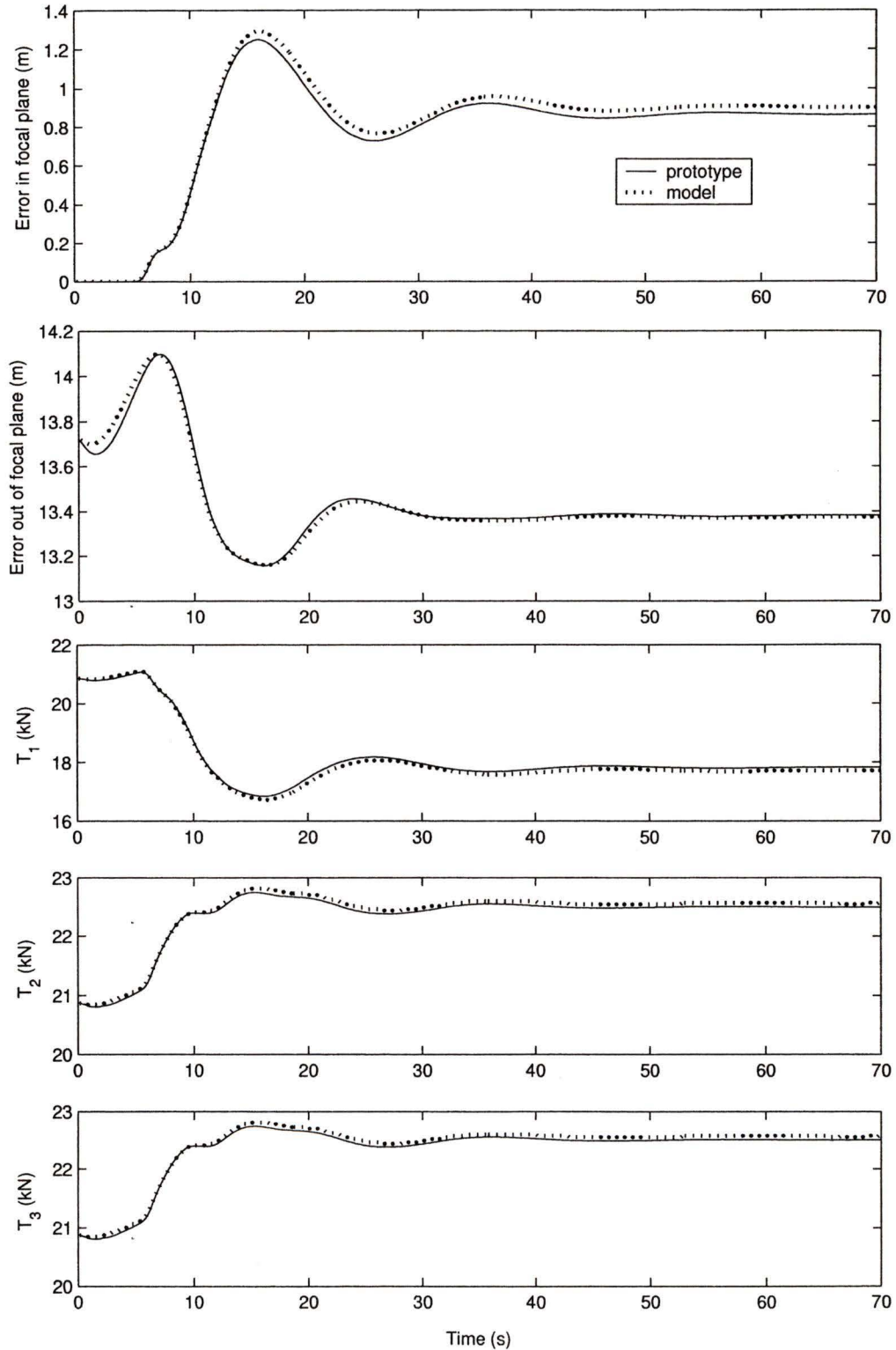


Figure 2.5: Simulation results; error of receiver in and out of the focal plane and tether tension, for scaled model and prototype, using Fr scaling.

2.3 Tether Damping

The dynamic behavior of the tethered aerostat system is heavily influenced by the tether properties. Therefore, it is important to accurately define all of the tether parameters that are used in the dynamics model. The tether model considers both damping and elastic properties of the tether. The elastic modulus, E is usually known for commercially available tethers, however the damping coefficient, b is seldom provided. The value $b = 10000$ kg/s originally used for the tether in the prototype was chosen arbitrarily. Since the effect of tether damping is likely to have a significant impact on the system behavior, an updated estimate of the damping characteristics was necessary. In order to estimate the damping coefficient of a particular tether material an experimental investigation was undertaken based on the procedure outlined by Hamilton in [11]. The elastic modulus of the tether can also be determined from the experimental results as a means of confirming the provided data from the manufacturer. The theory of the damping model and the experimental procedure and results are presented in subsequent sections.

2.3.1 Theory

Internal tether tension has two components; one due to the tether's elasticity and one due to the tether's damping properties. The damping effect is due to the internal friction between the several individual strands that are woven together to comprise the tether. It is common to model the internal friction damping effects of a tether using a viscous damping model. The viscous damping model is illustrated in this equation:

$$T_D = b\dot{L}$$

where T_D is the damping force, b is the damping coefficient and \dot{L} is the rate of change of the tether length.

A typical response for spring tension during free vibration of a simple spring-mass-damper system is shown in Figure 2.6. The maximum amplitude of the response is T_0 and the damped period is τ_d . The tension $T(t)$ can be expressed as:

$$T(t) = (T_0 - T_s)e^{-\zeta\omega_n t} \cos(\omega_d t) + T_s \quad (2.1)$$

where ω_n is the natural frequency, ω_d is the damped frequency and ζ is the damping ratio.

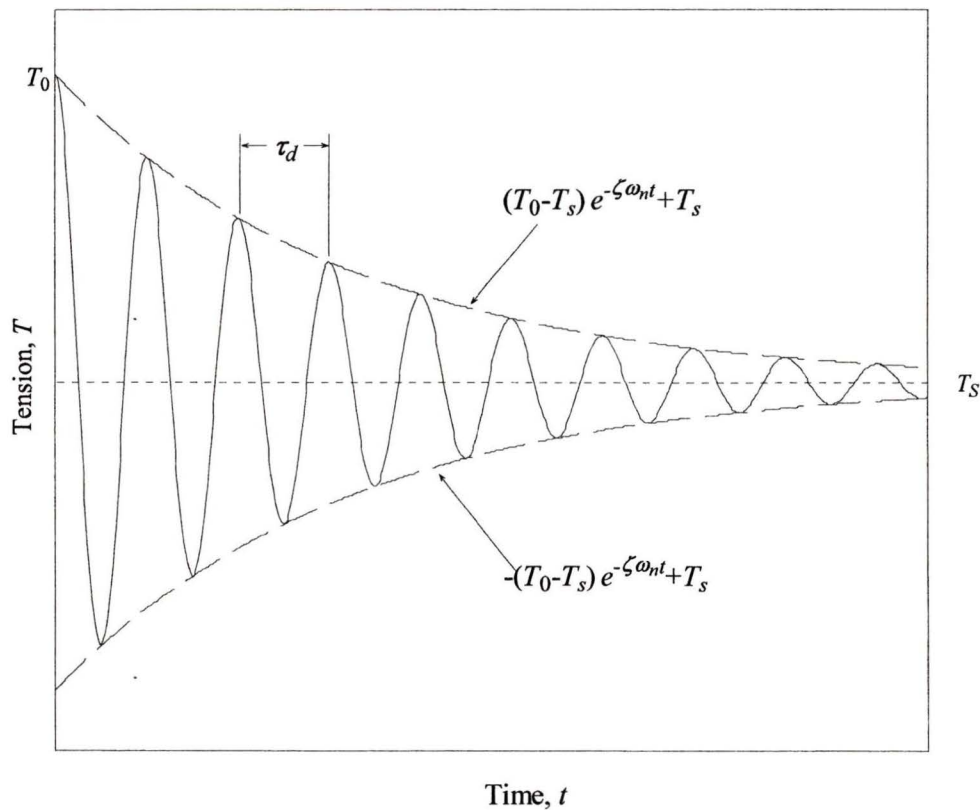


Figure 2.6 Typical response with viscous damping.

Assuming that a tether segment behaves as a viscoelastic spring, the natural frequency would be related to the tether properties according to the equations:

$$\omega_n = \sqrt{\frac{k}{m}} \quad \text{where } k = \frac{EA}{L} \quad \text{and} \quad m = \frac{T_s}{g} \quad (2.2)$$

where k is the stiffness of the tether, E is the elastic modulus, A is the cross sectional area of the tether, m is the mass of the load and T_s is the static loading of the tether. The mass of the tether is neglected in this formulation since it is not expected to contribute appreciably to the overall response. The damping characteristics of the tether are related using the following equations:

$$\omega_d = \frac{2\pi}{\tau_d} \quad \text{where} \quad \omega_d = \omega_n \sqrt{1 - \zeta^2} \quad \text{and} \quad \zeta = \frac{b}{2m\omega_n} \quad (2.3)$$

By experimental measurement of the response of the tether tension due to an initial disturbance, the damping coefficient the tether, b and the elastic modulus, E can be obtained using the relationships outlined above with the following method:

- estimate the damped frequency using the period of oscillation,
- use the logarithmic decrement of the oscillation peaks to estimate the damping ratio, ζ and natural frequency, ω_n
- calculate damping coefficient, b and elastic modulus, E , using eqs. (2.2) and (2.3)

2.3.2 Experimental Procedure

Our approach was to perform a simple test in which a tether with an initial static load is disturbed and the time response of the tether tension is recorded with a load cell. Photographs of the experimental apparatus are shown in Figure 2.7. The tether system was supported from a vertical bolt through an I-beam along the ceiling of a loading bay.

The top of the tether was attached to an S-type load cell which was mounted directly to the I-beam bolt. The lower end of the tether was attached to the load. A garbage pail filled with concrete was used for the load and a vertical bolt was set into the concrete surface to facilitate the attachment to the tether. Attachment brackets were built for each end of the tether with the purpose of securing the tether to the vertical bolts. The bracket consisted of a U-bolt clamp which fixed the tether in place and the outer frame which rigidly attached the clamp to the bolts. It was thought that this arrangement would limit the introduction of flexibility to the system. The tether tested was a high density polyethylene rope with 12 individual strands braided together and has a trade name of *Plasma*. The sample was provided by Puget Sound Rope for testing purposes.

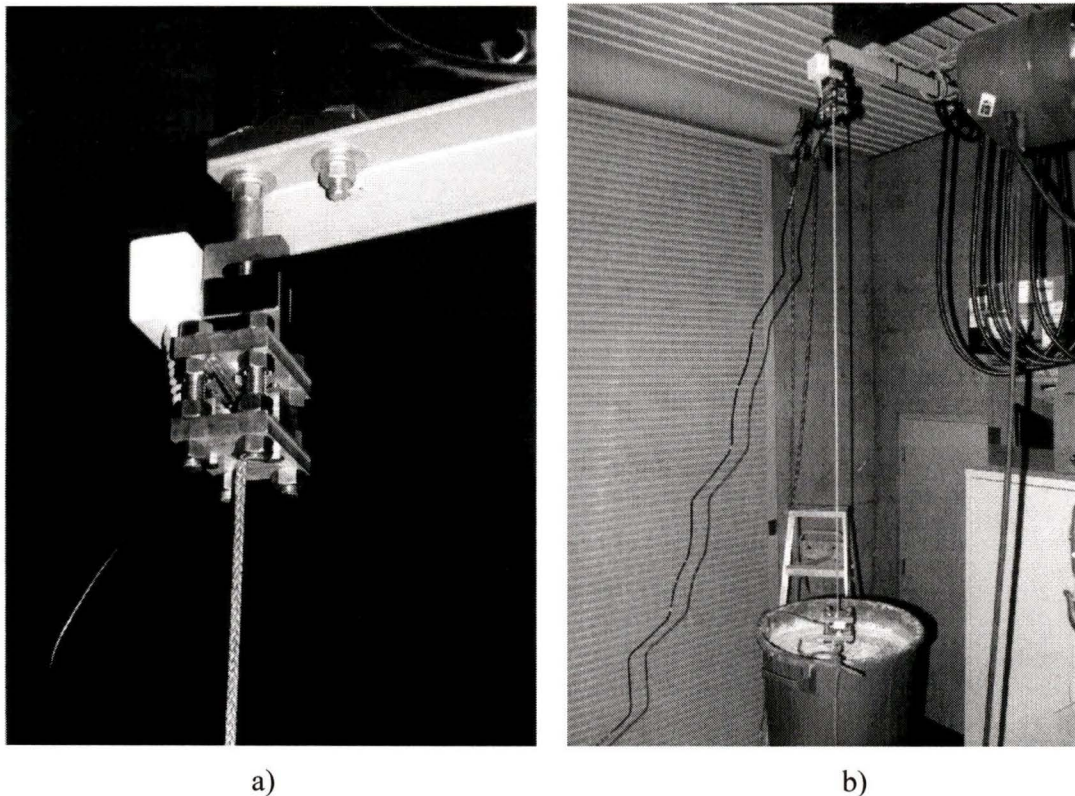


Figure 2.7: Experimental apparatus; a) rope attachment assembly with S-type load cell, b) full system with concrete weight attached to tether.

The diameter of the tether was 5 mm which is close to the 6.17 mm tether size specified for the model by the scaling process. The mass of the load was 123 kg which is within the range of tension expected during operation of the aerostat system. To investigate the response under a different load, trials were performed with an additional 44 kg of added weight. Also, tests were performed at three different lengths to determine how the damping characteristics change with tether length. The disturbance to the system was achieved by striking the bottom surface of the concrete block with a hammer.

2.3.3 Results

Several trials were performed for each load and tether length. An example of the experimental results for a typical trial is presented in Figure 2.8. To determine if the measured response is characterized by viscous damping, the logarithmic decrement of the oscillatory peaks was studied. It can be seen in Figure 2.6 that the curve through the oscillatory peaks is described by $(T_0 - T_s)e^{-\zeta\omega_n t}$. Therefore the log of the peak values should be linear with a slope of $-\zeta\omega_n$ since $\ln[(T_0 - T_s)e^{-\zeta\omega_n t}] = \ln(T_0 - T_s) - \zeta\omega_n t$. Figure 2.9 presents a plot of the log of the peak values for a single test case. The linear fit to the data was obtained using Matlab's linear data fitting function. A definite linear trend to the results is observed suggesting that the viscous model is adequate for representation of tether damping. For an ideal viscous damping response, only the first two peaks are required to determine the damping ratio. For our analysis of the experimental results, the first seven peaks are considered in order to average the data. The peaks beyond the first seven are not included in the analysis since noise effects infiltrate the results as the oscillation decays.

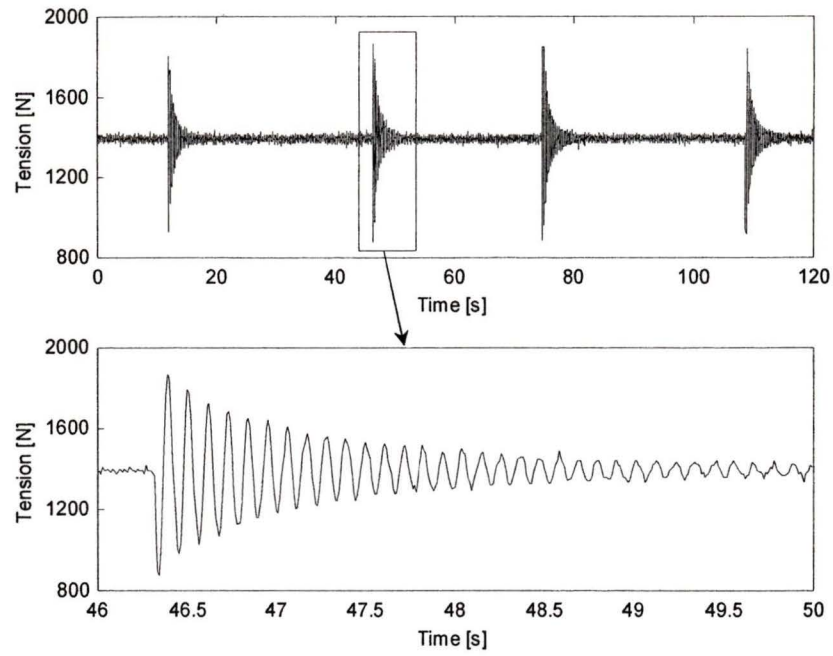


Figure 2.8: Sample of experimental results for tether test.

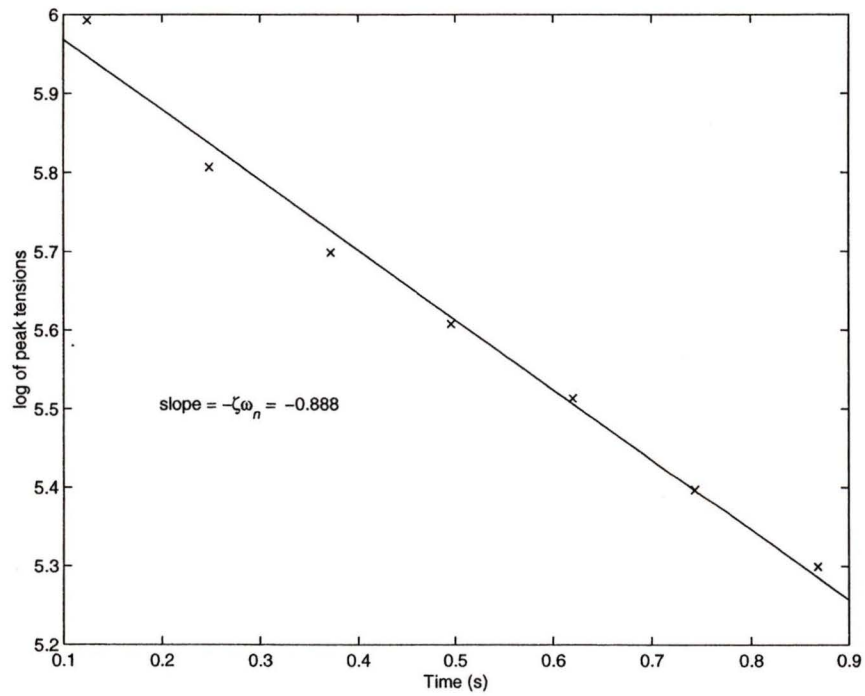


Figure 2.9: Log of the peak tensions for case with $L = 1.775$ m and $m = 186$ kg.

From the slope of the linear fit and the observed damped frequency of $\omega_d = 47.29$ rad/s, the equations of (2.3) were used to calculate the damping ratio, $\zeta = 0.0188$ and natural frequency $\omega_n = 47.30$ rad/s. It is observed that for this case $\omega_n \approx \omega_d$ as they differ by only 0.02%. This outcome is a result of the small magnitude of the damping ratio.

The results for the tether damping and elastic properties are presented in Table 2.5. Since several trials were performed for each combination of load and tether length, the reported results are the average of the repeated trials. The results for the damping coefficient, b are not consistent over the six testing configurations. This implies that the tether's damping capability is dependent on both the tether's length and load. The results for the damping ratio however are more consistent. Thus, to properly incorporate the damping characteristics observed with this tether in the dynamics model, a constant damping ratio should be used, instead of the constant damping coefficient used previously. The damping coefficient can then be calculated from the damping ratio based on the tether load and length.

Table 2.5: The average experimental results for the damping and elastic parameters.

L (m)	1.461		1.775		2.146	
m (kg)	142	186	142	186	142	186
ω_d (rad/s)	56.80	51.17	53.59	47.48	49.50	43.69
ζ	0.021	0.020	0.016	0.017	0.016	0.017
b (kg/s)	354.0	375.3	254.0	306.0	227.5	275.4
k (kN/m)	459.9	487.2	408.9	419.3	348.7	355.3
E (GPa)	34.8	36.4	37.1	37.9	38.4	38.9

The length of the discretized tether elements used in the dynamics model are typically 15 to 30 m long. Unfortunately, this is considerably longer than the tether segments tested as our testing apparatus could not accommodate tethers longer than 2.2 m. The damping ratio is relatively constant throughout the range of tethers tested, but it is not certain whether this trend would be repeated for tethers up to an order of magnitude longer. Nevertheless, the average of the results obtained for ζ was applied to the tether elements in the dynamics model presuming that the damping ratio does not change significantly with tether length.

The elastic properties of the tether are also given in Table 2.5. The values for E vary slightly for the different test configurations. This suggests that the stress vs. strain relationship is not precisely linear throughout the testing range. To evaluate the results for E , a comparison is made with data from the tether manufacturer. A version of the stress vs. strain relationship for the *Plasma* tether is shown in Figure 2.10.

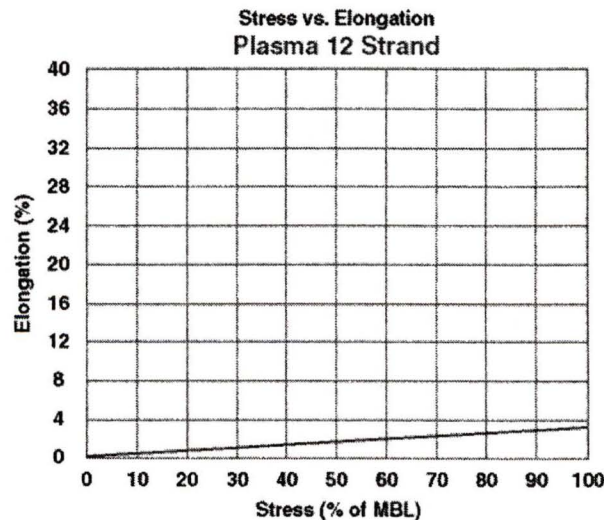


Figure 2.10: Elongation vs. stress for Plasma 12 Strand from Puget Sound Rope [29].

This plot presents a linear stress vs. strain curve where the stress is given in terms of the percentage of the minimum breaking load (MBL). The MBL for the 5 mm tether is 1246.5 MPa. The elastic modulus for the tether is the slope of the stress vs. strain curve which is calculated as $E = 1246.5 \text{ MPa}/0.033 = 37.8 \text{ GPa}$. This corresponds closely to the experimental values obtained for E . However, it should be noted that due to the limited resolution of the curve in Figure 2.10 the accuracy of the estimation of the elastic modulus is not entirely reliable. For the purpose of the dynamics model, a constant value of E will be used calculated as the average (37.4 GPa) of the results from Table 2.5. The original value of E used for the scaling exercise was less than half of this because the original system was designed with a different tether material, *Spectra Plasma* is a recent and improved version of *Spectra* with greater stiffness and strength.

2.4 Vortex Shedding of a Spherical Aerostat

The dynamic behavior of an aerostat in a wind field is important when ascertaining the suitability of the aerostat for a particular task. For most aerostat applications it is desired for the aerostat flight to be stable and steady in any wind condition. By developing an understanding of the dynamic behavior of various aerostats, it is possible to evaluate and compare which type is the most suited for the requirements of the LAR system. The three types of aerostats considered for this application are; 1) streamlined, 2) spherical and 3) variable lift. A spherical aerostat is inherently simple and hence was chosen for the initial dynamics model of the tethered aerostat system. However, the basic dynamics model did not include vortex shedding oscillations that are known to occur with tethered spheres in steady fluid flow. An effort was made to improve the dynamics model by estimating the

vortex shedding behavior of a spherical aerostat based on previous experimental investigations in 1997 by Govardham and Williamson [10].

From the results of their study, the vortex shedding characteristics of our particular aerostat were characterized. This was achieved by determining the frequency and amplitude of the expected transverse oscillations from the experimental data provided. Once the expected oscillatory behavior was established, the next step was to account for this motion in our dynamic simulation. A convenient method to accomplish this was to simply add a transverse, sinusoidal force to the equations of motion of the aerostat. The appropriate magnitude and frequency of the added force was determined by trial and error utilizing the simulation results for a single tethered aerostat. A detailed illustration of this process is described next.

The experimental results of Govardham and Williamson were obtained by measuring the movement of a tethered sphere in a free-surface water channel. The physical characteristics of the sphere were varied in order to get results for a range of mass and length ratios. The mass ratio, M^* is defined as the ratio of the sphere mass to the displaced fluid mass and the length ratio, L^* is defined as the ratio of tether length to sphere diameter. The physical parameters for our base case scaled tethered aerostat are shown in Table 2.6 and Figure 2.11. The aerostat on a single tether represents a subsystem of the multi-tethered aerostat system from the payload to the aerostat, with the single tether representing the aerostat's leash.

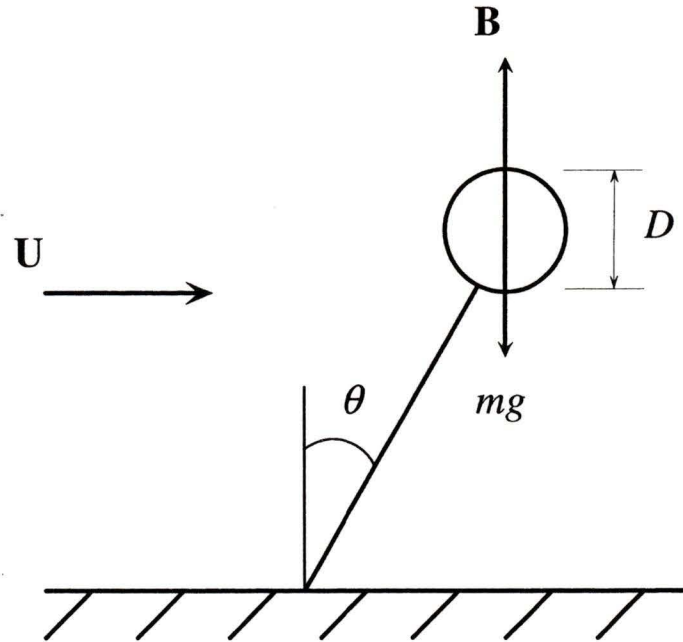


Figure 2.11: Tethered aerostat.

Table 2.6: Parameters for tethered aerostat.

aerostat mass, m	22.6 kg
aerostat diameter, D	6.57 m
buoyancy, B	1514 N
tether length, L	33.3 m

2.4.1 Amplitude of Oscillation

Results for the amplitude of the transverse oscillation are presented Figure 2.12 for $M^* = 0.26$ and 0.76 and $L^* = 8.93$ and 3.93 [10]. The amplitude is expressed as an rms value and is normalized by dividing it by the sphere diameter, D . For our system, $M^* = 0.15$

which is less than the two mass ratios presented, indicating our aerostat is more buoyant. It is observed in Figure 2.12 that the amplitude of oscillation is lower for the smaller M^* value of 0.26. Therefore, to obtain a relationship for $M^* = 0.15$ the results for $M^* = 0.26$ were applied directly giving a conservative estimate of the oscillation amplitude.

An interesting result of the work of Govardham and Williamson is that if the amplitude is plotted against a dimensionless velocity, V_R termed ‘reduced velocity’, it becomes independent of L^* . Thus the results given in Figure 2.12 are valid for any L^* . The reduced velocity is calculated as follows:

$$V_R = \frac{U}{f_n D} \quad (2.4)$$

where f_n is the natural frequency which for a buoyant pendulum is calculated using:

$$f_n = \frac{1}{2\pi} \sqrt{\frac{B - mg}{mL}} \quad (2.5)$$

To apply the results to our system, values for V_R were calculated for a range of wind speeds and the rms value of the oscillation amplitude divided by the aerostat diameter was obtained from the curve for $M^* = 0.26$. The maximum oscillation amplitude, y_{max} is preferred over the rms value, y_{rms} for the purpose of introducing the oscillation to the aerostat of the dynamics model. Since the rms value of a sine wave is 0.707 times its peak value, y_{max} was easily determined for each case.

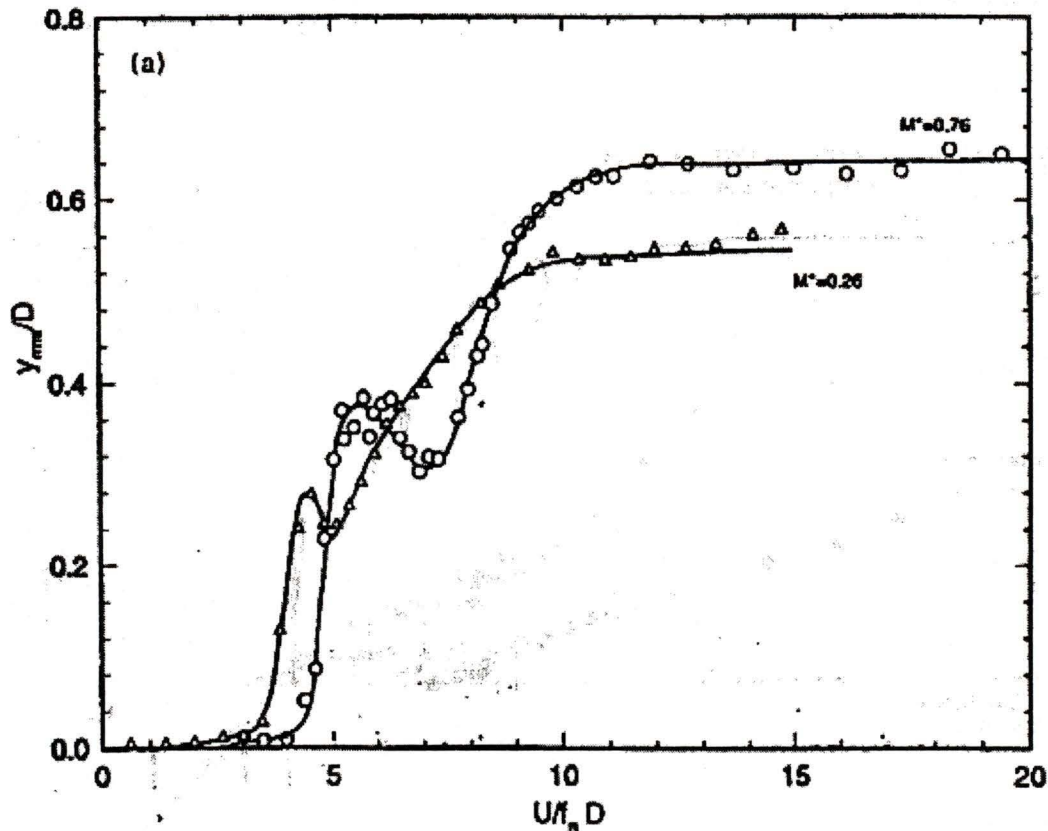


Figure 2.12: Normalized root-mean-square (y_{rms}/D) of transverse oscillations versus reduced velocity (V_R) for two mass ratios $M^* = 0.26(\Delta)$ and $M^* = 0.76(O)$ from [10].

2.4.2 Frequency of Oscillation

The frequency of the transverse oscillation must be determined in order to completely characterize its motion. The frequency of the oscillations measured by Govardham and Williamson is shown in Figure 2.13. Results were only available for $M^* = 0.76$ so these results will be applied to our system. It is interesting to note that at $V_R = 5$, the frequency of the oscillation is equal to the natural frequency of the buoyant pendulum. This corresponds to the local peak of the amplitude curve for $M^* = 0.76$ in Figure 2.12. This suggests that the peak is caused by resonance between the natural frequency of the pendulum and the wake vortex shedding frequency. This is confirmed by the fact that the

Strouhal number, defined as $\frac{fD}{U} = 0.2$ specifies the vortex shedding frequency f ,

coincides with the inverse of V_R [34].

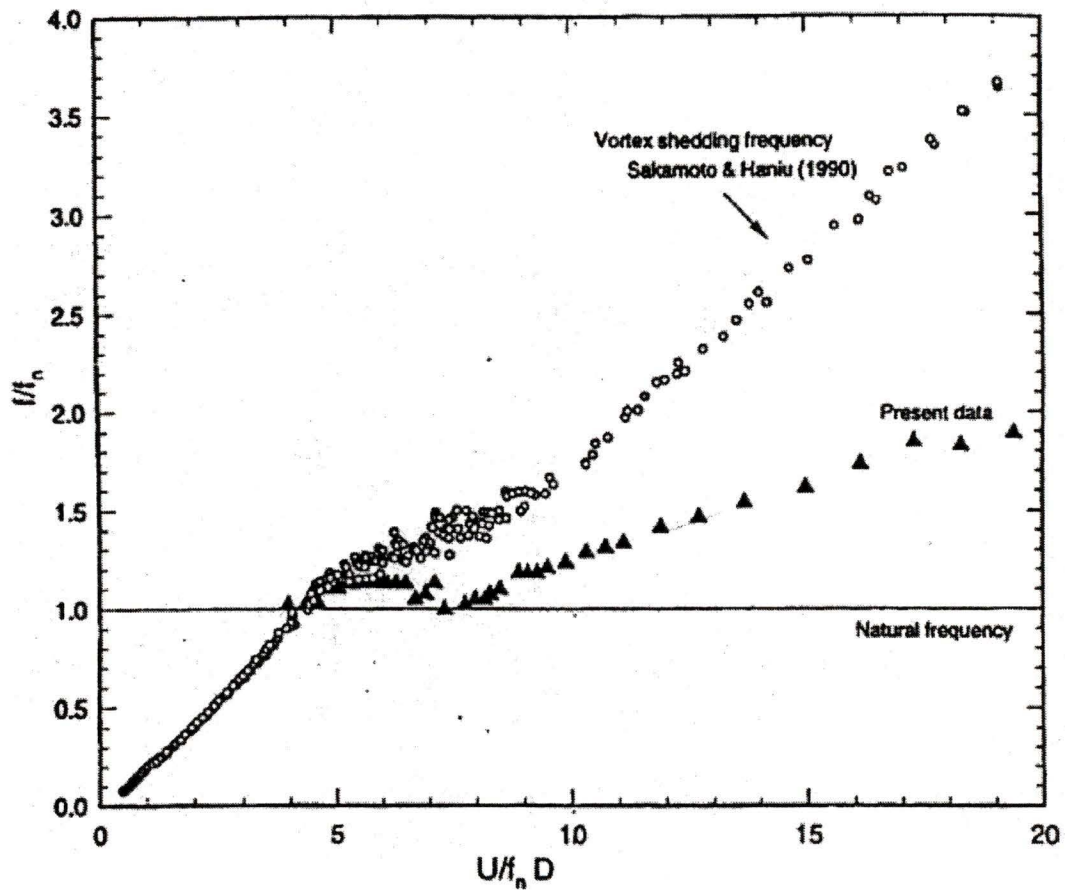


Figure 2.13: Transverse oscillation frequency (f/f_n) versus reduced velocity (V_R) for $M^* = 0.76$. Also plotted for comparison, is the vortex shedding frequency of a sphere from Sakamoto and Haniu (1990) [10].

2.4.3 Applying the Oscillation to Dynamics Model

The transverse oscillation of the tethered aerostat due to vortex shedding was incorporated into the dynamics model of the spherical aerostat, thus providing a means of predicting realistic behavior for the tethered aerostat system. The oscillations were incorporated by applying an external sinusoidal force at the aerostat's center of mass. The force, \mathbf{F} is expressed in the inertial frame as:

$$\mathbf{F} = \begin{bmatrix} F_0 \sin \omega t \sin \theta_w \\ F_0 \sin \omega t \cos \theta_w \\ 0 \end{bmatrix}$$

where F_0 is the amplitude of the force and ω is the oscillation frequency and θ_w is the wind angle. The terms $\sin \theta_w$ and $\cos \theta_w$ ensure that the force acts perpendicular to the incoming wind direction.

For a particular wind speed, the oscillation characteristics (y_{max}/D and f/f_n) were obtained from Figure 2.12 and Figure 2.13. The values for F_0 were determined by trial and error with the simulation results for the tethered aerostat. With the maximum amplitude and frequency of the oscillation known, the sinusoidal force was varied until the appropriate transverse motion was observed. A summary of the results of this process for a variety of wind speeds is displayed in Table 2.7. The amplitude of the force, F_0 is plotted in Figure 2.14. For implementation with the simulation code, given an input wind speed, the values for F_0 and ω are taken directly from Table 2.7. For non-integer wind speeds, linear interpolation is used. It should be mentioned that these results are only applicable to the specified aerostat and leash properties. If a change is made to any of the system variables, the entire process must be repeated. However, for a system that is

entirely scaled according to the scaling factors presented in section 2.2.4 the results obtained can be used if multiplied by the appropriate scaling factor.

Table 2.7: Vortex shedding oscillation characteristics and trial and error force inputs.

U (m/s)	V_R	Y_{rms}/D	Y_{rms} (m)	Y_{max} (m)	f/f_n	f (Hz)	ω (rad/s)	F_0 (N)
1	0.719	0	0	0.000	-	-	-	-
2	1.44	0	0	0.000	-	-	-	-
3	2.16	0	0	0.000	-	-	-	-
4	2.88	0	0	0.000	-	-	-	-
5	3.59	0.05	0.3335	0.472	1.0	0.209	1.313	70
6	4.31	0.28	1.8676	2.641	1.0	0.209	1.313	415
7	5.03	0.24	1.6008	2.264	1.0	0.209	1.313	350
8	5.75	0.28	1.8676	2.641	1.1	0.23	1.445	530
9	6.47	0.32	2.1344	3.018	1.2	0.251	1.577	750
10	7.19	0.36	2.4012	3.396	1.2	0.251	1.577	845
11	7.91	0.4	2.668	3.773	1.2	0.251	1.577	950
12	8.63	0.44	2.9348	4.150	1.2	0.251	1.577	1040
13	9.34	0.48	3.2016	4.528	1.2	0.251	1.577	1150
14	10.06	0.52	3.4684	4.905	1.3	0.272	1.709	1480
15	10.78	0.53	3.5351	4.999	1.3	0.272	1.709	1525
16	11.5	0.54	3.6018	5.094	1.3	0.272	1.709	1550
17	12.22	0.55	3.6685	5.188	1.3	0.272	1.709	1575
18	12.94	0.56	3.7352	5.282	1.4	0.293	1.841	1885
19	13.66	0.56	3.7352	5.282	1.4	0.293	1.841	1885
20	14.38	0.56	3.7352	5.282	1.5	0.313	1.967	2180

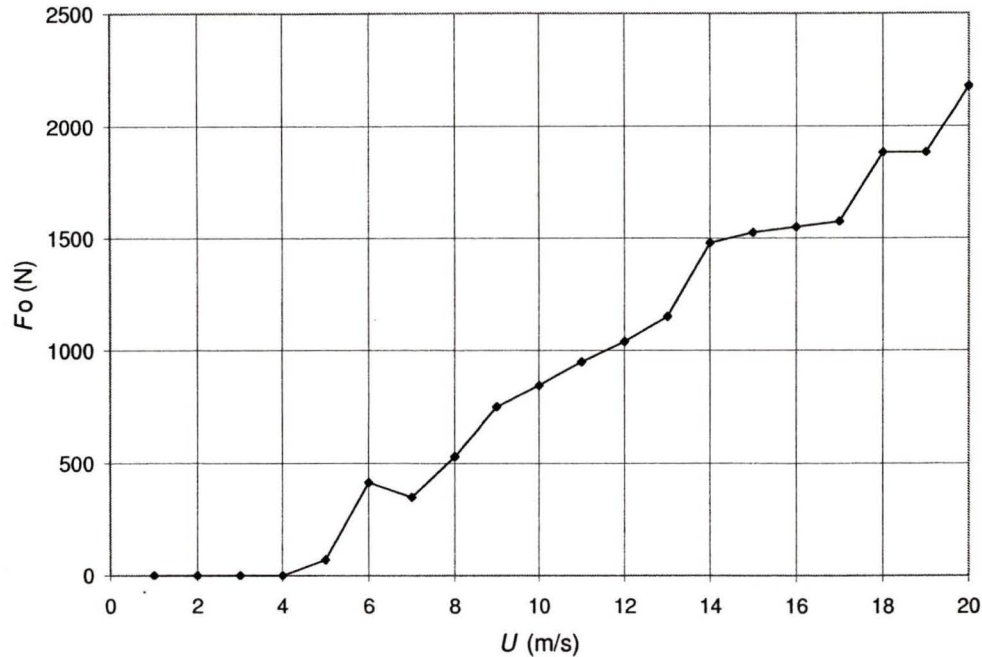


Figure 2.14: Sinusoidal force amplitude related to wind speed.

2.4.4 Results for Single-tether System

Simulation results are presented in Figure 2.15 to show the characteristics of the aerostat motion for a general condition with the wind speed $U = 6$ m/s. The system was initially in an equilibrium position for a no wind case and the wind was stepped up to 6 m/s during the first time step. From these results, it is observed that the induced transverse oscillation in the y-direction of 2.64 m has little effect on the position of the aerostat in the x or z-direction which change by less than 10 cm. It is interesting to compare the transverse force applied to the aerostat with the increase in tether tension. For this case, the transverse force amplitude was 415 N, but the resulting amplitude of the tether tension is only about 40 N. This implies that most of the applied force is dissipated by the atmosphere resistance on the aerostat as it oscillates from side to side.

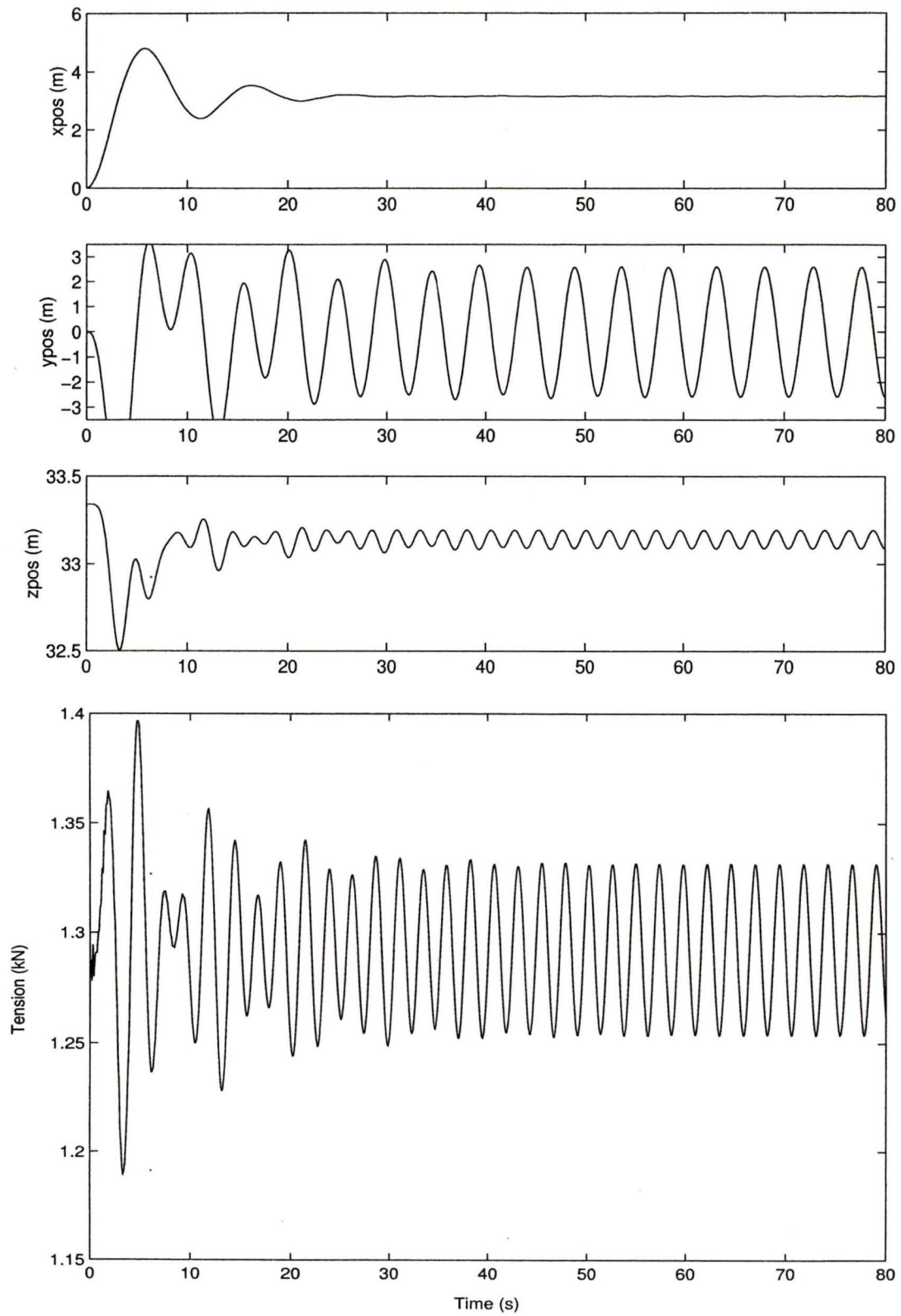


Figure 2.15: Aerostat position and tether tension for single tethered system with vortex shedding oscillations with $U = 6$ m/s.

2.4.5 Results for Multi-tethered System

To understand the effects of vortex shedding on the performance of the tri-tethered aerostat system, the same forcing function determined for the single tether system was applied to the aerostat of the tri-tethered system. It was found that the aerostat motion for this case was only slightly different from the single tether case. The slight difference can be attributed to the introduction of flexibility at the base attachment point of the leash. The position error of the payload is the variable of interest when assessing the performance of the multi-tethered system. Figure 2.16 presents results for this error along with the tension in the three tethers for a case with $\theta_{ze} = \theta_{az} = 0^\circ$ and U is increased from 0 to 6 m/s in the first time step. It is shown that the peak position error in the focal plane, once the system reaches its steady state, is about 8 cm while out of the focal plane it is less than 2 cm. This small error compared to the oscillation amplitude of the aerostat, $y_{max} = 2.46$ m, demonstrates the rigidity of the tether structure.

It is interesting to observe the fluctuations of the tensions for this case. The variation in tension of tether one has an amplitude of about 40 N while the variations in tension of tethers two and three have an amplitude of about 100 N. It was established in the preceding section that the tension in the leash has an amplitude of about 40 N. It might appear somewhat unexpected to see such high tension in the three tethers considering that there are three times as many tethers to divide the load. This result is due to the shallow geometry of the tethers. Since the leash force is primarily vertical (even with the vortex shedding oscillation, the leash is at an angle of only about 6° from the vertical) and the three tethers have an angle of only 23° from the horizontal, the force from the leash is amplified as it is transferred from the leash to the tethers.

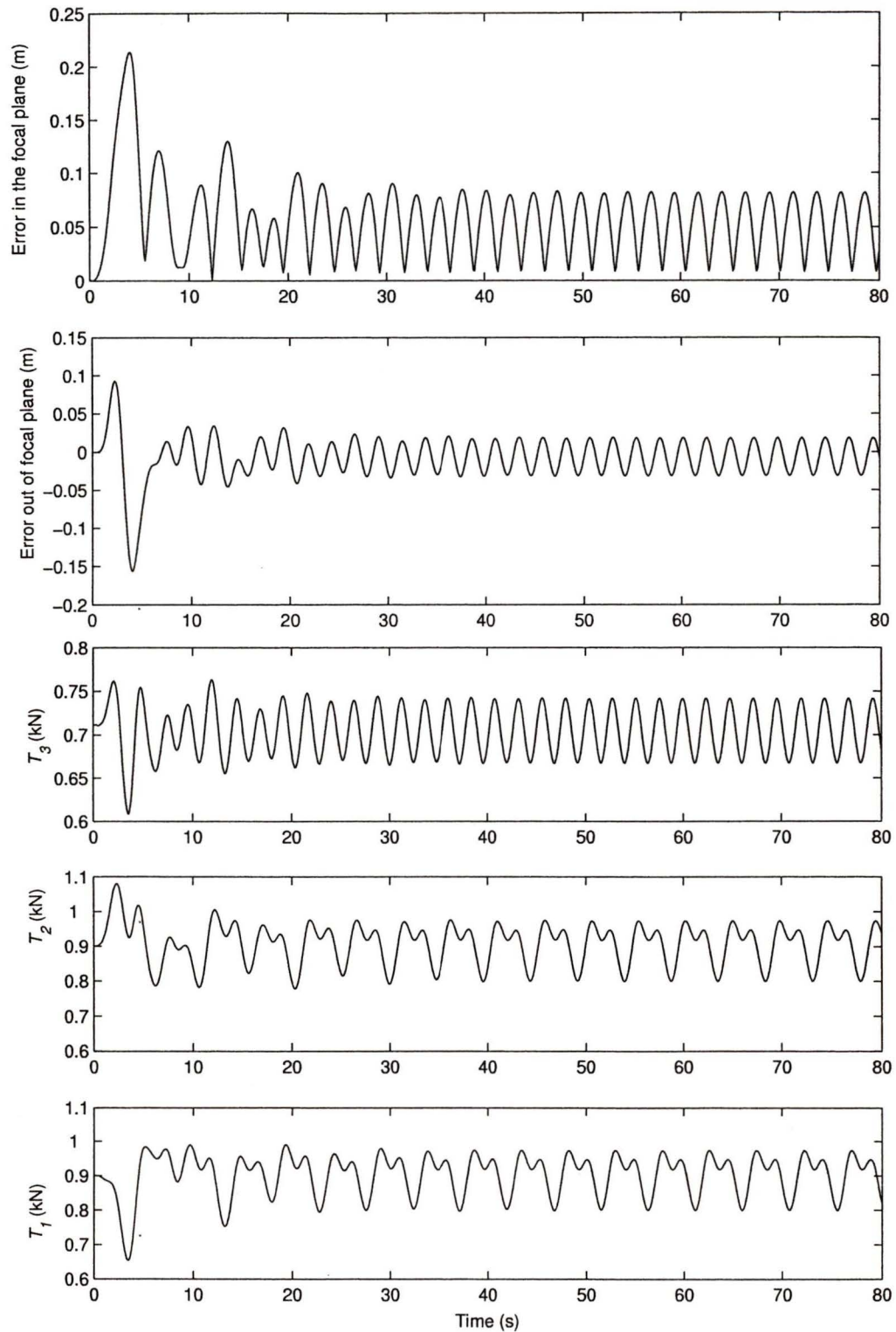


Figure 2.16: Error of the payload and tether tension for tri-tethered system with vortex shedding effects, $U = 6$ m/s.

2.4.5.1 Turbulence Effects

To quantify the vortex shedding effects on the tri-tethered system in realistic wind conditions, turbulence was added to the simulation. The results were compared to those for the same system without vortex effects as shown in Figure 2.17. The error in the focal plane, which is the critical performance indicator, changes somewhat with the addition of the vortex shedding effects. The rms error increased from 3.1 cm to 7.2 cm and fluctuations at the vortex shedding frequency are observed to dominate the motion of the payload in the focal plane. Although the displacement of the payload increased by more than a factor of two, the rigidity of the tether structure is apparent since the displacement of the payload is much less than the aerostat displacement which had an amplitude of 2.64 m. The error out of the focal plane experiences only slight changes from the vortex shedding effects. This seems logical since the perturbations due to vortex shedding are primarily in the horizontal plane. The tether tension is shown to oscillate with approximately the same amplitude and frequency as in Figure 2.16 when no turbulence was present. It should be noted that judging the performance of a system which is subject to random excitation is difficult. Therefore, these results should be viewed as qualitative in nature.

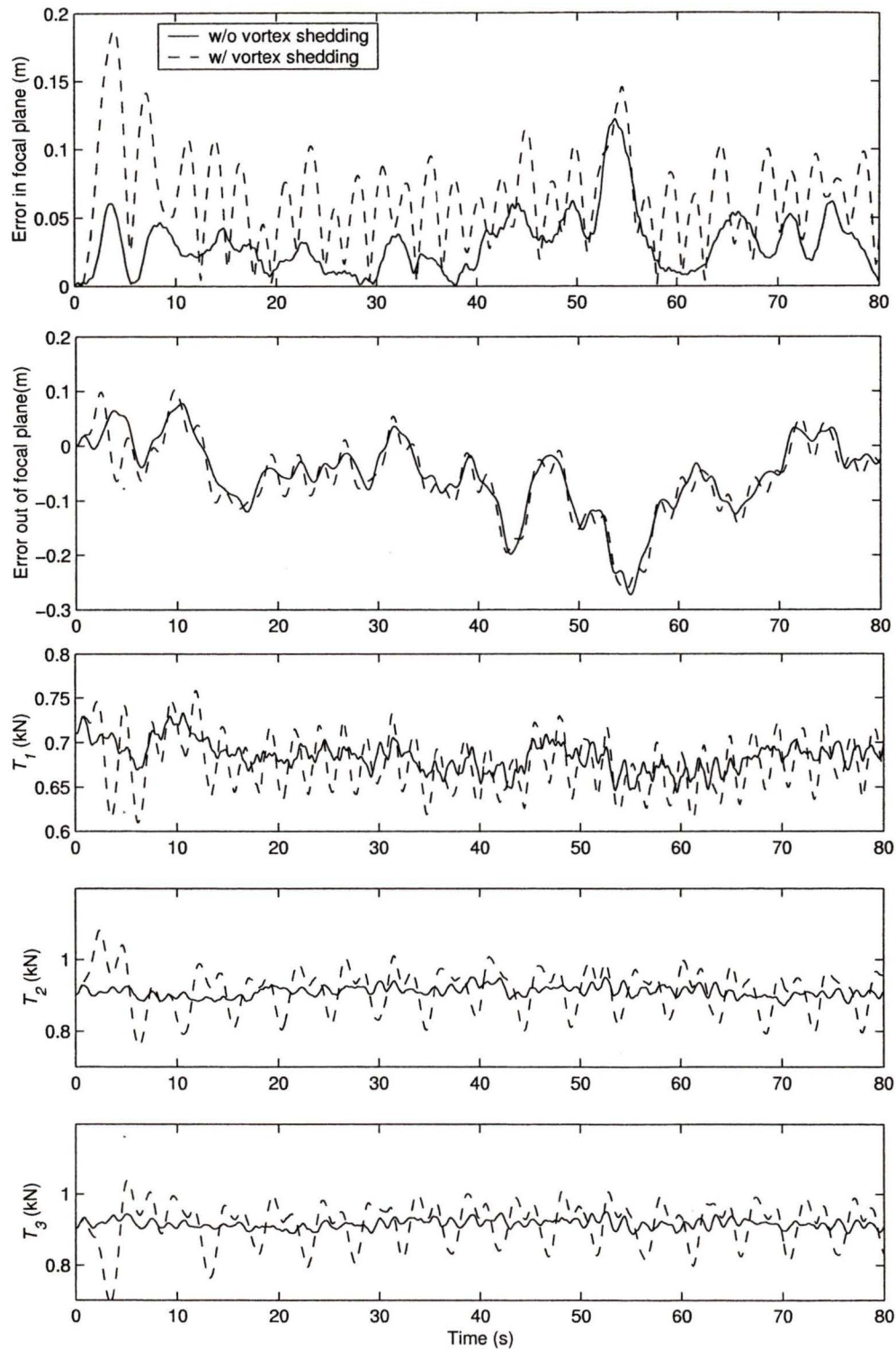


Figure 2.17: Error of the confluence point and tether tension for multi-tethered system with and without vortex shedding, with turbulence and no active control, $U = 6$ m/s.

2.4.5.2 With Active Control

The most important performance assessment of the tri-tethered system with vortex shedding is an evaluation of the extent to which the control system can overcome the oscillations. To accomplish this, the PID controller discussed in section 2.1 was applied to actively control the length of each tether depending on the position error of the payload. The error of the payload and the theoretical power supplied by the winch are presented for this comparison. Figure 2.18 shows results for the base system with and without vortex shedding. Gains of $k_p = 5$, $k_d = 1.5$ and $k_i = 1.5$ were used. The rms error the payload in the focal increased from 3.5 mm for the case without vortex shedding to 11 mm for the case with vortex shedding. Although this is an increase of more than a factor of 3, the increased error is still quite small.

A comparison of the theoretical power for each tether shows that the vortex shedding case requires almost twice as much power as the base case. The power was found by multiplying the rate of change of tether length, \dot{L} by the tether tension, T . For tethers two and three the maximum power for the case with and without vortex shedding are 75 W and 124 W respectively. Therefore, it can be concluded that accurate positioning is possible even with the aerostat experiencing vortex shedding oscillations. However, this would come at a cost of increased power and some performance degradation.

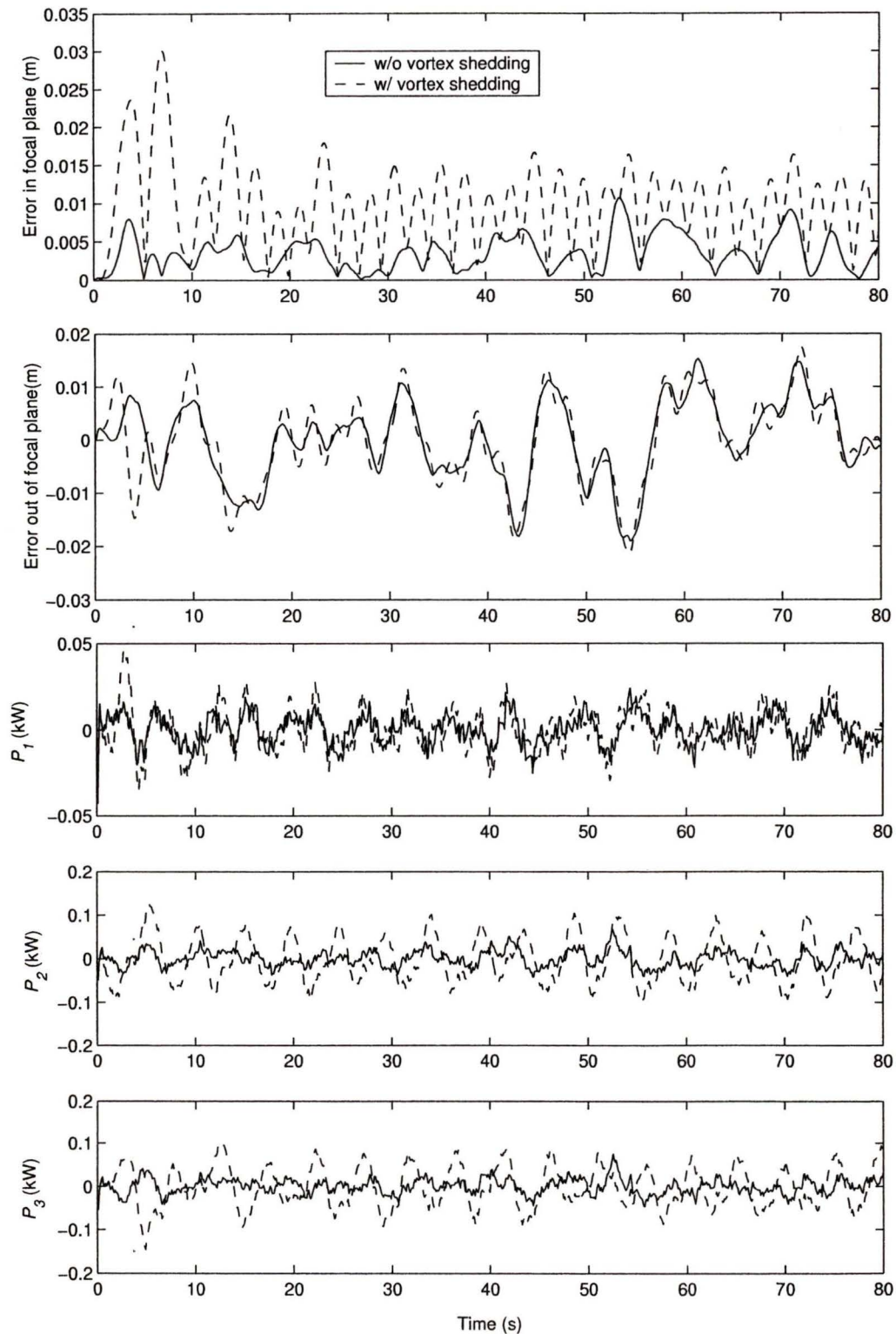


Figure 2.18: Error of the payload and winch power for multi-tethered system with and without vortex shedding, with turbulence and active control, $U = 6$ m/s.

2.4.6 Minimizing Region Where Vortex Shedding is Observed

An interesting outcome of the work of Govardham and Williamson which holds significance for our application is that the vortex shedding oscillations are eliminated for values of V_R less than 4 (see Figure 2.12). For our scaled aerostat and leash this implies that no vortex shedding oscillations are expected for wind speeds below 5 m/s. This also has important design implications because if the parameters of the system can be modified to bring the system's operating region so that $V_R < 4$ for all expected wind speeds, vortex shedding oscillations would not be a concern. This would result in a steadier system and more accurate control of the payload.

In order to reduce the system's V_R the variables in the denominator, either f_n or D , of equation 2.4 must be increased since U is the input variable. The aerostat's physical parameters such as mass, m diameter, D and buoyancy, B are pre-determined to give the system the required tension over the entire operating range. Therefore the only convenient option for reducing V_R is to increase the natural frequency of the system, f_n by decreasing the tether length, L .

As a demonstration, if we wanted negligible vortex shedding oscillations for the scaled tethered aerostat for all wind speeds up to 9 m/s the appropriate tether length can be determined using the following approach:

- set $V_R = 4$, $U = 9$ m/s and use equation 2.4 to calculate $f_n = 0.3425$ Hz,
- use equation 2.5 to calculate $L = 12.3$ m.

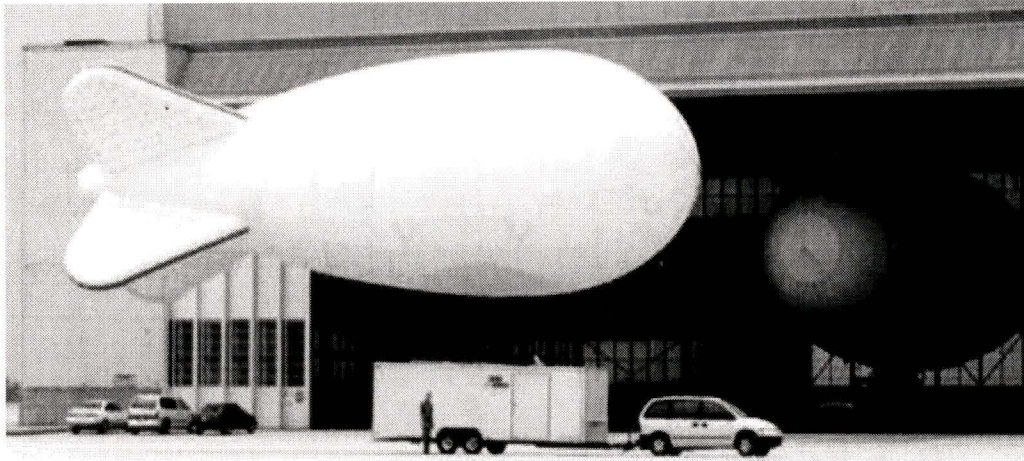
This decreases the tether length by almost a factor of 3. Therefore, if vortex shedding does prove to be problematic to the accurate control of the multi-tethered aerostat system, it may be possible to eliminate these effects by simply reducing the leash length.

However, it should be noted that the leash also plays an important role in separating the fluctuations of the aerostat from the payload itself. For this purpose a longer tether may be desired as it is more elastic. The leash length will be addressed in more detail in Chapter 4 – Experimental System Design. To relate this outcome to the full scale LAR system, a leash length of $L = 12.3 \times 3 = 36.9$ m would ensure no vortex shedding for wind speeds up to $U = 9 \times \sqrt{3} = 15.6$ m/s.

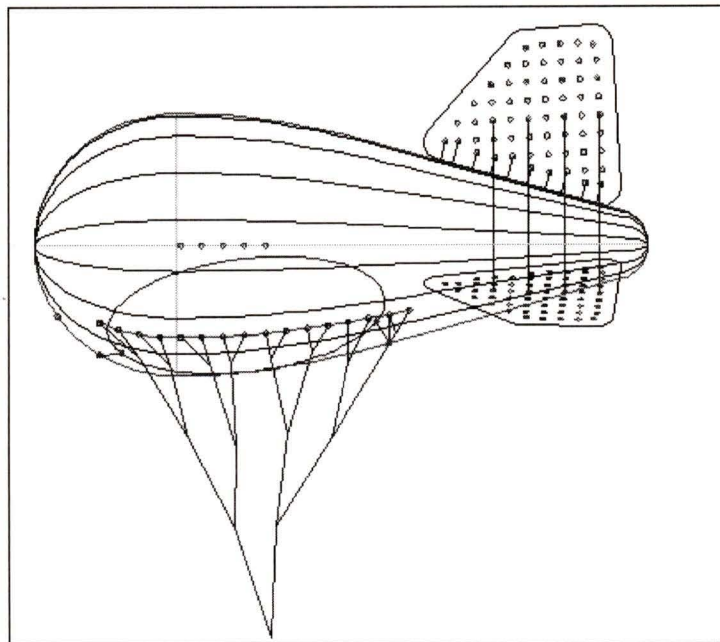
2.5 Dynamics of a Streamlined Aerostat

A model of the dynamics of a streamlined aerostat was developed to study its behavior in various wind conditions. The aerostat model is based on a proposed streamlined aerostat manufactured by Aeros Flightcam of Canoga Park, California. A photograph of a similar aerostat manufactured by Aeros along with a conceptual drawing for the proposed aerostat is shown in Figure 2.19. The central goal of this investigation is the stability of the aerostat on a single tether (leash). The results will be used to gain familiarity with the performance of the aerostat prior to investigating its behavior in the multi-tethered system. This analysis will also provide a basis for comparison of the performance of a streamlined aerostat to other possible aerostat shapes.

The parameters of interest of this study are the motion of the aerostat and the forces generated during its motion. The aerostat is considered to be rigid and is capable of full 6 degrees of freedom motion in 3D space. The output of the simulation is the translational and rotational position and velocity of the aerostat and the input is a set of initial conditions and a wind field.



a)



b)

Figure 2.19: a) Aeros Flightcam 21M aerostat, b) proposed aerostat for scaled system.

The methodology for the model development will be presented in two parts. The first is the derivation of the mathematical equations that govern the motion of the aerostat. The second part provides the process of determining the aerodynamic parameters of the aerostat.

2.5.1 Equations of Motion

The dynamic simulation of the aerostat is obtained by setting up and solving the equations of motion in 3-D space. The motion of the aerostat is described as the relative position and velocity of a body-fixed coordinate frame to an inertial coordinate frame. The body frame is attached to the aerostat's centre of gravity and the inertial frame is fixed to an arbitrary point on the ground. A diagram illustrating these reference frames in relationship to the aerostat is shown in Figure 2.20. The procedure for obtaining the motion with respect to the inertial frame involves first setting up the appropriate equations of motion for the aerostat with respect to the body frame. This creates a system of ordinary differential equations which can be solved numerically to give the position and velocity vectors in the body frame. Rotation matrices are then applied to these vectors to resolve them into the inertial frame.

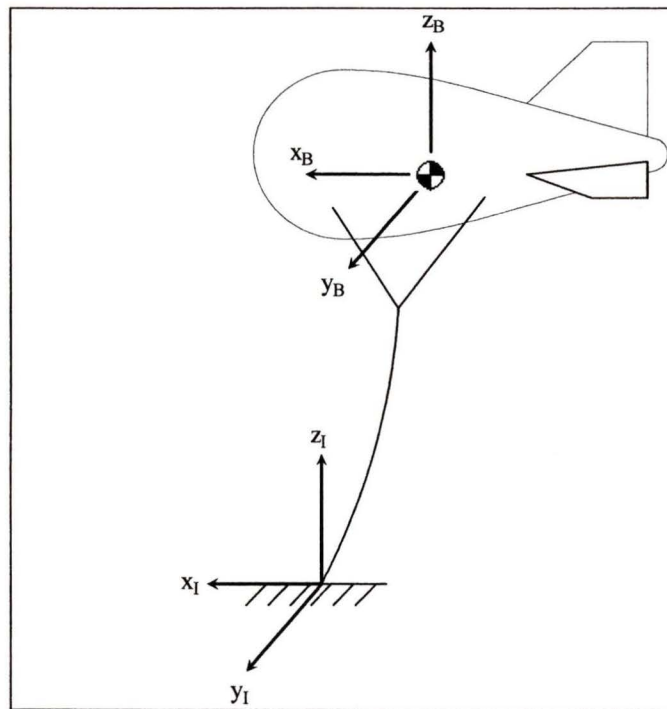


Figure 2.20: Inertial and body-fixed coordinate frames for aerostat system.

The translational motion is governed by Newton's second law and can be written as:

$$\mathbf{F}_I = m\mathbf{a}_I$$

where \mathbf{F}_I is the net force applied to the aerostat, m is its mass and \mathbf{a}_I is the acceleration of the mass centre with respect to an inertial frame. Because the aerodynamic forces are calculated as components in the body frame it becomes more convenient to solve for the motion variables also expressed in this frame. For this case, the acceleration is found by differentiating the velocity with respect to the inertial frame, $\frac{d\mathbf{V}_B}{dt}$. This is related to

$\frac{\partial\mathbf{V}_B}{\partial t}$, the rate of change of the velocity in the body frame, as follows:

$$\frac{\mathbf{F}_B}{m} = \frac{d\mathbf{V}_B}{dt} = \frac{\delta\mathbf{V}_B}{\delta t} + \boldsymbol{\omega} \times \mathbf{V}_B$$

where $\mathbf{V}_B = [u \ v \ w]^T$ and $\boldsymbol{\omega} = [p \ q \ r]^T$ is the angular velocity of the aerostat. The rotational motion of the aerostat must satisfy Euler's equation:

$$\mathbf{M}_{cm} = \mathbf{I}_{cm}\dot{\boldsymbol{\omega}} + \boldsymbol{\omega} \times \mathbf{I}_{cm}\boldsymbol{\omega} \quad \text{where} \quad \mathbf{I}_{cm} = \begin{bmatrix} I_{xx} & -I_{xy} & -I_{xz} \\ -I_{yx} & I_{yy} & -I_{yz} \\ -I_{zx} & -I_{zy} & I_{zz} \end{bmatrix}$$

where \mathbf{I}_{cm} is the inertia tensor and \mathbf{M}_{cm} is the net external moment acting on the aerostat with respect to its center of mass, cm . Due to the symmetry of the aerostat in the $x - z$ plane, the components I_{xy} and I_{yz} of the inertia tensor are zero.

The forces and moments which influence the aerostat are due to one of the following sources: gravity, buoyancy, aerodynamic and tether tension. The translational and rotational equations of motion of the aerostat can now be written as:

$$(mg - F_b) \sin \theta + F_{Hx} + F_{Px} + F_{Sx} + F_{Ux} + F_{Lx} = m(\dot{u} + qw - rv)$$

$$-(mg - F_b) \sin \phi \cos \theta + F_{Hy} + F_{Py} + F_{Sy} + F_{Uy} + F_{Ly} = m(\dot{v} + ru - pw)$$

$$-(mg - F_b) \cos \phi \cos \theta + F_{Hz} + F_{Pz} + F_{Sz} + F_{Uz} + F_{Lz} = m(\dot{w} + pv - qu)$$

$$-z_b F_b \sin \phi \cos \theta + M_{Hx} + M_{Px} + M_{Sx} + M_{Ux} + M_{Lx} = I_{xx} \dot{p} - (I_{yy} - I_{zz})qr - I_{xz}(\dot{r} + pq)$$

$$-x_b F_b \cos \phi \cos \theta - z_b F_b \sin \theta + M_{Hy} + M_{Py} + M_{Sy} + M_{Uy} + M_{Ly} =$$

$$I_{yy} \dot{q} - (I_{zz} - I_{xx})pr - I_{xz}(r^2 - p^2)$$

$$-x_b F_b \sin \phi \cos \theta + M_{Hz} + M_{Pz} + M_{Sz} + M_{Uz} + M_{Lz} = I_{zz} \dot{r} - (I_{xx} - I_{yy})pq - I_{xz}(\dot{p} - qr)$$

where F_H , F_P , F_S , F_U are the aerodynamic force contributions from the hull, port fin, starboard fin, upper fin, and F_L is the force exerted by the leash on the aerostat while F_b is the buoyancy force applied in the positive z-direction of the inertial frame and mg is the weight of the aerostat applied in the negative z-direction of the inertial frame. The angles ϕ , θ , ψ , represent the aerostat's roll, pitch and yaw. The left-hand side of the equations represents the external forces and moments acting on the aerostat whereas the right-hand side represents the aerostat's motion.

2.5.2 Component Breakdown Method

The aerodynamic forces and moments on the aerostat are calculated by breaking down the aerostat into components with known aerodynamic characteristics. This approach is based on the method developed by Nahon for modeling of underwater vehicles [24]. The individual components are the hull and the three aft fins. The method for calculating the effects of each component is as follows:

- calculate the motion at a reference point on each component,
- calculate the local angle of attack and sideslip angle,
- calculate the lift and drag forces and moments,
- transform these forces to the body frame,
- sum up the forces and moments.

To calculate the motion at a reference point on each component requires setting up a local frame on that component. The local frames for the hull and the three fins will be located at their respective centres of pressure. The method for calculating the location of the centre of pressure for the hull will be described in a later section.

For the fins, the location of the centre of pressure is taken to be at their $\frac{1}{4}$ chord line midway from the base to the tip. The location and orientation for each fin frame is shown in Figure 2.21. The velocity of the origin of the local frame for a particular fin, \mathbf{V}_L can be found using the relationship:

$$\mathbf{V}_L = \mathbf{V}_B + \boldsymbol{\omega} \times \mathbf{r}_L$$

where \mathbf{V}_B is the velocity at the origin of the body frame, while \mathbf{r}_L is the position vector from the origin of the body frame to the origin of the local frame or, specifically, from the centre of mass of the body to the centre of pressure of the component. Once the velocity of the centre of pressure of each component is found, it must be expressed with respect to its local frame. The local frame for the upper fin has the same orientation as the body frame so the velocity calculated above is the same as the velocity expressed in its local frame. By contrast, the orientations of the local frames for the two dihedral fins differ from that of the body frame. Therefore, to obtain the velocity of each dihedral fin in its own local frame, \mathbf{V}_i the velocity vector must be rotated by an appropriate angle.

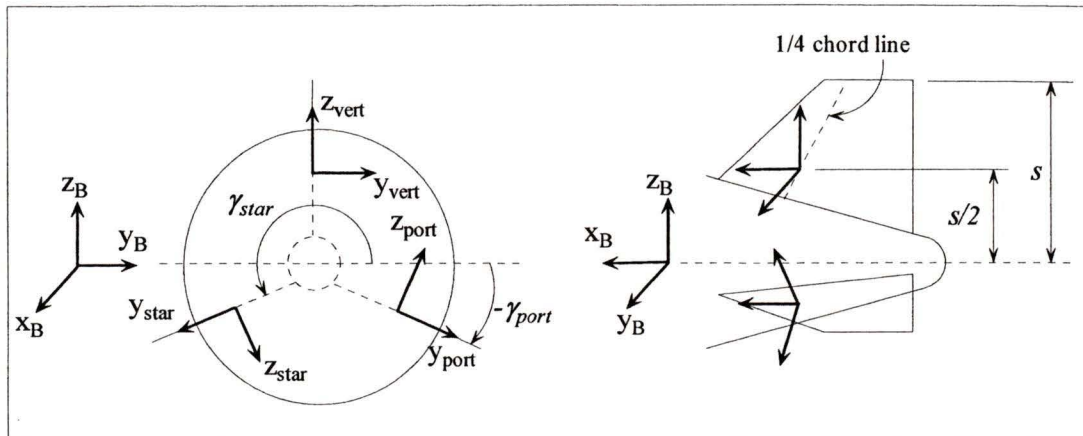


Figure 2.21: Front and side view of aerostat with location and orientation of local frame at the center of pressure of each fin.

This can be accomplished by applying a rotation matrix for a rotation about the x-axis by an angle γ as follows:

$$\mathbf{V}_i = [\mathbf{R}_x] \mathbf{V}_L, \quad \mathbf{R}_x = \begin{bmatrix} 1 & 0 & 0 \\ 0 & \cos \gamma & \sin \gamma \\ 0 & -\sin \gamma & \cos \gamma \end{bmatrix}$$

where $\mathbf{V}_i = [u_i \ v_i \ w_i]^T$. For the starboard fin the angle of rotation, $\gamma_{star} = 180^\circ + 22.5^\circ$, while for the port fin, $\gamma_{port} = -22.5^\circ$. The local angle of attack, α_i and sideslip angle, β_i can now be calculated for each component using the relationships:

$$\alpha_i = \tan^{-1}\left(\frac{w_i}{u_i}\right) \quad \beta_i = \tan^{-1}\left(\frac{v_i}{u_i}\right)$$

For the vertical tail fin, definitions for the sideslip angle, β and the angle of attack, α are reversed since the fin is vertical rather than horizontal. These parameters are represented schematically in Figure 2.22.

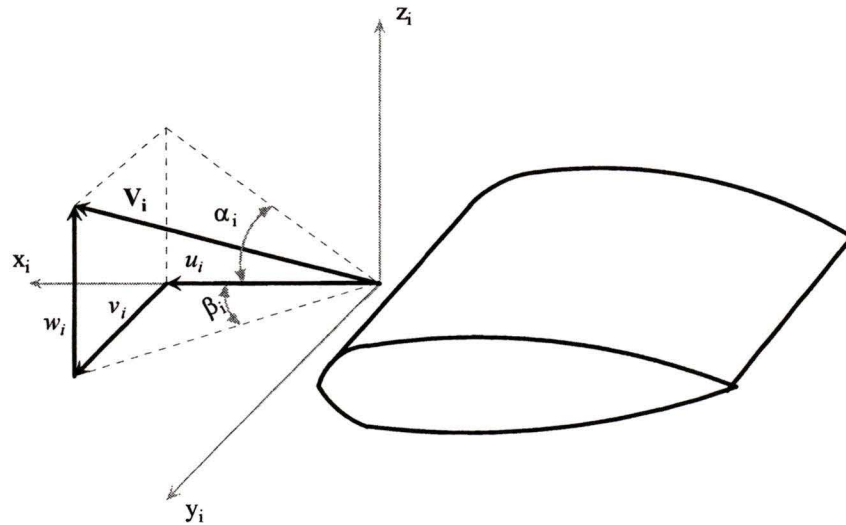


Figure 2.22: Angle of attack, α_i , and sideslip angle β_i , for an airfoil.

The aerodynamic forces of each component can now be estimated using local velocities and approach angles. The estimation method for the fins will use established methods for airfoils, while for the hull, a technique developed specifically for airships by Delaurier and Jones will be used [16].

2.5.3 Aerodynamic Forces of the Fins

The fins are approximated as NACA 0018 airfoils and the forces on each fin are characterized as lift, L and drag, D . The lift and drag forces for the fins are dimensionalized using the following equations:

$$L_i = \frac{1}{2} \rho A_f V_i^2 C_L \quad D_i = \frac{1}{2} \rho A_f V_i^2 C_D$$

where ρ is the density of air, A_f is the planform area of the fin, V_i is the local velocity of each fin, $V_i = \sqrt{u_i^2 + v_i^2 + w_i^2}$ and C_L and C_D are the lift and drag coefficients. C_L can be estimated using the empirical relationship between the 2-D lift coefficient and the angle

of attack. A linear fit to the curve for the region $0 < \alpha < \alpha_{stall}$, where α_{stall} is the stall angle, will be used to calculate the 2-D lift coefficient. The region of the lift curve past the stall angle, $\alpha > \alpha_{stall}$, is taken to be flat with the lift coefficient retaining its maximum value. This is considered reasonable in the case of low aspect ratio airfoils [14]. The 3-D lift coefficient can be calculated for a particular aspect ratio using:

$$C_L = C_{L\alpha}\alpha, \quad C_{L\alpha} = C_{l\alpha} \frac{A}{A+2 \left(\frac{A+4}{A+2} \right)}$$

where $C_{l\alpha}$ is the slope of the 2-D lift curve, A is the aspect ratio and $C_{L\alpha}$ is the slope of a 3-D lift curve [23].

The drag force on the fin is due to two different effects termed the parasitic drag and the induced drag. The drag coefficient, C_D is calculated by including both effects using the following equation:

$$C_D = C_{D_o} + \frac{C_L^2}{\pi A e}$$

where C_{D_o} is the parasitic drag coefficient and e is the Oswald's efficiency factor. It is important that if the airfoil has exceeded its stall angle, the C_L used in this equation is calculated using the actual attack angle, α to reflect the additional drag beyond the stall point.

Using these equations, the lift and drag forces are oriented according to the relative velocity of the fin. The lift force, L_i is directed normal to the direction of motion while the drag force, D_i acts in the opposite direction of the velocity vector as shown in Figure 2.23. The reason the direction of the lift force is directed downwards which is opposite to the common depiction of lift is because of our convention for assigning the z-

direction in an upward direction. For use with the equations of motion outlined earlier, these forces must be resolved into the aerostat's body frame. This can be achieved by first performing a simple rotation about the fin's local y -axis. In the case of the dihedral fin, this is then followed by a rotation from the local frame into the body frame, as follows:

$$\mathbf{F}_i = \mathbf{R}_x^T \mathbf{R}_y \begin{bmatrix} -D_i \\ 0 \\ -L_i \end{bmatrix} = \begin{bmatrix} 1 & 0 & 0 \\ 0 & \cos \gamma & -\sin \gamma \\ 0 & \sin \gamma & \cos \gamma \end{bmatrix} \begin{bmatrix} \cos \alpha_i & 0 & -\sin \alpha_i \\ 0 & 1 & 0 \\ \sin \alpha_i & 0 & \cos \alpha_i \end{bmatrix} \begin{bmatrix} -D_i \\ 0 \\ -L_i \end{bmatrix}$$

where $\mathbf{F}_i = [F_{ix} \ F_{iy} \ F_{iz}]^T$ is vector of the resultant force expressed in the body frame. For inclusion with the rotational equations of motion, the resulting moment, \mathbf{M}_i is calculated using a cross-product of the fin force vector with a position vector from the centre of mass of the aerostat to the centre of pressure of each fin as follows:

$$\mathbf{M}_i = \mathbf{r}_L \times \mathbf{F}_i$$

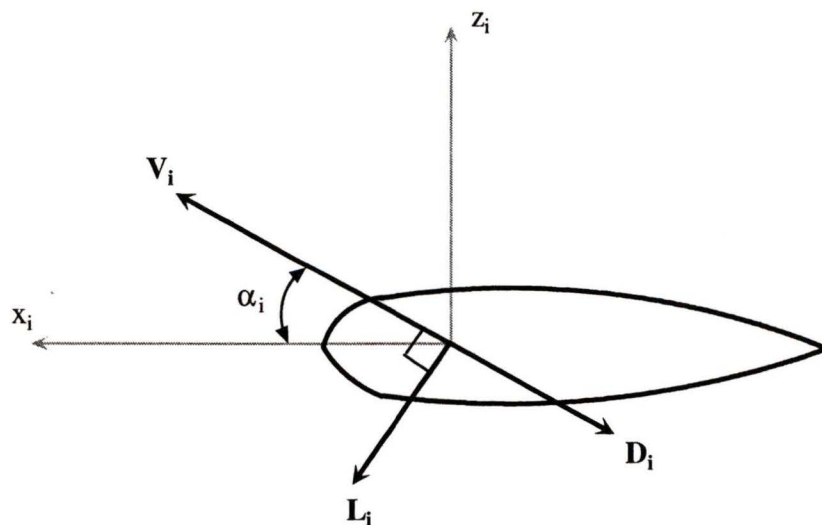


Figure 2.23: Lift and drag forces relative to fin motion.

2.5.4 Aerodynamic Forces of the Hull

Using the method from Jones and Delaurier [16] the aerodynamic influence of the hull was estimated by a lift and drag force and a pitch moment. The lift force is termed the normal force, N_h and along with the drag force, D_h it is considered to be applied at the nose of the aerostat. The pitch moment about the nose, M_{nose} accounts for the pitching tendencies of the aerostat. These quantities are calculated using the following equations:

$$\text{lift : } N = q_o [(k_3 - k_1)\eta_k I_1 \sin(2\alpha) \cos(\frac{\alpha}{2}) + (Cd_c)_h J_1 \sin \alpha \sin |\alpha|] \quad (2.6)$$

$$\text{drag : } D = q_o [(Cd_c)_o S_h \cos^2 \alpha - (k_3 - k_1)\eta_k I_1 \sin(2\alpha) \cos(\frac{\alpha}{2})] \quad (2.7)$$

$$\text{moment : } M_{nose} = -q_o [(k_3 - k_1)\eta_k I_3 \sin(2\alpha) \cos(\frac{\alpha}{2}) + (Cd_c)_h J_2 \sin \alpha \sin |\alpha|] \quad (2.8)$$

where:

$$q_o = \text{steady state dynamic pressure} = \rho V_B^2 / 2$$

ρ = density of atmosphere

$$V_B = \text{total velocity of the aerostat} = \sqrt{u^2 + v^2 + w^2}$$

α = hull angle of attack

k_1, k_3 = axial and lateral added-mass coefficients respectively

η_k = hull efficiency factor accounting for the effect of the fins on the hull

$(Cd_c)_h$ = hull cross-flow drag coefficient, referenced to J_1

$(Cd_h)_o$ = hull zero-angle axial drag coefficient, referenced to S_h

S_h = hull reference area = $(\text{hull volume})^{2/3}$.

Also,

$$I_3 = \int_0^{l_h} \xi \frac{dA}{d\xi} d\xi \quad \text{and} \quad I_1 = \int_0^{l_h} \frac{dA}{d\xi} d\xi = A_h$$

$$J_2 = \int_0^{l_h} 2r\xi d\xi \quad \text{and} \quad J_1 = \int_0^{l_h} 2rd\xi$$

where A is the cross sectional area of the hull, ξ is the axial distance along the hull from the nose and r is the hull radius. The values for I_1 , I_3 , J_1 and J_3 are based on the geometry of the aerostat. In order to utilize these equations it is required to split the aerostat into two regions; the hull region which extends from the nose to the starting point of the fins, and the fin region from this point to the tail. Figure 2.24 shows a 2-D diagram of the aerostat and the various aerodynamic parameters. The moment calculated about the nose, M_{nose} of the aerostat is not appropriate for our simulation since the equations of motion sum the moments at the centre of gravity of the aerostat, illustrated in Figure 2.25.

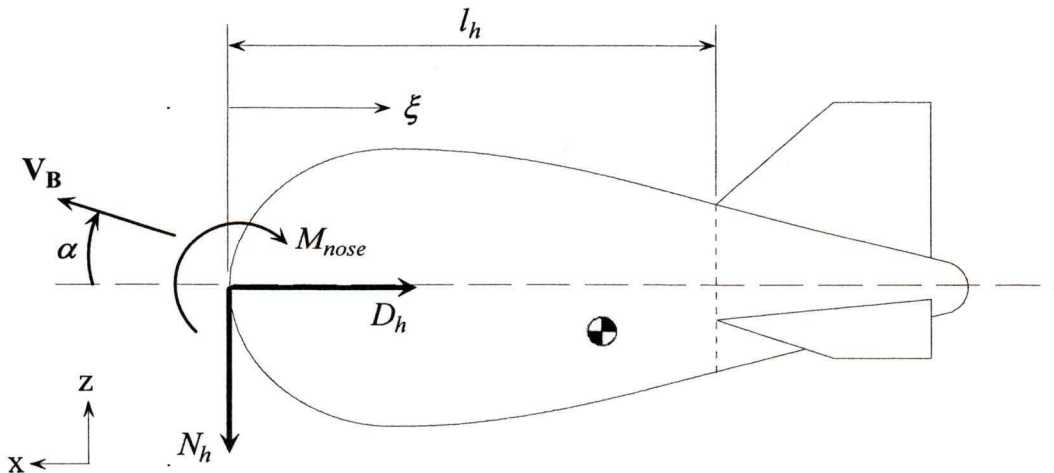


Figure 2.24: Schematic of aerodynamic parameters.

In order to account for this, the force/moment system N_h , D_h , M_{nose} was replaced by an equivalent system at the aerostat's center of pressure, c.p. The center of pressure is the point at which the moment of the force/moment system becomes zero. It is located along the centre-line of the aerostat at a distance from the nose which is determined at each time step of the simulation. The distance from the nose to the c.p., x_n is calculated by equating M_{nose} to the moment generated about the nose by the lift force, N_h using the following equation:

$$-M_{nose} = N_h(-x_n)$$

Using the convention of Jones and Delaurier [16], the orientation of the lift and drag forces on the hull follows a different convention than that of the fins. For the fins, the forces are directed according to the fin's motion, while the hull forces are directed according to its body axis independent of the direction of motion. The lift force acts perpendicular to the aerostat's central axis (x-direction in the body frame) while the drag force acts in the negative x-direction.

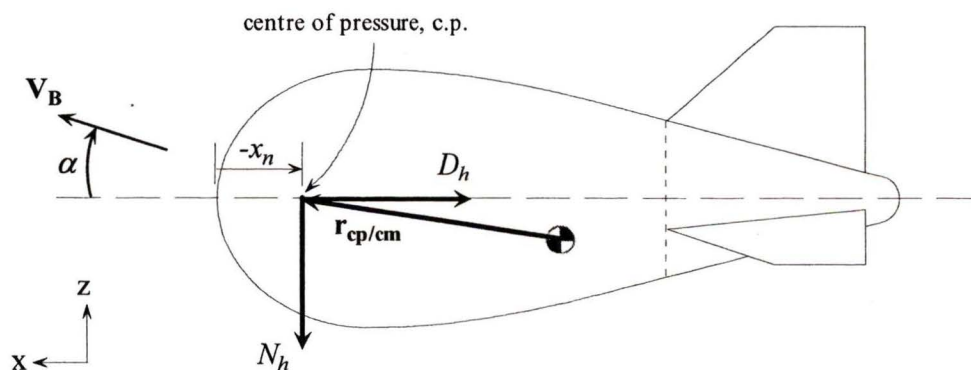


Figure 2.25: Aerodynamic parameters with M_{nose} replaced by forces applied at center of pressure.

The configuration of the aerostat shown previously are for a 2-D representation. Figure 2.26 shows the motion variables and hull forces for 3-D motion. The angle of attack of the hull, α and the angle of the lift force in the yz -plane, ϕ are found using the motion variables as follows:

$$\alpha = \cos^{-1}\left(\frac{u}{V_B}\right) \text{ and } \phi = \tan^{-1}\left(\frac{v}{w}\right)$$

In order to represent the aerodynamic forces in the body frame, the lift and drag forces are transformed as follows:

$$\mathbf{F}_h = \begin{bmatrix} F_{hx} \\ F_{hy} \\ F_{hz} \end{bmatrix} = \begin{bmatrix} 1 & 0 & 0 \\ 0 & c\phi & s\phi \\ 0 & -s\phi & c\phi \end{bmatrix} \begin{bmatrix} -D_h \\ 0 \\ -N_h \end{bmatrix}$$

For the rotational equations of motion, the resultant moment, \mathbf{M}_{cm} about the centre of mass can be found using the equation:

$$\mathbf{M}_{cm} = \mathbf{r}_{cp/cm} \times \mathbf{F}_h$$

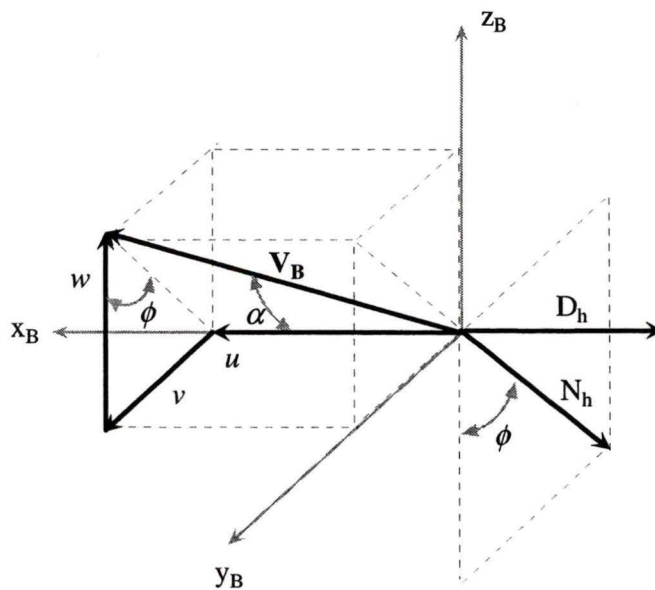


Figure 2.26: Orientation of the hull motion and forces.

2.5.5 Added Mass

The disruption caused by the aerostat's presence in the flow field causes fluid particles to accelerate as they are forced around the exterior of the body. Therefore, the fluid acquires kinetic energy through its interaction with the aerostat [27]. In certain cases, this transfer of energy to the fluid is significant and must be included in the dynamics model of the body. The conventional approach for inclusion of this effect is in the form of 'added mass' and 'added moments of inertia' to the body. The effective mass of the aerostat, m_e which will replace m in the motion equations can be found by summing the true mass, m and the added mass, m_a as follows:

$$m_e = m + m_a$$

where $m_a = k\rho V$ and k = added mass coefficient, and ρ = atmospheric density and V = volume of the aerostat. The dimensionless added mass coefficients for ellipsoidal shapes are provided in [27].

2.5.6 Tether Attachment

A tether is used to constrain the motion of the aerostat and this must be accounted for in the dynamics model by combining the aerostat and tether models. The coupling of the tether model and the aerostat model was achieved by connecting the uppermost node of the tether to the base of the aerostat's flying lines as shown in Figure 2.27. The aerostat and its flying lines (everything within the dashed box) are treated as a single rigid body. Hence, the two flying lines shown can be interpreted as rigid members. In reality, for an

aerostat of this type, many flying lines would be present and arranged in a harness (see Figure 2.19) in order to rigidly secure the aerostat. It would be difficult to incorporate the effects of the flexibility of a complex harness and therefore the rigid body approximation is deemed adequate for this level of investigation. The force from the top node of the tether or leash, F_1 is included in the equations of motion of the aerostat. For the rotational equations of motion, the moment from the leash force is calculated using:

$$\mathbf{M}_{\text{cm}} = \mathbf{r}_1 \times \mathbf{F}_1 \quad \text{where} \quad \mathbf{r}_1 = \begin{bmatrix} x_l \\ 0 \\ z_l \end{bmatrix}$$

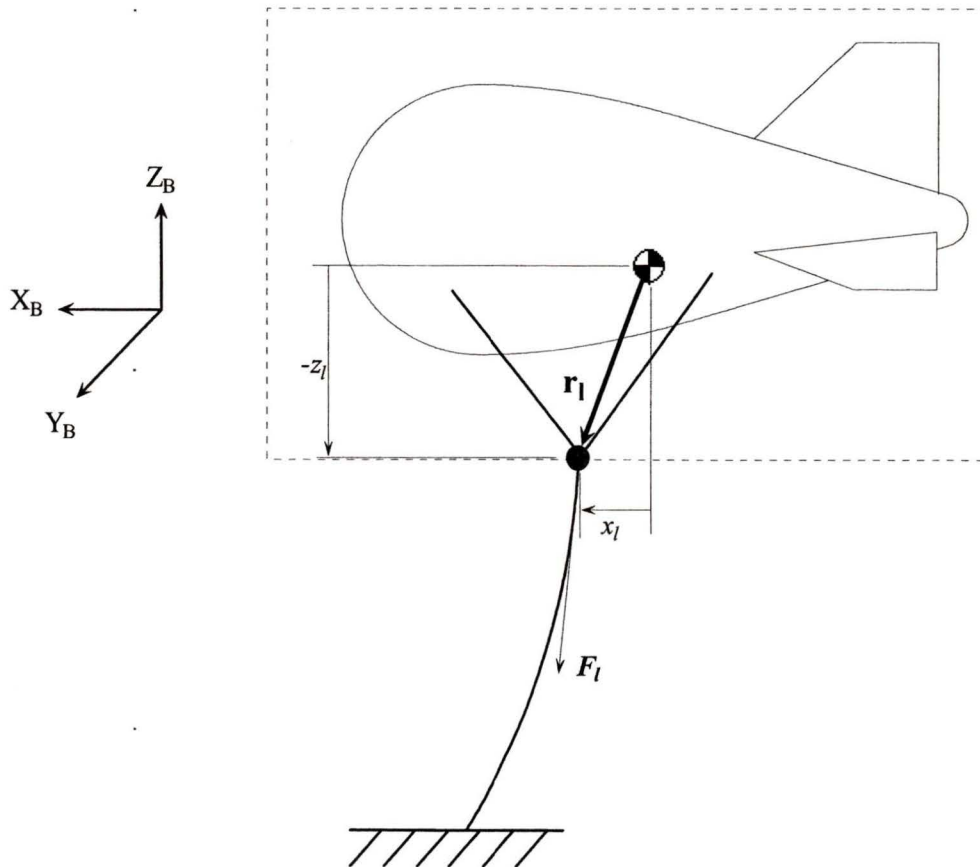


Figure 2.27: Connection point of tether and aerostat.

The actual location of the attachment point relative to the aerostat can have a significant effect on the behavior of the aerostat. Aeros Flightcam offered some general insights as to where to place the leash attachment point, based on their experience with tethered aerostats. It was recommended that, in the interests of stability, the aerostat should have a pitched up attitude of about 5 to 10° and that the vertical distance of the attachment point from the aerostat centreline, z_l should be about 1½ times the aerostat diameter.

The distance x_l was calculated to yield the selected pitch angle by summing the moment about the aerostat's centre of mass in a zero wind equilibrium position shown in Figure 2.28. The moment equation is as follows:

$$-F_b x_b \cos \theta - F_b z_b \sin \theta + F_{lz} x_l \cos \theta + F_{lz} z_l \sin \theta = 0$$

which can be rearranged as:

$$\tan \theta = \frac{F_b x_b - F_{lz} x_l}{F_{lz} z_l - F_b z_b} \quad 2.9$$

The buoyancy, F_b , the leash force, F_{lz} and the position of the centre of buoyancy, x_b and z_b are all fixed quantities for the aerostat. Therefore, once values for two of the other three remaining variables, θ , x_l and z_l are selected, this equation can be used to solve for the remaining variable. For our purposes, we selected a certain pitch angle, θ and vertical leash attachment position, z_l and solved for the unknown horizontal leash attachment position, x_l .

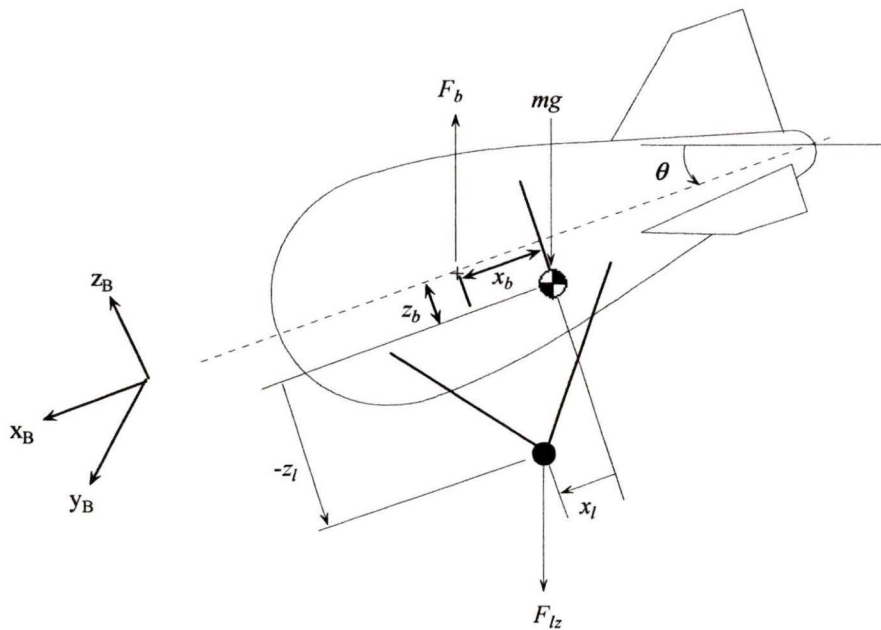


Figure 2.28: Rotation of aerostat in no-wind condition.

2.5.7 Physical Parameters

In order to solve the equations of motion outlined earlier, it is necessary to define numerous physical parameters for this particular aerostat. Figure 2.29 shows the overall dimensions of the Aeros aerostat and Table 2.8 gives relevant geometric parameters. The oval shape at the base of the body represents an internal balloon called a ‘ballonet’. It is a variable volume envelope filled with air which regulates the internal helium pressure by venting and accumulating air using electric blowers. The blowers are located at the base of the belly where the ballonet meets the hull. The tail fins are made from the same material as the hull and are inflated with helium. Multiple strands of nylon cord connect the face of each fin to the face of the adjacent fin. The nylon cord is cinched tight and the tension in the cords keeps the fins in place. The fins are arranged in an inverted Y configuration. The two dihedral fins are offset by an angle of 112.5° from the vertical fin.

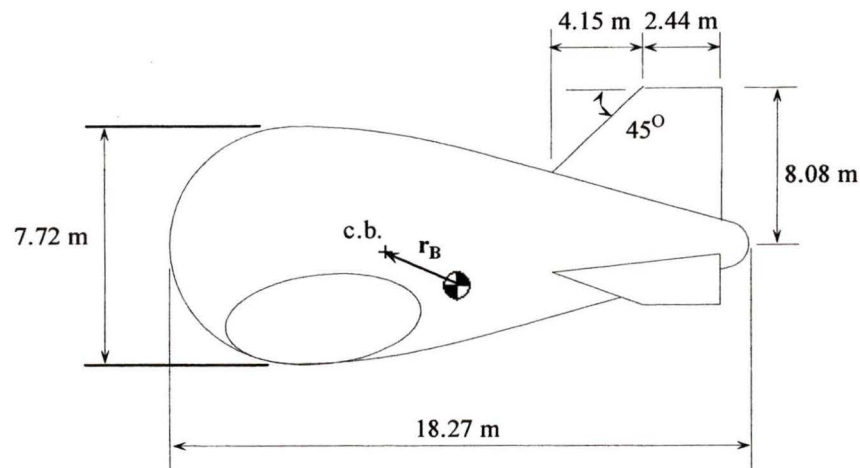


Figure 2.29: Aerostat with dimensions.

To obtain the physical parameters of the aerostat, a 3-D CAD model was generated using PRO-E. The CAD model was constructed to accurately represent the actual aerostat, complete with a thin-walled shell of the hull and ballonnet envelopes, solid models of the gases contained within and a plate which houses the blowers. The appropriate density was assigned to each part and the various physical parameters were computed by PRO-E. The mass and volume of the relevant parts are given in Table 2.8. Other parameters of interest obtained in this manner are the location of the aerostat's centre of buoyancy, c.b., the centre of mass, c.m., and the inertia tensor. The centre of buoyancy was found by obtaining the centre of mass for a solid, homogenous aerostat with the proper dimensions. From the values for the mass of the various components in Table 2.8 it is observed that the mass of the gases are a significant contribution to the overall mass of the aerostat. Typically when modeling vehicles, the vehicle mass and inertial parameters are not affected by the mass of internal gases, however for lighter than air vehicles it is essential to account for the internal gas volume when determining any physical parameters.

Table 2.8: Aeros physical parameters.

Parameter	Value	Parameter	Value
helium volume	467.1 m ³	centre of mass (from nose):	
ballonet volume	52.2 m ³	x_{cm}	-8.476 m
total volume	519.3 m ³	y_{cm}	0
helium mass	78.9 kg	z_{cm}	-0.491
air mass	64.2 kg	centre of buoyancy (from c.m.):	
hull mass	115.6 kg	x_b	0.710 m
ballonet mass	25.6 kg	y_b	0
blowers mass	10.0 kg	z_b	0.524 m
tail fin mass (all 3)	63.6 kg	inertia tensor components:	
total mass	357.9 kg	I_{xx}	3184 kg·m ²
density of air	1.229 kg/m ³	I_{yy}	10011 kg·m ²
density of helium	0.169 kg/m ³	I_{zz}	9808 kg·m ²
buoyancy	6260.7 N	$I_{xz} = I_{zx}$	-641 kg·m ²
net lift	2749.7 N		

2.5.7.1 Aerodynamic Parameters

The aerodynamic parameters used in the dynamics model must be estimated for this particular aerostat. The location of the centre of pressure for each component was calculated using the explanation given earlier and is listed in Table 2.9. All distances given are measured from the aerostat's centre of mass.

As noted earlier, the aerostat was split into two regions; the hull region which includes everything from the nose to the start of the fins and the fin region which includes the fins and the section of the hull back from the start of the fins. The area for each fin, A_f is the cross sectional area from the centre-line of the aerostat to the tip of the fin. The

aspect ratio of the fins is defined as the square of the distance from the aerostat's centre-line to the fin tip divided by A_f . The value of $C_{L\alpha}$ takes into account losses arising from the fins' location at the rear of the vehicle. The flow field in the vicinity of the fins will have experienced disruptions from passing over the hull, resulting in a reduction of the fins' capability to produce lift.

Table 2.9: Aerodynamic parameters of aerostat.

Parameter	Value	Parameter	Value
centre of pressure:		fins:	
hull		A_f	30.0 m ²
x_h	x_n	A	2.18
y_h	0	$C_{L\alpha}$	2.0
z_h	0.491 m	C_{D0}	0.012
vertical fin		α_{stall}	11.0°
x_v	-4.92 m	hull:	
y_v	0	k_1	0.16
z_v	3.74 m	k_3	0.76
port fin		η_k	1.1823
x_p	-4.92 m	$(Cd_c)_h$	0.8
y_p	2.98 m	$(Cd_h)_0$	0.0394
z_p	-0.706	S_h	59.35 m ²
starboard fin		I_1	20.43 m ²
x_s	-4.92 m	I_3	-108.4 m ³
y_s	-2.98 m	J_1	75.84 m ²
z_s	-0.706	J_2	650.49 m ³

The added mass coefficients, k_1 and k_3 were estimated using data for ellipsoids in [27]. The hull efficiency factor, η_k was found by averaging values given for six different aerostats from Jones and Delaurier in [16]. The cross-flow drag coefficient for the hull, $(Cd_c)_h$ was estimated using the drag coefficient for a cylinder. It should be mentioned that efforts should be made to obtain a cross-flow drag coefficient for a more representative shape; possibly a spheroid or from experimental data on similar lighter than air bodies. The estimation of the zero angle axial drag, $(Cd_h)_0$ was based on the drag coefficient for a streamlined shape with a fineness ratio of 2.4 [23], where the fineness ratio is the length of the body divided by its maximum diameter. The hull reference area, S_h is defined as the (hull volume)^{2/3}. The evaluation of the integral for I_1 gives the cross-sectional area of the hull at the hull fin region boundary, A_h . The integral for J_1 is equivalent to the cross-sectional area of the hull region of the aerostat in the xz-plane. The value for this was found using the CAD model and the evaluation tools of PRO-E. The integrals for I_3 and J_2 are not easily solved unless a closed form equation for the aerostat shape is available and in our case it was not. Therefore, to estimate these quantities, an average was used of equivalent non-dimensional terms given for six aerostat shapes in [16].

2.5.7.2 Tether Properties

The tether that was modeled has physical and aerodynamic parameters listed in Table 2.10. The *Plasma* tether is manufactured by Puget Sound Rope. The manufacturer provided the data for the density and strength of the cable. The damping ratio and elastic modulus were estimated from experimental data as presented in section 2.3.

Table 2.10: Tether parameters.

Parameter	Value
diameter, D_t	6 mm
density, ρ_t	840 kg/m ³
minimum strength	35.6 kN
elastic modulus, E	37.4 GPa
damping ratio, ζ	0.017

2.5.8 Results

To illustrate the dynamics model results, Figure 2.30 presents simulation output for the position and orientation of the Aeros aerostat on a single tether of $L = 100$ m. The system is initially in a static equilibrium position for the steady state wind speed imposed of $U = 6$ m/s. Turbulent gusts are superimposed on the wind speed which is directed towards the aerostat in the negative x-direction. Since the system is initially in static equilibrium the unsteady motion observed can be attributed solely to turbulence effects. The turbulence induced motion appears to be significant when considering the magnitude of the displacement is on the order of 5 m. However, considering that the length of the tether is 100 m and that the length of the aerostat is almost 20 m, a displacement of 5 m is not considered excessive. Also, the displacement of in the x and y-directions occurs at low frequencies (period > 10 s). When incorporated with the multi-tethered system, the effects of the low frequency aerostat motion should be easily controlled by the winch system. Figure 2.31 shows results for the tri-tethered case in the symmetrical configuration with the Aeros aerostat. The PID controller discussed earlier was used with gains of $k_p = 5$, $k_d = 1.5$ and $k_i = 1.5$. The stiffness and responsiveness of the system is

clear as the maximum position error of the payload is less than 8 mm while the aerostat's displacement reaches as high as 3 m. The aerostat motion is different for the tri-tethered case because the aerostat's leash is only 33.3 m compared to $L = 100$ m for the single tether case.

Further understanding the stability of the aerostat over a wide range of conditions is of prime importance and the dynamics model of the aerostat will be used to perform a stability analysis in Chapter 3.

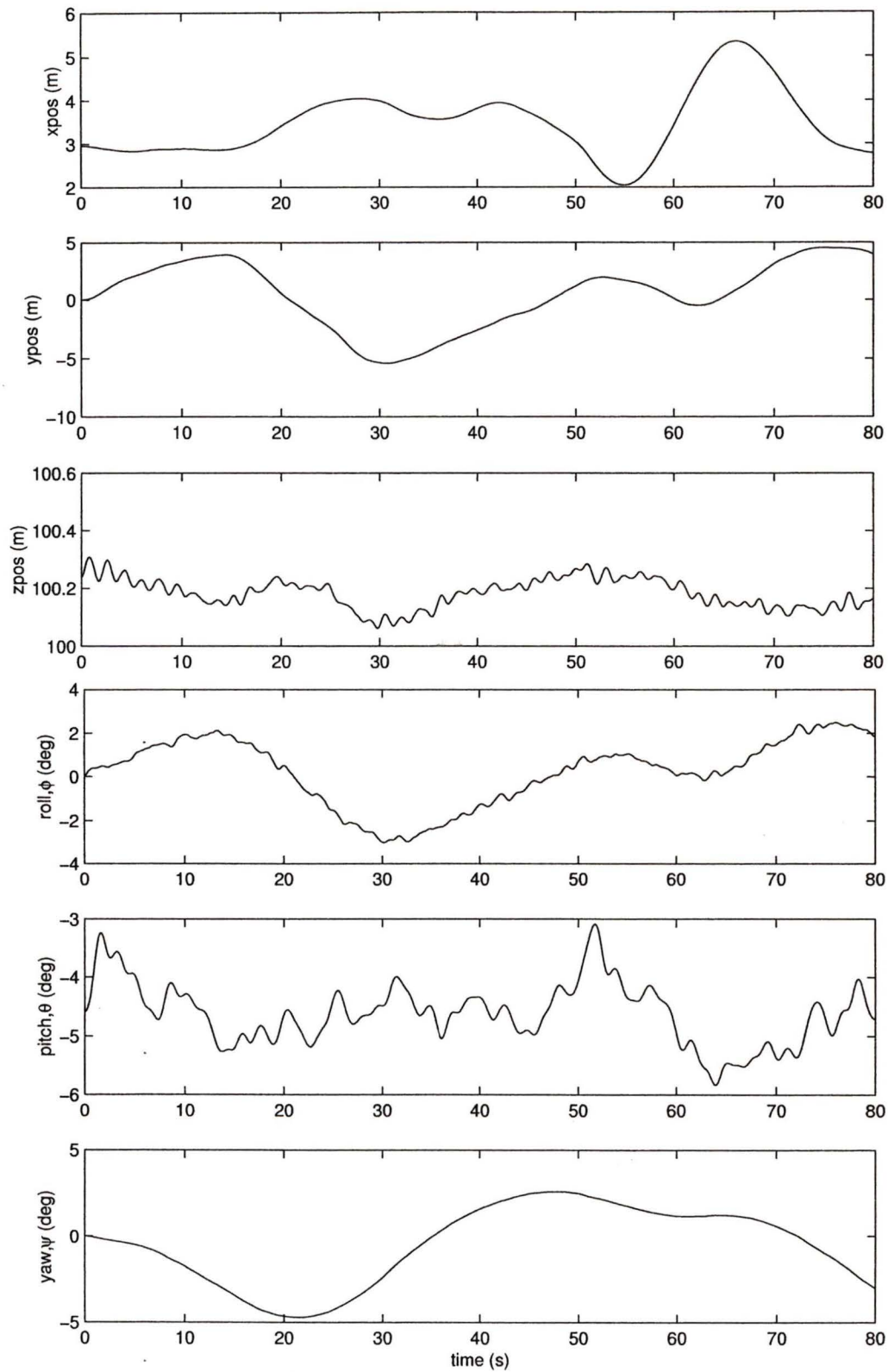


Figure 2.30: Position and orientation of streamlined aerostat on a single tether with $L = 100$ m, $U = 6$ m/s with turbulence.

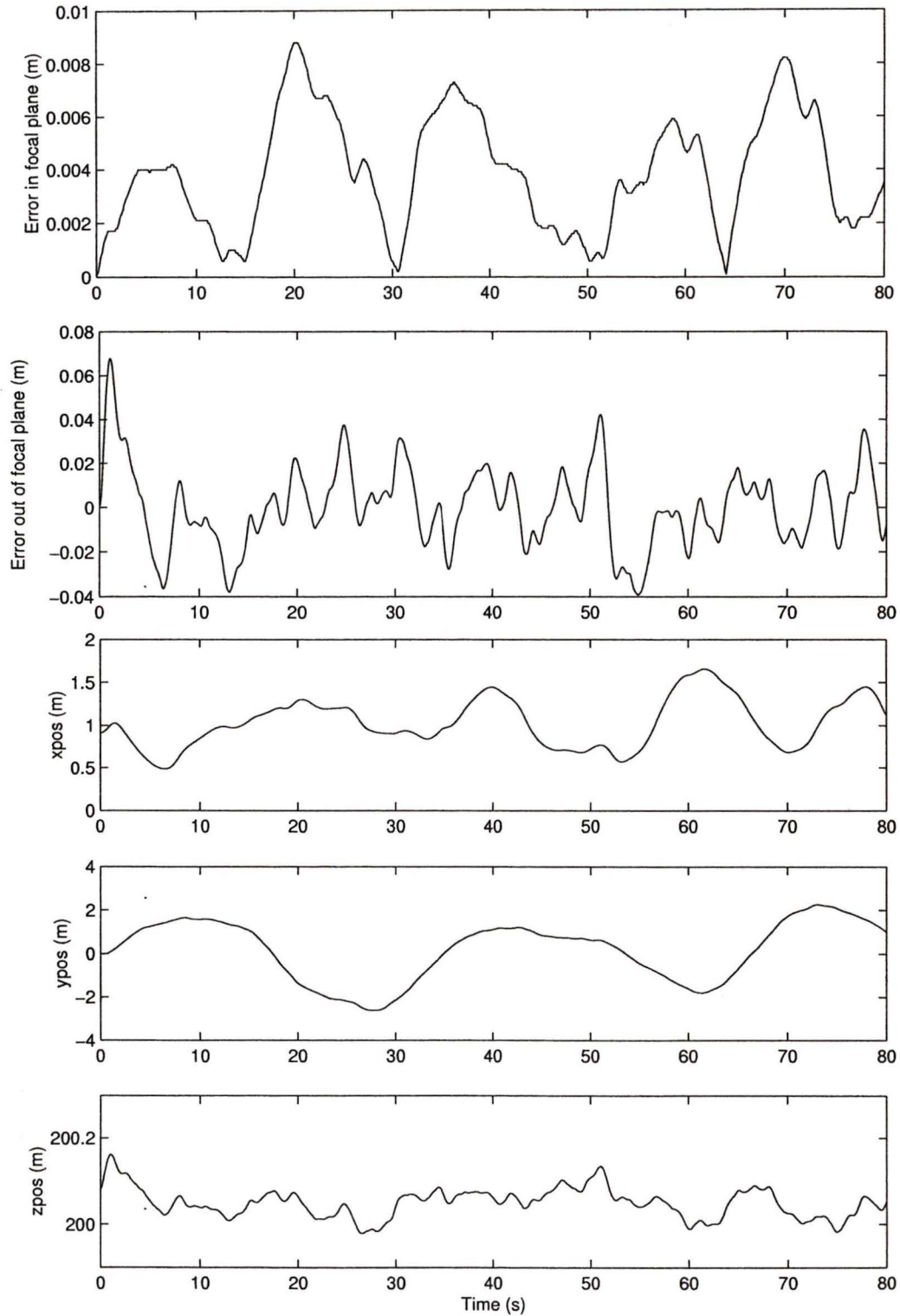


Figure 2.31: Payload error and aerostat position for tri-tethered case, $U = 6$ m/s with streamlined aerostat with turbulence and active control.

Chapter 3

Linear Stability Analysis

The nonlinear dynamics model of the streamlined aerostat on a single tether is useful for obtaining time histories of the aerostat's motion in response to a particular wind or winch input. However, in order to acquire a quantitative assessment of the stability of the aerostat, a linear approximation of the system was derived and its eigenvalues and eigenvectors were studied.

The dynamics simulation can be thought of as a set of functional relationships where the derivative of each state variable is dependent on the full set of state variables. This is demonstrated by the following equations:

$$\dot{\mathbf{X}} = \mathbf{F}(\mathbf{X}) \quad (3.1)$$

or:

$$\begin{aligned} \ddot{x}_1 &= f_1(\mathbf{X}) \\ \dot{x}_1 &= f_2(\mathbf{X}) \\ &\vdots \\ \dot{\psi} &= f_{6n+6}(\mathbf{X}) \end{aligned}$$

where $\mathbf{X} = [\dot{x}_1, x_1, \dot{y}_1, y_1, \dot{z}_1, z_1, \dots, \dot{x}_n, x_n, \dot{y}_n, y_n, \dot{z}_n, z_n, \dot{\phi}, \phi, \dot{\theta}, \theta, \dot{\psi}, \psi]^T$ is the state vector. It contains the position and velocity of all the discretized elements. This includes each of the tether nodes as well as the aerostat. For the aerostat node, there are an additional six state variables representing the rotational motion. Therefore, the total number of state variable is $6n + 6$, where n is the number of tether nodes. Note that there are no state variables for the bottom-most tether node since it is fixed to the ground. Hence the translational variables with the subscript n represent the aerostat node.

3.1 Linear Model

Linearizing equation (3.1) leads to:

$$\dot{\mathbf{X}} = \mathbf{A}\mathbf{X}$$

where the state matrix, \mathbf{A} is defined as:

$$\mathbf{A} = \frac{\partial \mathbf{F}}{\partial \mathbf{X}} = \begin{bmatrix} \frac{\partial f_1}{\partial \dot{x}_1} & \frac{\partial f_1}{\partial x_1} & \dots & \frac{\partial f_1}{\partial \psi} \\ \frac{\partial f_2}{\partial \dot{x}_1} & \frac{\partial f_2}{\partial x_1} & \dots & \frac{\partial f_2}{\partial \psi} \\ \vdots & \vdots & \ddots & \vdots \\ \frac{\partial f_{6n+6}}{\partial \dot{x}_1} & \frac{\partial f_{6n+6}}{\partial x_1} & \dots & \frac{\partial f_{6n+6}}{\partial \psi} \end{bmatrix}$$

The most direct method for obtaining the state matrix is to perform a numerical differentiation by finite difference of the nonlinear differential equations. The first step is to choose a reference equilibrium condition about which the system will be linearized. Next, each state variable will be perturbed slightly from its equilibrium value. The ensuing response of every state variable will be observed and compared to its equilibrium value. The difference between the response and the equilibrium value is divided by the

perturbation to approximate each element of the state matrix. For example, in the case of the first element in the first row, we have:

$$\frac{\partial f_1}{\partial \dot{x}_1} \approx \frac{f_1' - f_{1_0}}{\Delta \dot{x}_1}$$

where f_1' is the value of f_1 due to a perturbation of a particular state variable (in this case, \dot{x}_1), while f_{1_0} is the value of f_1 at the reference equilibrium condition and $\Delta \dot{x}_1$ is the perturbation value of \dot{x}_1 . The value for the perturbation is typically very small (10^{-5} was used). The reference equilibrium condition is one in which the tethered aerostat system is in a steady state wind field in the absence of turbulence. The process can be repeated for a variety of wind speeds in the range of interest.

Once **A** is formed, it is necessary to verify its validity through a comparison of the linear and nonlinear responses to a specified initial condition. To obtain the linear response, the Matlab function ‘initial’ was used. This function obtains the time response for a linear system. The nonlinear response was obtained using the dynamics model of the single tethered streamlined aerostat discussed in section 2.5. All six position variables for the aerostat were simultaneously given an initial perturbation from the equilibrium condition. The perturbation was 0.1 m for the translational variables and 0.01 rad for the rotational variables. The linear and nonlinear response for the position variables is shown in Figure 3.1. The good agreement between the two responses demonstrates the success of the linearization process and provides justification for pursuing the linear stability analysis.

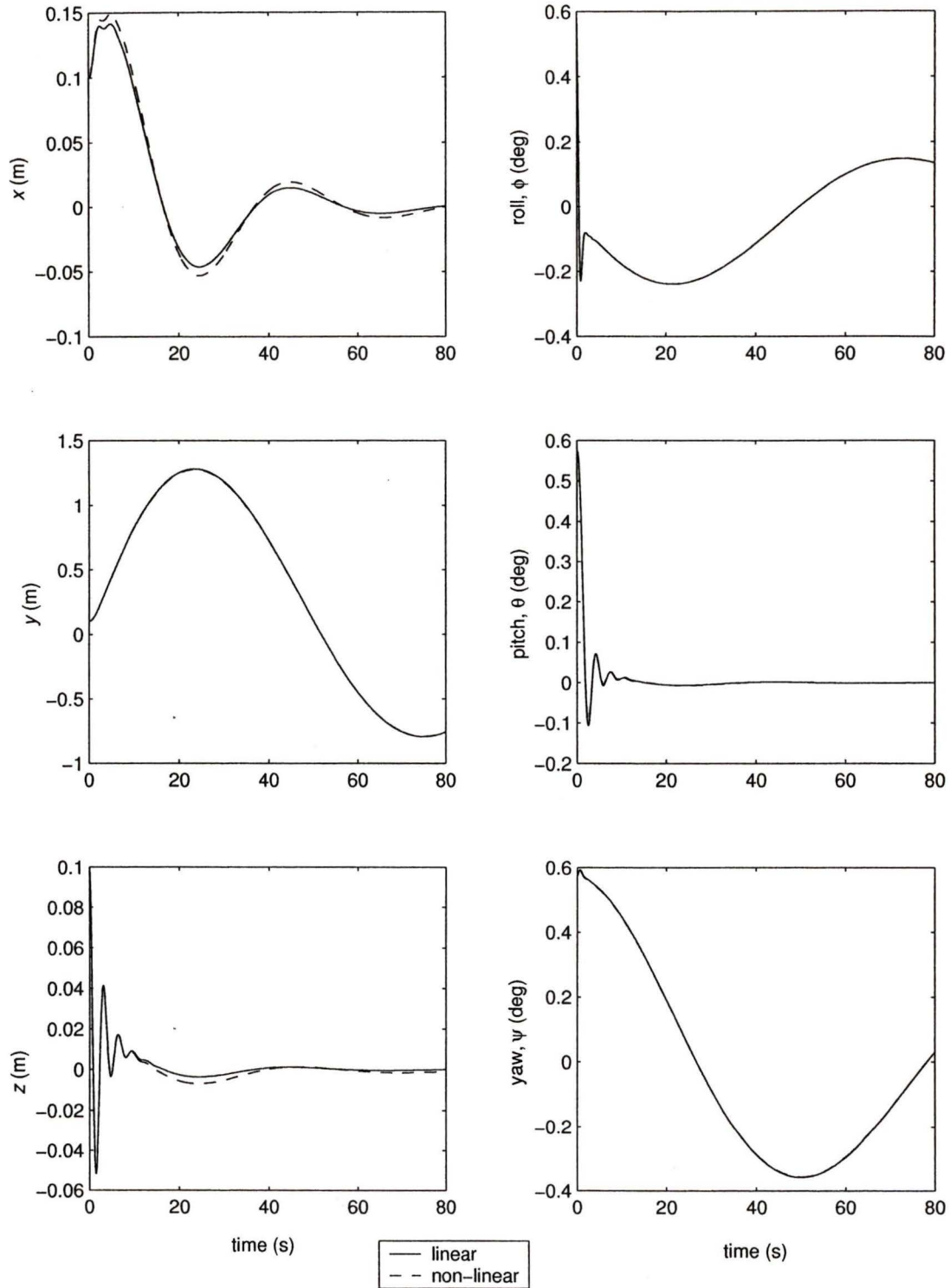


Figure 3.1: Comparison of linear (solid line) and non-linear (dashed line) simulation results of aerostat motion for case with single tether of $L = 300$ m tether and $U = 10$ m/s. The responses are identical in the regions where only one line is present.

3.2 Decoupling

The convention for analyzing the stability of vehicle models is to decouple the motion variables into lateral and longitudinal subsets [8]. The longitudinal variables are defined as translational motion in the x and z directions and rotational motion about the y-axis (i.e. $\dot{x}_{1..n}, x_{1..n}, \dot{z}_{1..n}, z_{1..n}, \dot{\theta}, \theta$). The lateral variables are defined as translational motion in the y-direction and the rotational motion about the x and z axes (i.e. $\dot{y}_{1..n}, y_{1..n}, \dot{\phi}, \phi, \dot{\psi}, \psi$). For a tethered aerostat symmetrical about the xz-plane it can be shown that longitudinal and lateral decoupling will occur [8]. To ensure that this holds true for our tethered aerostat system, the state vector and the state matrix were rearranged to separate the longitudinal and lateral systems. The new state vector, \mathbf{X}' is as follows:

$$\mathbf{X}' = \begin{bmatrix} \mathbf{X}_{long} \\ \mathbf{X}_{lat} \end{bmatrix} \text{ where } \mathbf{X}_{long} = \begin{bmatrix} \dot{x}_1 \\ x_1 \\ \dot{z}_1 \\ z_1 \\ \vdots \\ z_n \\ \dot{\theta} \\ \theta \end{bmatrix} \text{ and } \mathbf{X}_{lat} = \begin{bmatrix} \dot{y}_1 \\ y_1 \\ \vdots \\ y_n \\ \dot{\phi} \\ \phi \\ \dot{\psi} \\ \psi \end{bmatrix}$$

To be consistent with the new arrangement of \mathbf{X}' , the state matrix, \mathbf{A} must be rearranged by exchanging the appropriate row and column for each variable that was repositioned. Once this process is complete we can determine whether the longitudinal and lateral variables are, in fact, decoupled. If the longitudinal and lateral systems are decoupled, the new state matrix, \mathbf{A}' will be partitioned into 4 distinct sub-matrices; a longitudinal sub-matrix, \mathbf{A}_{long} and a lateral sub-matrix, \mathbf{A}_{lat} as well as two null sub-matrices. The dimensions of and location of each sub-matrix is as follows:

$$\mathbf{A}' = \begin{bmatrix} [\mathbf{A}_{long}]_{(4n+2) \times (4n+2)} & [\mathbf{0}]_{(4n+2) \times (2n+4)} \\ [\mathbf{0}]_{(2n+4) \times (4n+2)} & [\mathbf{A}_{lat}]_{(2n+4) \times (2n+4)} \end{bmatrix}$$

For our system, it was found that the lower left matrix was in fact comprised of all zeros, however the upper right sub-matrix matrix had several elements with small magnitudes. Since these values were quite small (the largest being on the order of 10^{-4}) compared to the magnitude of the elements of the other matrices (the largest being on the order of 10^4) it can be concluded that the motion is essentially decoupled. Therefore, the system can be analyzed as two separate systems as follows:

$$\begin{aligned} \dot{\mathbf{X}}_{long} &= \mathbf{A}_{long} \mathbf{X}_{long} \\ \dot{\mathbf{X}}_{lat} &= \mathbf{A}_{lat} \mathbf{X}_{lat} \end{aligned}$$

3.3 Eigenvalues and Eigenvectors

The aerostat's natural motion and stability is characterized by the eigenvalues and eigenvectors of the corresponding state matrix. Each eigenvalue (or pair of eigenvalues) represents a particular mode of the motion, while its corresponding eigenvector provides the relationship of each state variable in that mode. A system with N degrees of freedom will have N modes. Our system in state-space form has $2N$ state variables because each degree of freedom is represented by a corresponding displacement and velocity. For the single-tethered aerostat, the number of state variables is $6n + 6$ and hence the number of modes is $3n + 3$. Eigenvalues can exist as either complex conjugates denoted as $\lambda_{1,2} = \sigma \pm \omega_d i$, or as pairs of distinct real numbers denoted as $\lambda_{1,2} = \sigma_1, \sigma_2$. A complex conjugate pair of eigenvalues indicates that the mode is oscillatory, and a real eigenvalue indicates non-oscillatory motion. For stability of the system, all the real parts of the

eigenvalues must be negative. The motion characteristics determined from a complex eigenvalue are shown in Figure 3.2. The damped frequency, ω_d is the imaginary part of the eigenvalue and the natural frequency and damping ratio are found from:

$$\omega_n = \sqrt{\sigma^2 + \omega_d^2}$$
$$\zeta = \sin \theta = \frac{\sigma}{\omega_n}$$

where ω_n is the natural or undamped frequency and ζ is the damping ratio.

Each eigenvalue of a complex conjugate pair has a conjugate that is a reflection about the real axis. Both eigenvalues correspond to a single mode with a particular frequency and damping ratio. Each element of the corresponding eigenvector represents the magnitude and phase of the response of a particular state variable.

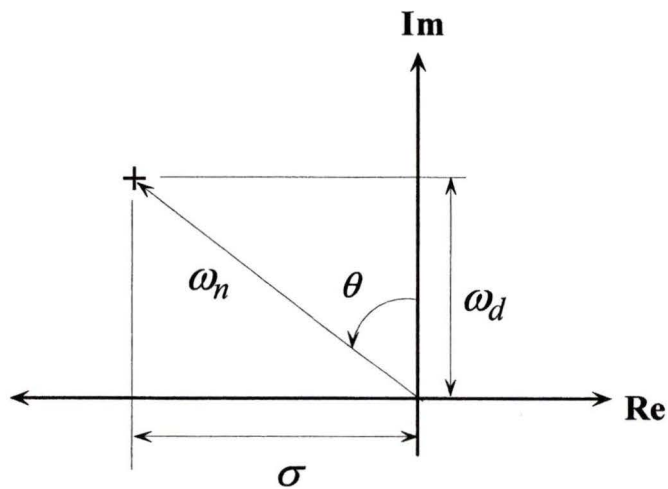


Figure 3.2: Complex representation of eigenvalue.

If phasor representation for the members of eigenvectors is considered, the radius corresponds to the magnitude of the response and the angle corresponds to the phase. It is important to note that the magnitude and phase of the state variables obtained from the eigenvectors are relative to each other and are not absolute. In the case of complex conjugate eigenvalues, the corresponding eigenvectors are also complex conjugates mirrored about the real axis.

For a real eigenvalue, the motion is characterized by t_2 , the time to double amplitude (unstable---positive σ) or by $t_{1/2}$, the time to half amplitude (stable---negative σ) which are given as follows:

$$t_2 \text{ or } t_{1/2} = \frac{0.693}{|\sigma|}$$

3.4 Results

The Matlab function 'eig' was used to compute the eigenvalues and eigenvectors for \mathbf{A}_{long} and \mathbf{A}_{lat} . Because the number of modes for this system is large, it was decided to only study the four lowest frequency modes in each subsystem, since the high frequency modes are not likely to yield significant motion in the actual system.

The results for a baseline case are presented in Figure 3.3. The conditions for this case are: tether length, $L = 300$ m with a steady-state pitch angle, $\theta_0 = -4^\circ$ (pitched up). All other physical parameters correspond to the values presented for the Aeros Aerostat in Chapter 2. The four longitudinal and four lateral modes considered here were found to be stable over the full range of wind speeds. The remaining modes omitted from the presentation were observed to be stable as well.

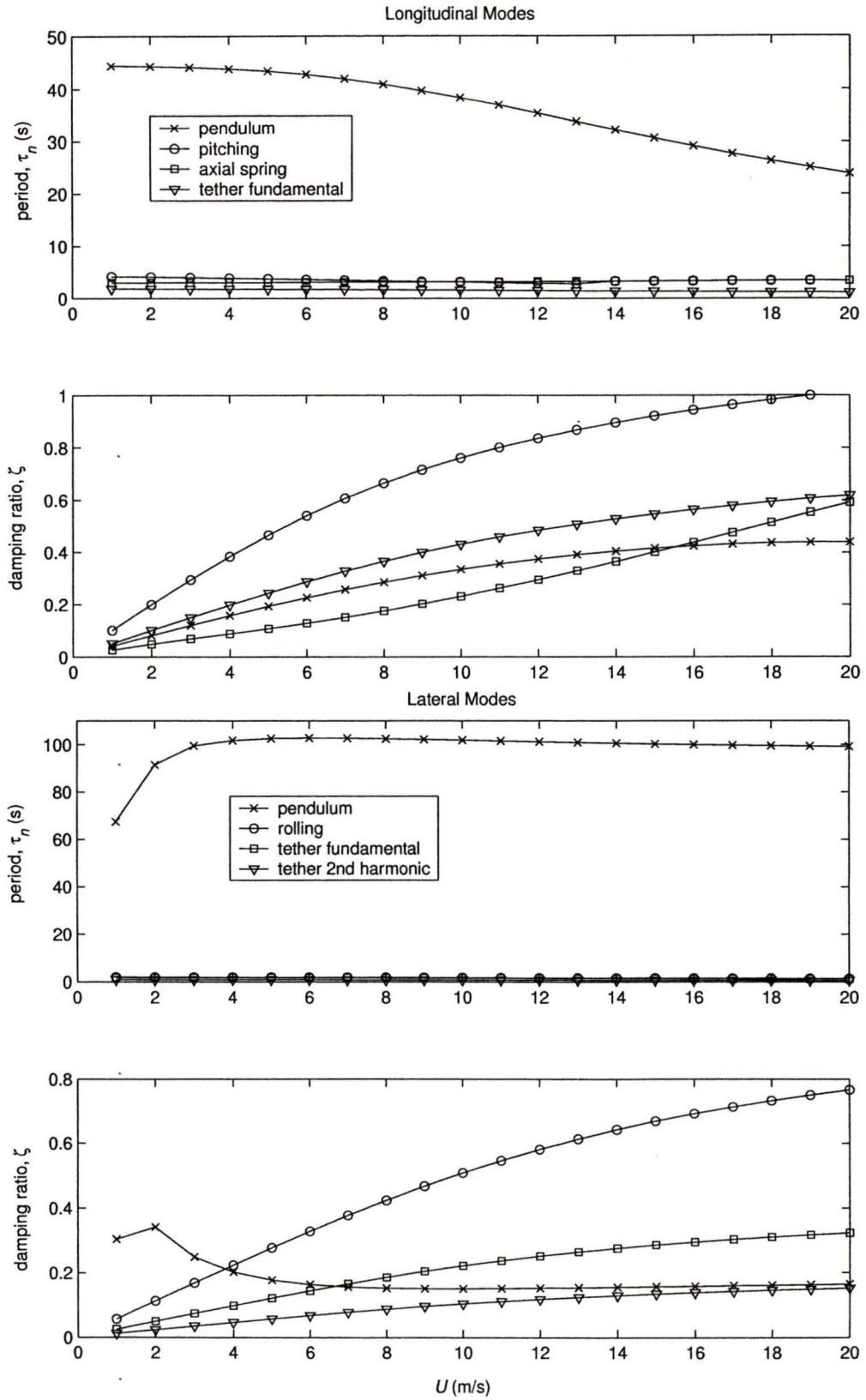


Figure 3.3: Longitudinal and lateral modes for baseline case with $L = 300$ m, $\theta_0 = -4^\circ$.

To gain a better appreciation of the results, the eigenvectors for each of the modes were studied in attempt to classify the motion. For brevity, only the method of classification for the lateral modes is presented. The eigenvectors for the four lowest frequency lateral modes with $U = 1$ m/s are presented in graphical form in Figure 3.4 and in numerical form in Table 3.1. Both sets of the eigenvectors are plotted in Figure 3.4 as can be observed in the symmetry about the real axis. However, since the relevant information about the mode can be obtained with just one set of eigenvectors, only one set was included in Table 3.1.

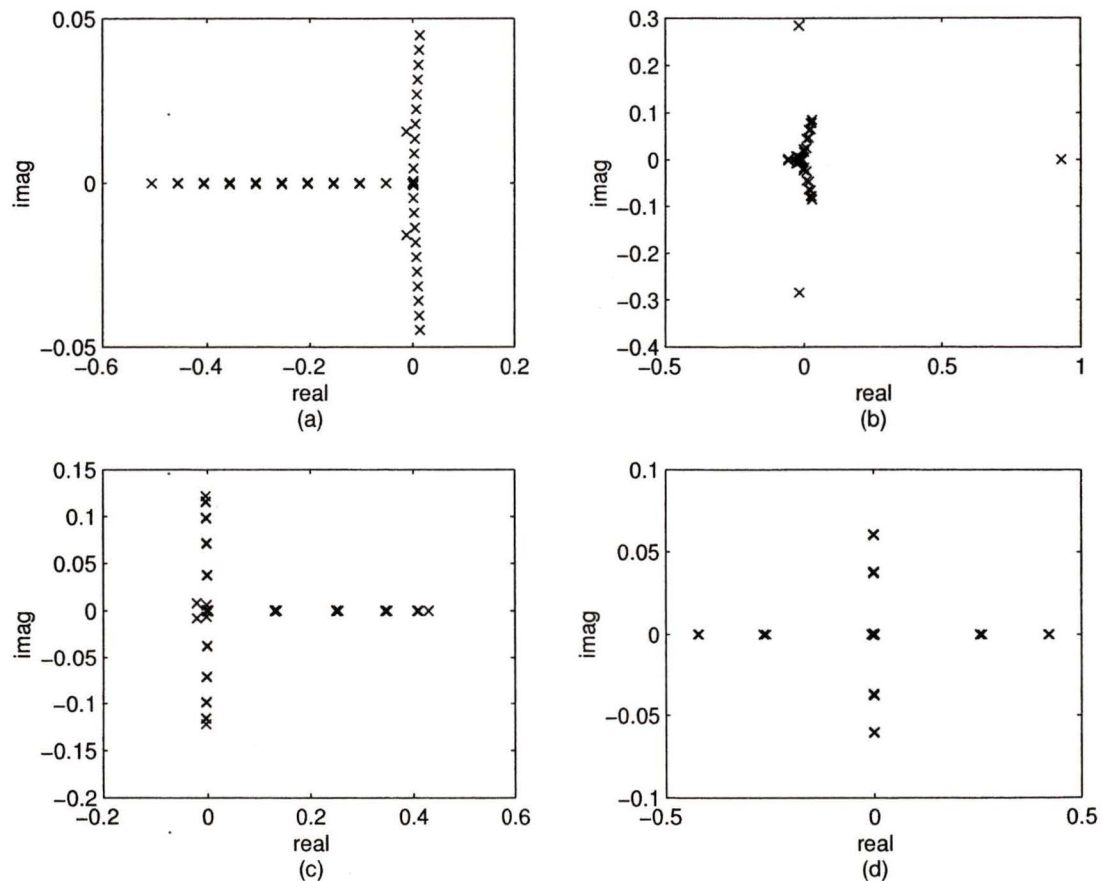


Figure 3.4: Eigenvectors for 4 lowest frequency lateral modes: a) pendulum, b) rolling, c) 1st tether harmonic and d) 2nd tether harmonic for baseline case at $U = 1$ m/s.

Table 3.1: Lateral eigenvectors for low frequency modes of baseline case at $U=1$ m/s.

	a) pendulum	b) rolling	c) 1 st tether	d) 2 nd tether
\dot{y}_1	0.0014+0.0046i	0.0094+0.0246i	0.1342+0.0001i	0.2624+0.0000i
y_1	-0.0512-0.0001i	-0.0077+0.0024i	-0.0010+0.0380i	-0.0004+0.0377i
\dot{y}_2	0.0029+0.0091i	0.0178+0.0470i	0.2548+0.0001i	0.4229
y_2	-0.1023-0.0001i	-0.0147+0.0046i	-0.0018+0.0722i	-0.0007+0.0607i
\dot{y}_3	0.0043+0.0136i	0.0245+0.0655i	0.3500+0.0001i	0.4204-0.0000i
y_3	-0.1533-0.0002i	-0.0204+0.0063i	-0.0025+0.0991i	-0.0007+0.0604i
\dot{y}_4	0.0057+0.0181i	0.0288+0.0786i	0.4104+0.0001i	0.2566-0.0001i
y_4	-0.2041-0.0003i	-0.0245+0.0074i	-0.0029+0.1163i	-0.0004+0.0368i
\dot{y}_5	0.0072+0.0226i	0.0303+0.0852i	0.4304	-0.0049-0.0001i
y_5	-0.2548-0.0003i	-0.0266+0.0078i	-0.0030+0.1219i	0.0000-0.0007i
\dot{y}_6	0.0086+0.0271i	0.0288+0.0848i	0.4081-0.0001i	-0.2639-0.0001i
y_6	-0.3053-0.0003i	-0.0264+0.0073i	-0.0029+0.1156i	0.0005-0.0379i
\dot{y}_7	0.0100+0.0316i	0.0244+0.0774i	0.3461-0.0002i	-0.4218-0.0001i
y_7	-0.3556-0.0003i	-0.0241+0.0061i	-0.0024+0.0980i	0.0007-0.0606i
\dot{y}_8	0.0114+0.0360i	0.0177+0.0638i	0.2504-0.0004i	-0.4191+0.0000i
y_8	-0.4058-0.0002i	-0.0198+0.0043i	-0.0017+0.0709i	0.0007-0.0602i
\dot{y}_9	0.0129+0.0405i	0.0092+0.0450i	0.1307-0.0004i	-0.2577+0.0000i
y_9	-0.4558-0.0001i	-0.0139+0.0020i	-0.0008+0.0370i	0.0004-0.0370i
\dot{y}_{10}	0.0143+0.0449i	-0.0002+0.0225i	-0.0014-0.0005i	0.0006+0.0000i
y_{10}	-0.5057	-0.0069-0.0005i	0.0002-0.0004i	-0.0000+0.0001i
$\dot{\phi}$	-0.0000-0.0001i	0.9308	-0.0206+0.0078i	0.0022-0.0001i
ϕ	0.0015+0.0000i	-0.0162+0.2844i	-0.0021-0.0059i	0.0000+0.0003i
$\dot{\psi}$	0.0018+0.0007i	-0.0552+0.0018i	0.0011-0.0005i	-0.0001+0.0000i
ψ	-0.0124+0.0159i	0.0004-0.0169i	0.0001+0.0003i	-0.0000-0.0000i

Details of the classification of each lateral mode is presented as follows:

- a) pendulum mode – the eigenvectors for the velocity and position of the tether nodes are 90° out of phase. The amplitude of the position and velocities increase linearly from the base to the top of the tether. The magnitude of the yaw rotation, ψ of the aerostat is appreciable which suggests that yawing motion is coupled with the pendulum oscillation. This mode has by far the lowest frequency which is expected for the pendulum mode, considering the size of the system.
- b) rolling mode – the dominant motion of this mode is the rolling of the aerostat as large relative amplitudes with the roll angle, ϕ and rotational velocity, $\dot{\phi}$ are observed.
- c) 1st tether harmonic – the eigenvectors for the position and velocity of the tether nodes are 90° out of phase. The magnitude of the position of the tether nodes is a maximum at the middle node which corresponds to a simple concave/convex shape.
- d) 2nd tether harmonic – the position and velocity of the tether nodes are 90° out of phase. The motion for the nodes under node 5 and above node 5 are 180° out of phase. The magnitude of the position of the tether is a maximum at nodes 2 and 7 and is a minimum at node 5 which corresponds to an ‘S’ shaped tether. As expected the frequency of this mode is twice as high as the 1st tether harmonic.

Although, the longitudinal eigenvectors are not explicitly given, their classification followed a similar process. The characteristics and classification of the 4 lowest frequency longitudinal modes is as follows:

- a) pendulum mode – The dominant motion variables for this mode are the position and velocity of the tether nodes in the x-direction, $x_{1...n}$ and $\dot{x}_{1...n}$. The motion in the z-direction is negligible. The eigenvectors corresponding to $x_{1...n}$ and $\dot{x}_{1...n}$ are 90° out of phase. The amplitudes of $x_{1...n}$ and $\dot{x}_{1...n}$ increase linearly from the base to the top of the tether.
- b) pitching mode – the dominant motion of this mode is the pitching of the aerostat as large relative amplitudes of the pitch angle, θ and rotational velocity, $\dot{\theta}$ are observed.
- c) axial spring mode – the dominant motion variables for this mode are the position and velocity in z-direction, $z_{1...n}$ and $\dot{z}_{1...n}$. The magnitudes of the motion variables in the x-direction are negligible.
- d) 1st tether harmonic – Like the pendulum mode, the dominant motion variables for this mode are the position and velocity of the tether nodes in the x-direction and the motion in the z-direction is negligible. The magnitude of the x-position of the tether nodes is a maximum at the middle node which corresponds to a simple concave/convex shape.

3.4.1 Reference Frequencies

The basic motion characteristics from the linear analysis can be compared with the analytical solutions for an ideal tethered aerostat, as a means of checking the validity of

the dynamics model. The analytical reference frequencies for the motion of a buoyant mass on a string are obtained as follows:

for the pendulum mode:

$$\omega_n = \sqrt{\frac{B - mg}{m_e L}}$$

for the axial spring mode:

$$\omega_n = \sqrt{\frac{EA}{m_e L}}$$

for the tether's transverse mode for the n th harmonic [8]:

$$\omega_n = \frac{n\pi}{L} \sqrt{\frac{\rho_t}{A_t(B - mg)}}, \quad n = 1, 2, \dots$$

where m_e is the effective mass of the aerostat including added mass. For the pendulum modes, the relevant added mass included for the longitudinal case is in the x-direction and for the lateral case it is in the y-direction. For the axial spring mode the added mass in the z-direction is included. Added mass is not required for the gravity force used in determining the net lift of the aerostat given as $B - mg$ since the added mass only applies to the inertial properties of the aerostat. The theoretical natural frequencies are used to find the theoretical periods of each mode using $\tau_n = 2\pi / \omega_n$. The results are presented in Table 3.2 for a comparison with the periods given in Figure 3.3 from the linear analysis at $U = 1$ m/s.

Table 3.2: Comparison of theoretical and linear model results for period, τ_n of certain oscillatory modes for baseline case.

	longitudinal pendulum	lateral pendulum	axial spring	1 st tether harmonic	2 nd tether harmonic
theoretical	43.9 s	58.0 s	2.96 s	1.81 s	0.90 s
linear model	44.4 s	67.4 s	2.96 s	1.78 s	0.90 s
% difference	1.14	16.2	≈ 0	1.66	≈ 0

For the fundamental transverse tether mode, the observed frequencies from the linear model were identical for both the longitudinal and lateral cases. Close agreement is observed for all modes with the exception of the lateral pendulum which has a difference of 16.2% with the theoretical value. This discrepancy could be attributed to the fact that the comparison uses the results from the linear model at $U = 1$ m/s while the theoretical period corresponds to a system with $U = 0$. The curve for the period versus wind speed for the lateral pendulum in Figure 3.3 is observed to increase significantly from $U = 1$ to 4 m/s after which it stabilizes near 100 s. It is probable that this trend is also observed in the region from $U = 0$ to 1 m/s which would suggest a period closer to the theoretical value. I believe that the increase in period with wind speed is due to the coupling of the pendulum motion and the yawing of the aerostat. With the additional wind, the aerostat yawing motion intensifies causing the pendulum motion to become more exaggerated, thus increasing the period. The effects of this phenomena appear to become saturated at $U = 4$ m/s. As the wind speed increases to 20 m/s the period eventually starts to shrink suggesting that the wind eventually overcomes this coupling and the lateral pendulum mode behaves closer to the longitudinal pendulum mode which decreases with wind speed. Overall, the good agreement between the linear model and

the theoretical oscillations provides a first level of assurance of the general validity of the dynamics model.

3.4.2 Performance Analysis

Several different physical configurations were studied in an attempt to understand some of the factors that affect the performance of the aerostat on a single tether. The results for the baseline case given by Figure 3.3 are used for a basis of comparison for the current analysis.

3.4.2.1 Leash Length

The first parameter investigated is tether length. The leash length for the multi-tethered aerostat system will likely be shorter than the tether length, $L = 300$ m of the baseline case. Therefore, the behavior of the aerostat with shorter tether lengths of $L = 100$ m and $L = 33.3$ m are presented Figure 3.5 and Figure 3.6 respectively. There are significant differences in the behavior of the system as the tether length decreases. For the longitudinal modes, the pendulum, axial spring and fundamental tether modes all experience a reduction in damping as tether length shortens. Laterally, there is a slight increase to the damping ratio for the pendulum mode but both tether modes are less damped. Minimal changes are observed with the pitching and rolling modes which can be expected since the motion of those modes pertain primarily to the aerostat.

It appears that the reduction in damping ratio for the tether modes (*i.e.* axial spring, tether harmonics) is the result of losing most of the damping influence from the wind. For all modes with the exception of the lateral pendulum mode, the damping increases as U increases. For the baseline case, the damping ratio of the longitudinal

tether modes increase from less than 0.1 to over 0.4 as U increases from 1 to 20 m/s.

The lateral modes are less damped but also experience an improvement as U increases.

For the case with a short tether of $L = 33.3$ m the damping ratios for the tether modes are near the same low values at $U = 1$ m/s, but as U increases only gradual damping improvements are observed. The damping ratio of the longitudinal pendulum mode actually starts to decrease as U approaches its upper limit of 20 m/s. Based on these results it would appear that the system in general is more stable with longer tether lengths. This implies that a long leash length for the multi-tethered system is beneficial. However, it is possible that the high frequency leash modes will be sufficiently damped by the long perimeter tethers. The issue of leash length will be addressed in more detail in Chapter 4 – Experimental System Design.

For the case with $L = 33.3$ m, the slope of the damping curve for the lateral pendulum mode is much flatter in the region from $U = 1$ to 2 m/s as seen in Figure 3.6. This suggests that for this case the pendulum motion is less coupled with the yawing motion at low speeds. To confirm this, it is noted that the theoretical period for an ideal pendulum is 19.3 s while for the lateral pendulum at $U = 1$ m/s the period is 19.9 s. The percent difference between the two periods is 3.1%, which is much better agreement than was obtained in Table 3.2 for the lateral pendulum mode of the baseline case.

3.4.2.2 Attachment Point Location and Pitch Angle

Other important operational decisions that can be addressed with this analysis are the location of the aerostat's attachment point and the aerostat's steady-state pitch angle. The attachment point and pitch angle are related as demonstrated in Chapter 2 by equation (2.9). The z -position of the attachment point was set to $z_l = -11$ m based on a

recommendation from Aeros Flightcam. Also recommended was a steady-state pitch angle in the region of $-5^\circ \leq \theta_0 \leq -10^\circ$. The baseline case was arbitrarily chosen with a slightly less extreme pitch angle of -4° and the x-position of the attachment point, x_l was calculated as 0.764 m. To understand the effects of pitch angle, x_l was modified to give steady state pitch angles of -7° and -1° . The results for these cases are shown in Figure 3.7 and Figure 3.8 respectively. Overall, the results do not change significantly whether $\theta_0 = -1^\circ, -4^\circ$ or -7° . The most notable difference is that the damping ratio for the pitching and rolling modes tends to increase as the pitch angle decreases. Based on this information it appears that there is no advantage to having a steady-state pitch angle in the region of $-5^\circ \leq \theta_0 \leq -10^\circ$. However, there may be a slight advantage in using a zero pitch attitude.

For conventional aerostat applications, a pitched up attitude is beneficial for performance because of the lift generating ability of the aerostat in this configuration. This is an important feature for operation in high winds since the lift to drag ratio must remain high in order to maintain a more vertical orientation of the tether. Typically, aerostats are sized to provide only a slight amount of excess lift beyond the weight of the payload. With a pitched up attitude the aerostat generates lift as the wind increases and the lift to drag ratio remains high.

For our system, the aerostat is designed to provide significant excess lift in order to stiffen the tension structure. Therefore, it is not essential for the aerostat to generate additional aerodynamic lift in order to have stability in high winds (up to 20 m/s). Although additional lift from the aerostat would stiffen the system further, the unsteady nature of the aerodynamic lift force creates serious problems for the positioning accuracy

of the multi-tethered system. This was revealed in related work by Gilardi and Nahon [26] as it was shown that the performance of the streamlined aerostat system is degraded as a direct result of disturbances in the leash tension from lift generated by the aerostat. Unfortunately, this effect occurs irrespective of the steady-state pitch angle, though it is reduced slightly at smaller angles.

3.4.2.3 Model Parameters

The linear model provides a convenient platform for evaluating the performance of the system in response to altering both physical and model properties. To demonstrate this process for investigating the effects of changing a model parameter, the cross-flow drag coefficient of the hull, $(Cd_c)_h$ is reduced. During the modeling process for the Aeros aerostat, there was some uncertainty about the selection of $(Cd_c)_h$. It was decided to use the drag coefficient for a similar sized cylinder, $(Cd_c)_h = 0.8$ from [23], while keeping in mind that this was a rudimentary estimate. In [16], the experimental values for $(Cd_c)_h$ for 6 different aerostats were given. The average of these coefficients was 0.28 which is considerably less than our value. To understand the effect of using a lower value for $(Cd_c)_h$, it was changed in the dynamics model to 0.28 and the modes were plotted as shown in Figure 3.9. The only noticeable difference between these results and the baseline case is a slight increase in damping of the pitching mode. The cross-flow drag coefficient contributes to the lift of the aerostat as seen in equation (2.6). In terms of the pitching mode, the lift generated by the hull is an unstable force since the lift force increases its magnitude when the aerostat pitches up and thereby promotes further pitching motion. Thus, if $(Cd_c)_h$ decreases, it is expected for the pitching mode would

become more stable (higher damping). Since the difference is modest, the drag coefficient of 0.8 will be used until a more suitable estimation technique is found.

The ability to quickly obtain the general performance of the system from the linear analysis is a valuable tool for the operation and design of a tethered aerostat system. Currently, only sparse amounts of information pertaining to the actual operational characteristics of aerostats have been collected. The majority of this information relies on verbal accounts from the aerostat manufacturer, Aeros Flightcam. Since our aerostat requirements are different than most aerostat applications, the results from the linear analysis provide the foundation of our insight towards the operational characteristics of the streamlined aerostat.

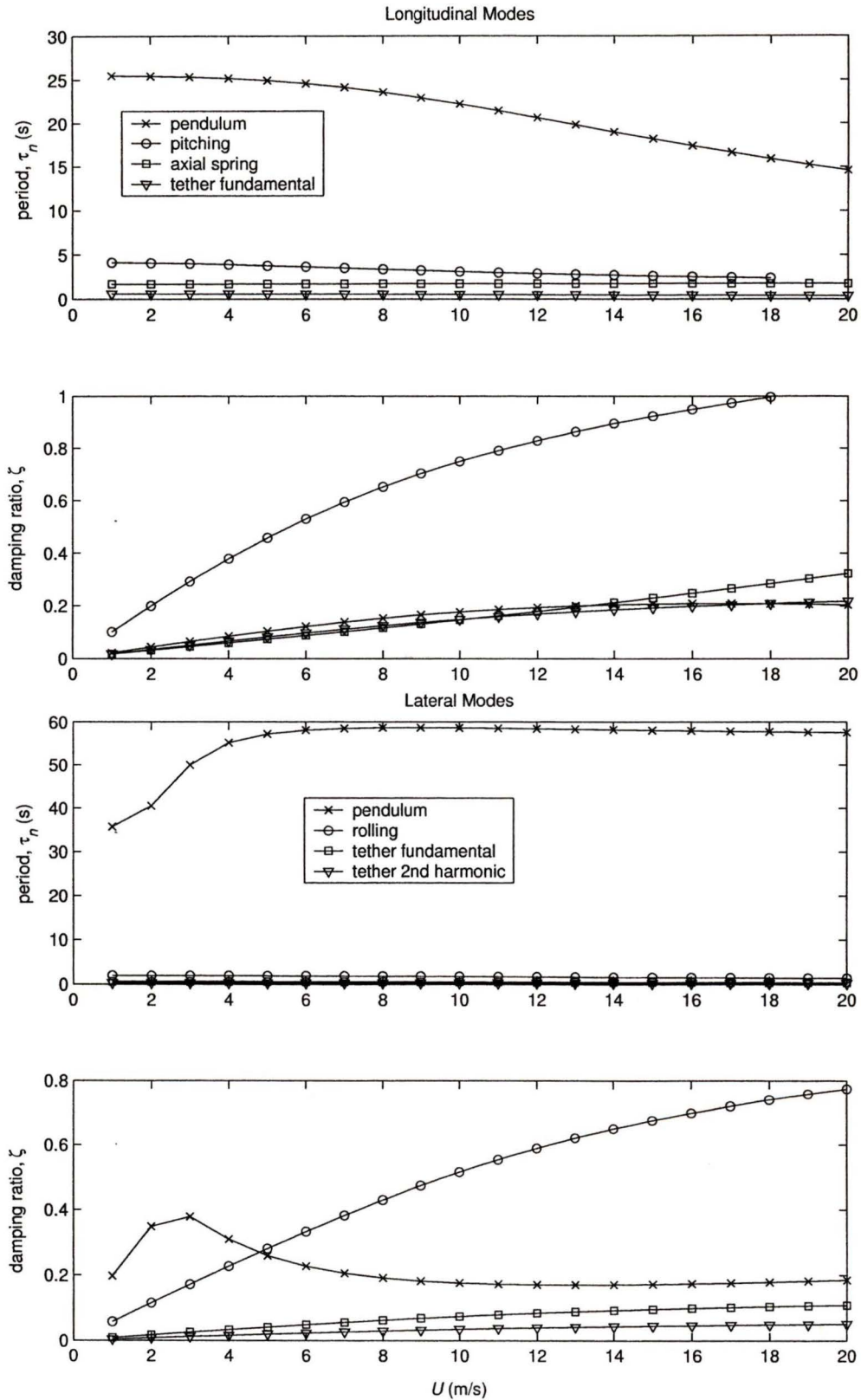


Figure 3.5: Longitudinal and lateral modes for case with $L = 100$ m, $\theta_0 = -4^\circ$.

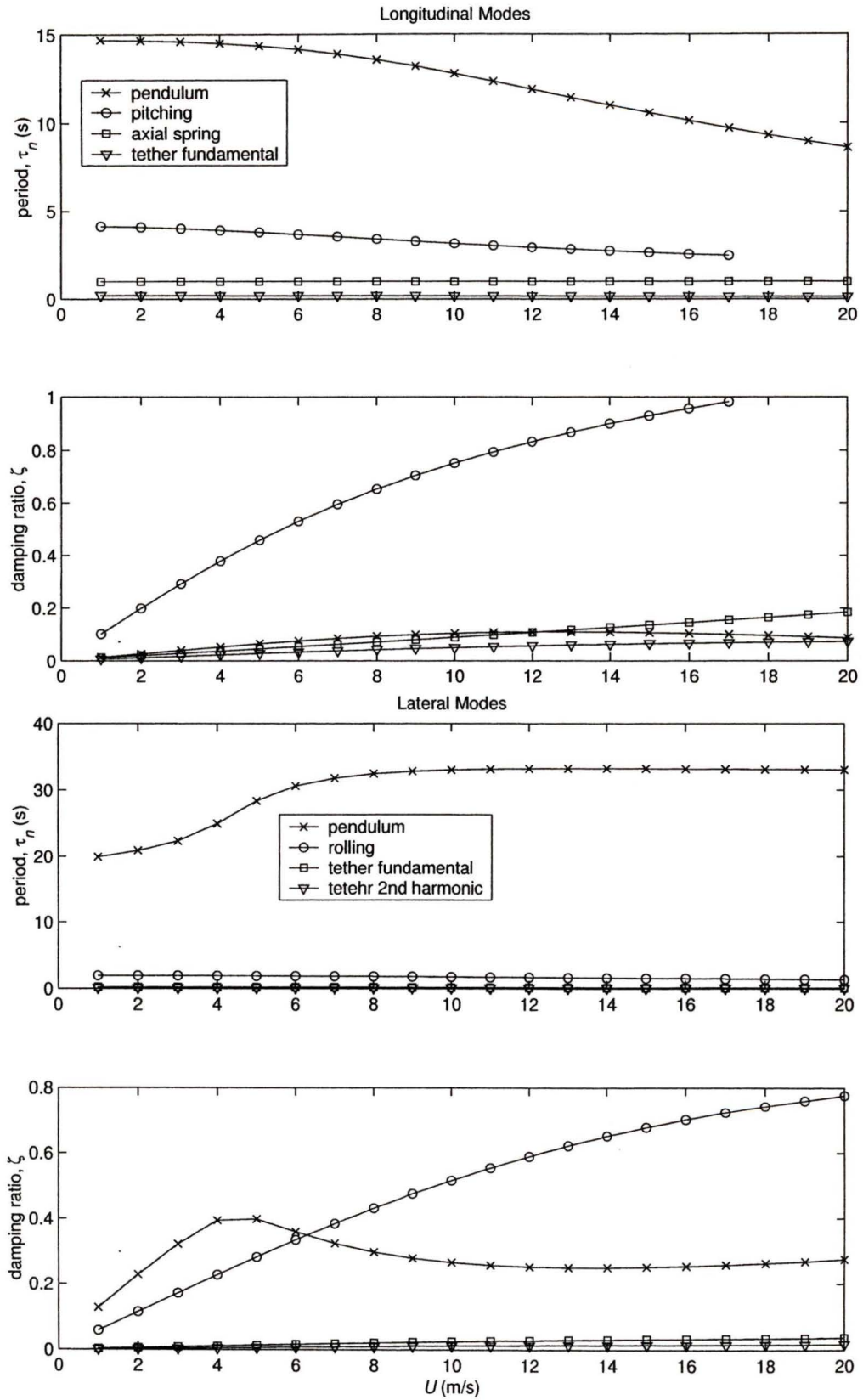


Figure 3.6: Longitudinal and lateral modes for case with $L = 33.3$ m, $\theta_0 = -4^\circ$.

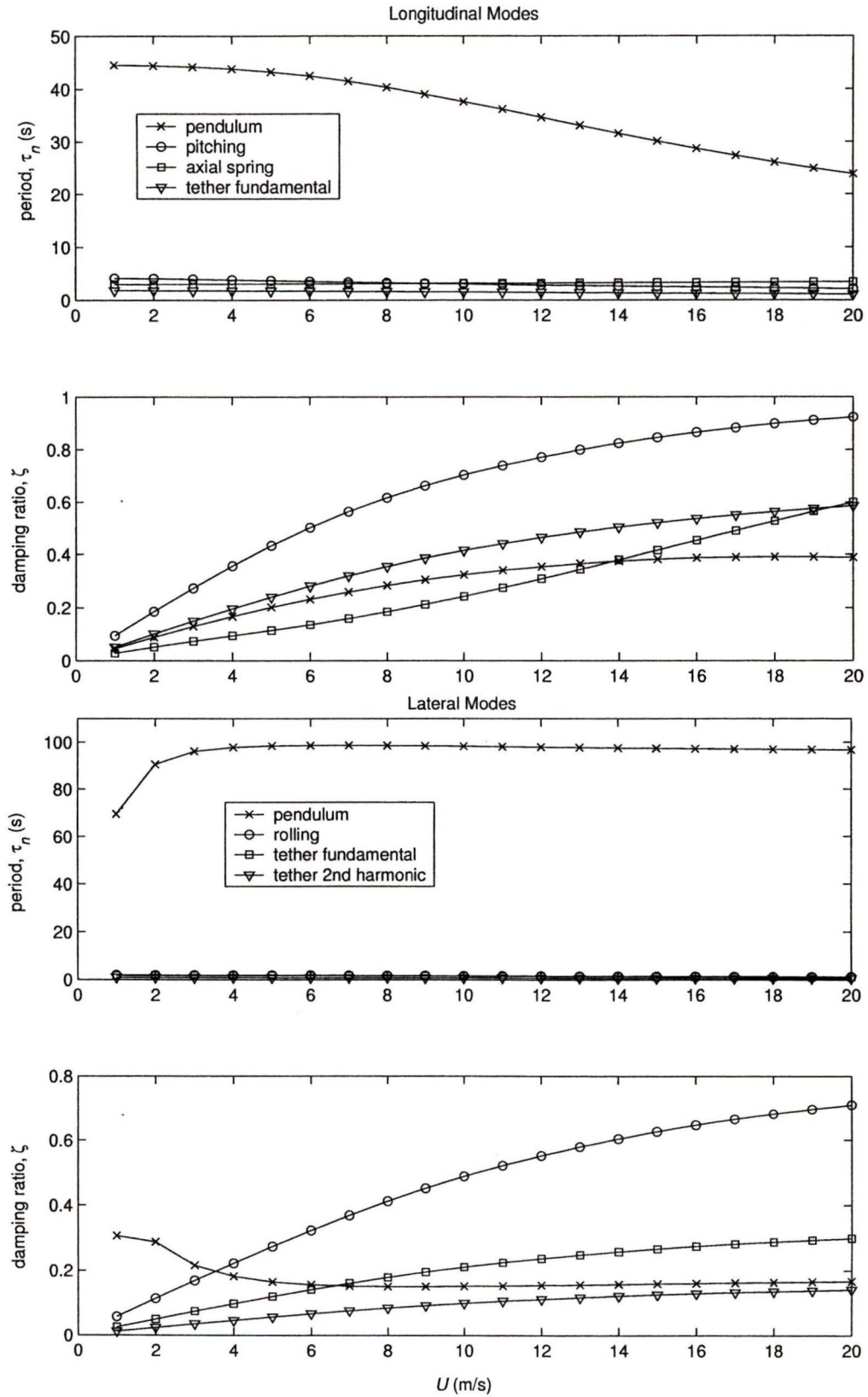


Figure 3.7: Longitudinal and lateral modes for case with $L = 300$ m and $\theta_0 = -7^\circ$.

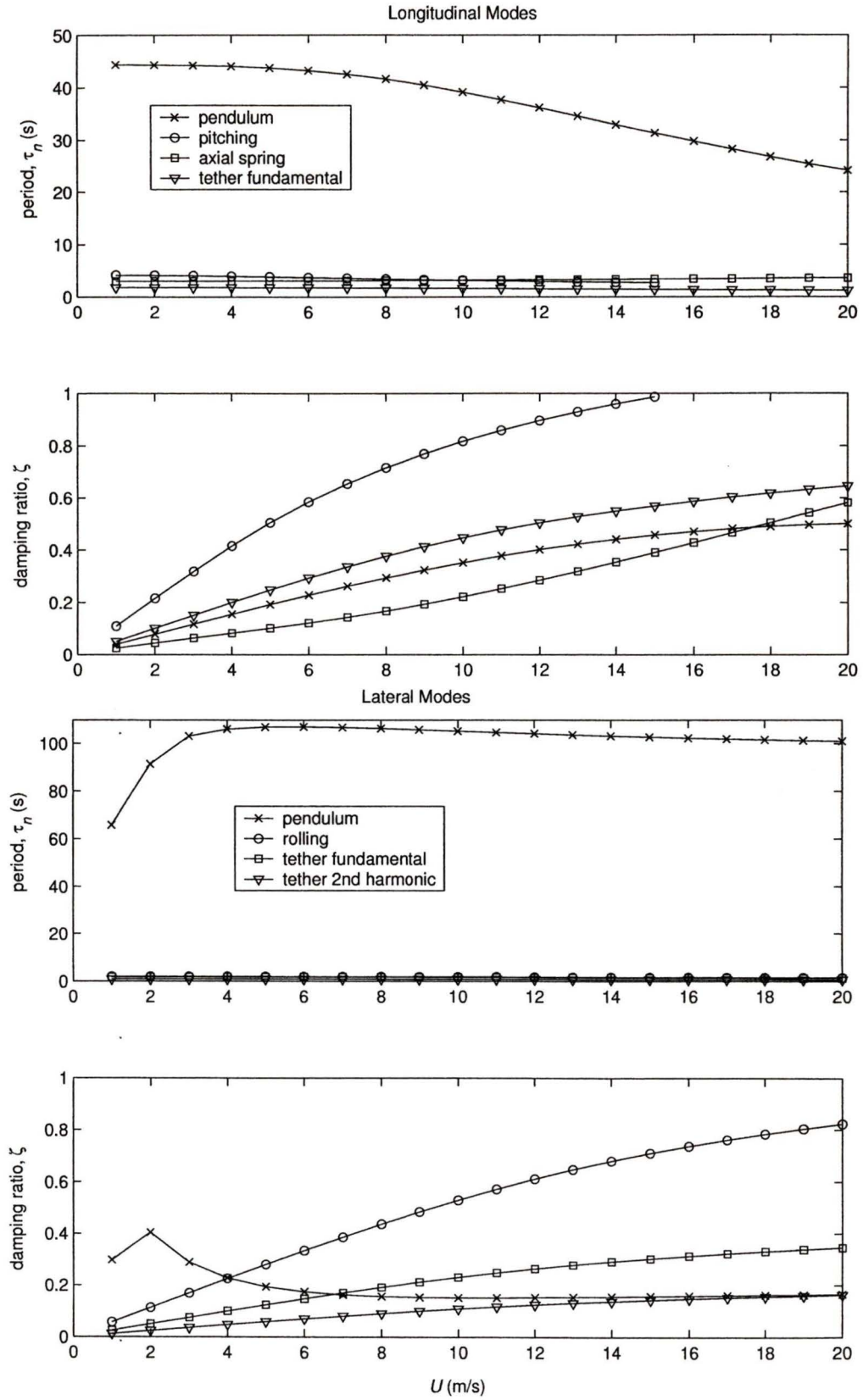


Figure 3.8: Longitudinal and lateral modes for case with $L = 300$ m, $\theta_0 = -1^\circ$.

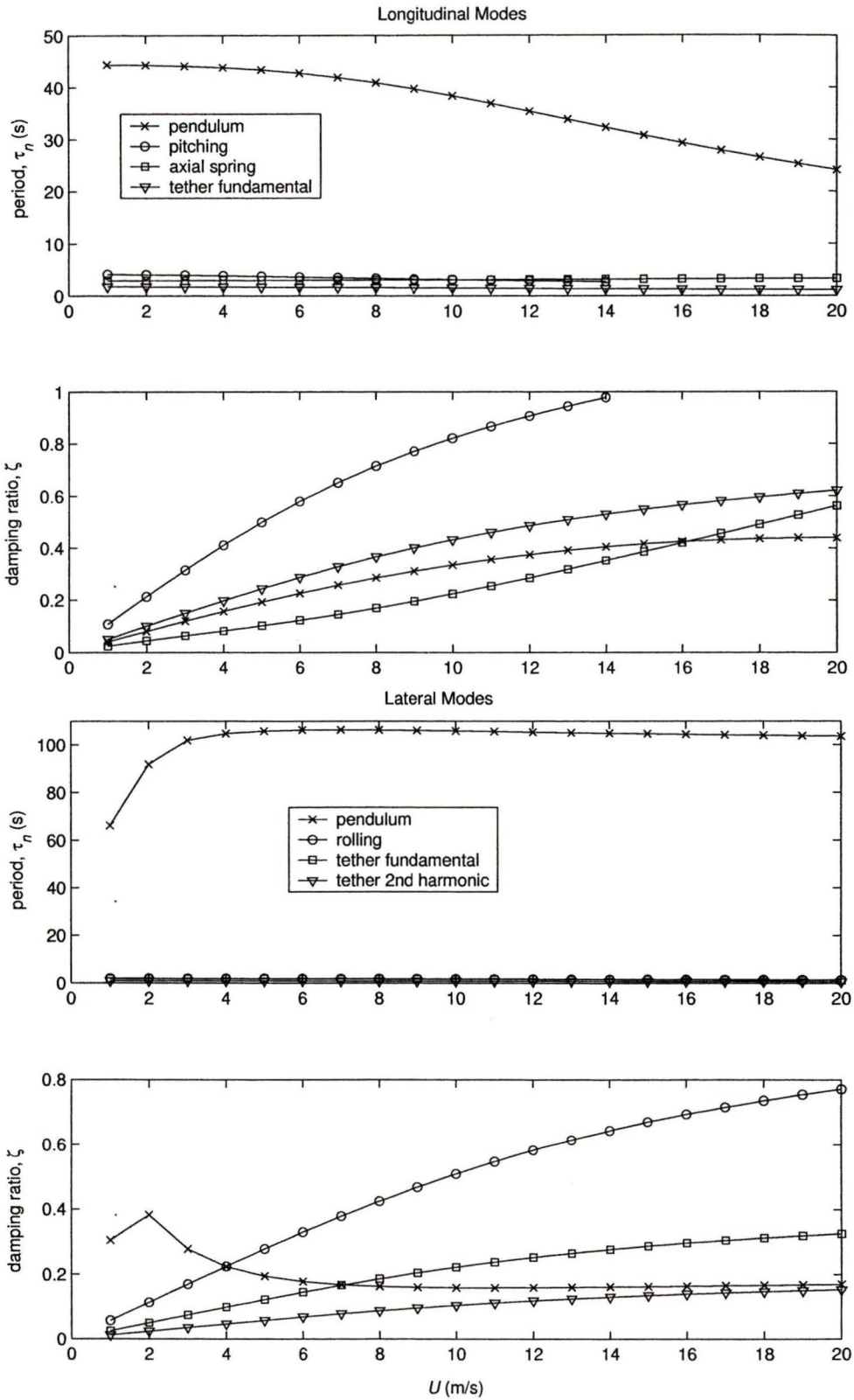


Figure 3.9: Longitudinal and lateral modes for case with $L = 300$ m, $\theta_0 = -4^\circ$ and $(Cd_c)_h = 0.28$.

Chapter 4

Experimental System Design

The design of the scaled tri-tethered aerostat system is presented in two parts. The first, sections 4.1 to 4.3, involves the selection of system components, namely the aerostat, tethers and instrumentation. It should be mentioned that this design process occurred concurrently with the dynamics model development. This initial component selection was based mostly on qualitative analyses of performance and on the original design of the full-scale system which was based purely on a static analysis [9]. The general sizing of the components were taken directly from the scaling results in Chapter 2. Slight modifications were made to certain scaled properties, due to practical considerations. The second part of the system design, section 4.4, focuses on the design of the winching system which relied heavily on results from the dynamics model.

4.1 Aerostat

A basic study of three types of aerostats was conducted to determine which would be most suitable for the scaled experimental system. The types considered were: a) spherical, b) streamlined and c) variable lift (kite).

4.1.1 Aerodynamic Performance

The spherical aerostat, as its name implies, has a spherical shape. This is the simplest type of aerostat as it has no preference to a particular orientation and also does not produce any aerodynamic lift in a horizontal wind profile. The streamlined aerostat has an aerodynamic shape like a teardrop to reduce its wind drag and a number of tail fins for directional stability. A third type of aerostat is termed variable lift reflecting its ability to generate a significant amount of lift in a wind field.

The variable-lift aerostats generate lift through the addition of wings or lifting surfaces, or alternatively by simply using the hull to derive lift. Two different variable lift aerostats, the Skydoc and Helikite were considered. Both are shown in Figure 4.1. The smaller aerostat on top is the Skydoc aerostat. It is an oblate (flattened) spheroid and its mesh flying harness gives it a pitched orientation which exploits its hull to generate lift in a wind field. The lower aerostat is the Helikite and it is a combination of a spheroid aerostat and a kite. It generates lift using its delta wing. The attraction of such aerostats is their ability to maintain a more vertical orientation in high winds. For a conventional aerostat, only the drag increases as the wind speed increases and as a result the aerostat loses altitude as the angle of the aerostat tether becomes less and less vertical.

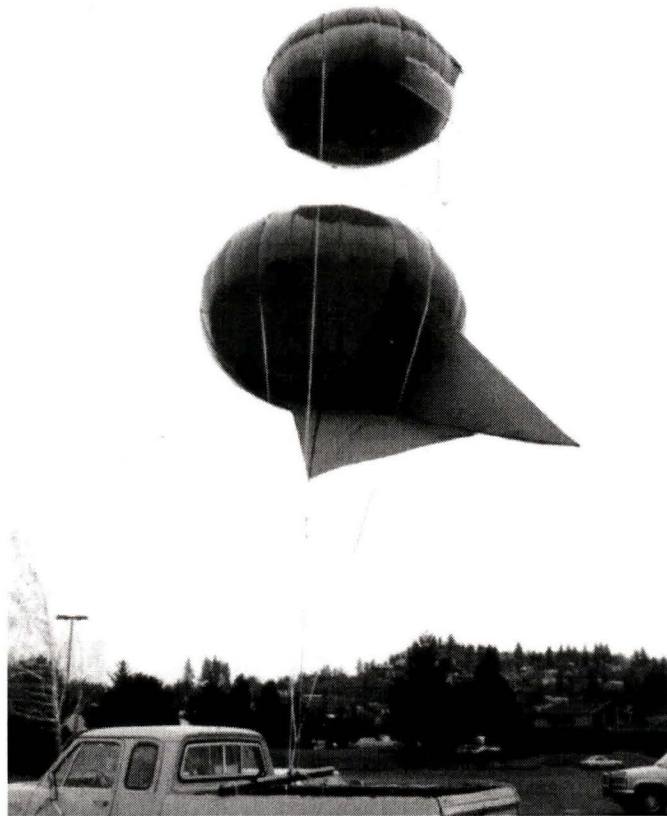


Figure 4.1: Two variable lift aerostats; Skydoc above and Helikite below.

To get an appreciation of the performance of the two variable-lift aerostats, experimental tests were performed while towing the aerostats behind a boat. Figure 4.2 shows the Skydoc being tested. During the tests, poor performance of both aerostats was observed. At high speeds between 40 and 50 km/hr, the aerostats became unstable, and sometimes dove violently all the way to the water surface. Based on these observations it was decided to exclude the variable-lift aerostats from further analysis and instead focus on more conventional spherical and streamlined types.



Figure 4.2: Testing of Skydoc aerostat in Hood River, Oregon, November 2000.

The aerodynamic performance of the spherical aerostat is characterized by a single drag force on the hull which is proportional to its constant spherical cross section and by vortex shedding oscillations. The drag coefficient for spherical bodies is presented in most Fluid Dynamics texts and is shown to vary considerably with Reynold's number, Re [19][23]. To compare the drag coefficient of a spherical and streamlined aerostat, a reference Re of 10^6 was chosen which represents typical operating conditions of the scaled aerostat. The drag coefficient for a spherical body is about 0.15 and for a typical streamlined body it is in the range of 0.03 to 0.1. Including the effect of the hull and the fins, a value of 0.073 (referenced to the frontal area) was used in Chapter 2 for modeling the streamlined aerostat. A value of 0.1 is given from experimental data of a streamlined aerostat in [1]. The difference between the drag coefficients of 0.15 and 0.073 for spherical and streamlined shapes does not completely reflect the actual difference in the

drag force acting on the aerostats. For a given volume of helium, the frontal area of the streamlined aerostat is approximately 1.7 times smaller than the area of a spherical aerostat. This ratio was found based on the dimensions of a sphere containing the same volume as the Aeros aerostat. Therefore, the drag force acting on a streamlined aerostat is about 3.5 times smaller than on an equivalent spherical aerostat. The reduced drag of the streamlined aerostat has two important advantages for the tethered system. First, the disturbances to the tension structure due to wind gusts will have a smaller magnitude resulting in a reduction of the position error. This result was reported in [9] during the original static analysis of the LAR concept. The second advantage is more complicated and an understanding of the design constraints of the original system is required.

Recall that the full system must have the ability to position the aerostat down to the extreme zenith angle, $\theta_{ze} = 60^\circ$ regardless of the wind direction. At $\theta_{ze} = 60^\circ$ the tension in certain tethers decreases to the lowest levels encountered throughout the operating region. When the tension decreases beyond a certain point the tethers sag and are in danger of touching the ground. To demonstrate this, a top view of the tether layout for a particular configuration is shown in Figure 4.3. In this configuration, the tension in tether 1 will be much less than that in the other two tethers. For this case, a reduction in the aerostat drag would increase the tension in tether 1. As a result it will sag less and be less likely to touch the ground creating a more robust system.

The vortex shedding oscillations of a spherical aerostat also suggest that a streamlined aerostat may be preferable for our application as a steadier leash tension is considered desirable. In Chapter 2, the effects of vortex shedding were shown to degrade the performance of the system with a spherical aerostat.

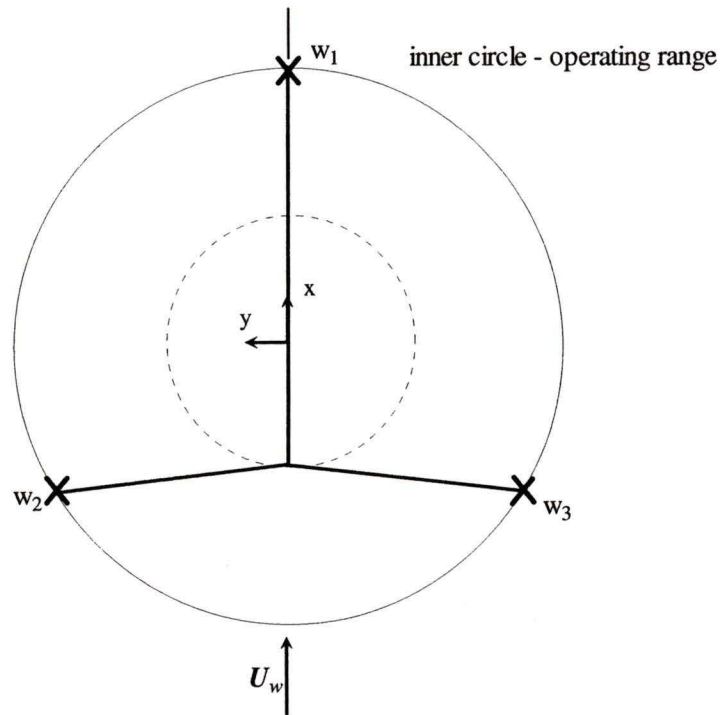


Figure 4.3: Top view of tether layout for configuration with $\theta_{ze} = 60^\circ$, $\theta_{az} = 180^\circ$ and $\theta_w = 0^\circ$.

4.1.2 Survivability

Survivability refers to the aerostat's ability to remain intact and stay afloat in high winds. The mode of failure for an inflatable aerostat is likely to be initiated by the external hull pressure overcoming the internal pressure. This will cause the hull to dimple which is likely to lead to total failure of the aerostat through a rupture in the hull or through the unpredictable behavior of the aerostat when it loses its aerodynamic shape. For a given wind speed the external force on the hull will be less for a streamlined aerostat than for a spherical aerostat since it possesses a smaller drag coefficient. Therefore if similar materials are used for both aerostats, the streamlined aerostat should have a higher wind speed threshold than its spherical counterpart.

4.1.3 Cost and Availability

The cost and availability of commercial aerostats is an important factor for the selection of a suitable aerostat for our system. The commercial manufacturers of aerostats seem to be split into two distinct groups. The first produces small, basic and inexpensive aerostats that are usually used for advertising purposes. The second group produces large, sophisticated and expensive aerostats used for lifting heavy loads. The advertising aerostats are available in all shapes and sizes, while for the larger aerostats, it appears that only streamlined shapes are commercially available. The required net buoyancy for our scaled system is considerably higher than the limited buoyancy of the advertising units which implies that a manufacturer of large aerostats is more suitable for the fabrication of our aerostat. There are only a few large aerostat manufacturers in the world. Of the aerostats from these companies, most serve defense applications and tend to be more expensive than could be afforded for this project. Aeros Flightcam is a relatively new aerostat manufacturer and produces aerostats for flight surveillance at a reasonable price. All their previous aerostats have a streamlined shape, though they are capable of producing a spherical aerostat on request. The simplicity of the spherical aerostat would reduce the cost since additional components such as the tail fins are not required. However, the disadvantage of the spherical aerostat is that it is a less common design in large sizes and would therefore be subject to uncertainty with design, fabrication and operation.

4.1.4 Ground Handling

Ground handling and mooring of aerostats are among the most difficult problems encountered during the operation of tethered aerostats [15]. The support system for handling the aerostat once it is near or on the ground is often more complex and costly than the aerostat itself. The two aerostat options considered have different requirements for ground handling that must be considered.

For the spherical aerostat, the ground handling equipment will undoubtedly be simpler than for the streamlined aerostat since it does not need the ability to weathervane. Therefore once the aerostat is near the ground, the forces generated on the aerostat are the same drag forces experienced while in flight and the orientation of the aerostat is not a concern. This suggests that a relatively simple strategy to secure the aerostat would be possible. Conversely, for the streamlined aerostat, more complicated ground handling equipment is required to accommodate its tendency to weathervane. The aerodynamic drag of the streamlined aerostat is relatively small in direct headwinds, but in a side wind the drag increases significantly. If the aerostat is rigidly secured and unable to freely rotate, the loading from even mild side winds is strong enough to generate very large forces. This implies that the mooring station for a streamlined aerostat must either permit the aerostat to rotate freely into the wind or the aerostat must be completely sheltered from the wind. If an enclosed shelter is used, additional equipment is required to transport the aerostat from the shelter to the launch site. Both options for mooring the streamlined aerostat are likely to cost much more to build and operate than a simpler mooring station for a spherical aerostat. Consequently, the available resources for ground handling equipment become a critical factor when selecting which aerostat is more suitable for a

particular application. For our experimental system, sufficient funding and infrastructure was available for the ground handling equipment for either the spherical or streamlined aerostat.

4.1.5 Aerostat Selection

The decision was made to use a streamlined aerostat for the scaled experimental system. The streamlined aerostat demonstrates better performance from a static perspective [9] and is likely to have a higher survivable wind speed than a spherical aerostat. It is acknowledged that the ground handling equipment and procedures are more complicated than for a spherical aerostat, but in the interest of better performance of the positioning system, it was decided to accept the added ground handling complexities. It should be noted that the final decision to use a streamlined aerostat was made before the dynamics model was fully developed and more thorough investigations were conducted. A preliminary analysis of the performance of the full-scale streamlined aerostat system later revealed that the fluctuating lift generated by the gusts may cause significant problems. If this does turn out to be the case, the spherical aerostat may become a better option [26].

4.2 Tether Selection

From the scaling analysis in Chapter 2, certain properties were defined for the tethers based on the properties of the full scale system. The scaled tether properties are reiterated in Table 4.1.

Table 4.1: Desired scaled tether properties from Chapter 2.

diameter, D_t	6.17 mm
density, ρ_t	840 kg/m ³
elastic modulus, E	5.6 GPa

4.2.1 Tether Materials

Initially, an attempt was made to find an existing commercial tether with these properties. A list of high strength commercial tether materials is provided in Table 4.2. The properties given are for a braided tether and differ from the constituent material properties. The tether used in the design of the full scale system was *Spectra*. From the tethers listed, it is not possible to match both the density and elasticity required for the scaled tether. A more exhaustive search of tether materials was not undertaken since it was understood that only a light, high-strength tether would be suitable for the tethered aerostat system.

After some further analysis, it was decided that it was more important to choose the best performing tether material, rather than trying to choose the tether with the closest match to the scaled properties in Table 4.1. The rationale for this decision was based on the premise that the optimizing the capability of the scaled system was more important than designing a strictly similar model. It is also noted that the validation of the simulation can be accomplished irrespective of which tether is used.

Table 4.2: Properties for braided tethers of several materials [4][9].

tether material	density, ρ_t (kg/m ³)	break strength, S_b (GPa)	elastic modulus, E (GPa)	S_b/ρ_t (m ² /s ²)
Kevlar 49	1000	0.86	11	8.6e5
Spectra	840	0.98	17	1.2e6
Plasma	840	1.16	38	1.4e6
Vectran	1050	1.09	28	1.0e6
Steel	4400	0.71	80	1.6e5

The best performing tether material was chosen by considering two important factors: the strength to weight ratio, S_b/ρ_t and the stiffness. The tether's stiffness is characterized by the elastic modulus, E . The strength to weight ratio is a direct indicator the weight of the required tethers. It is clear that lighter tethers are favorable for our system since this would reduce the lift required from the aerostat. From Table 4.2 it is observed that *Plasma* has the highest strength to weight ratio and also is the stiffest (highest E). Therefore, it was chosen as the tether material for the scaled system. It is noted that the original tether selection of *Spectra* for the full scale system occurred before *Plasma* and *Vectran* were available on the market. It is likely that *Plasma* or *Vectran* would be chosen for the full scale system as well.

4.2.2 Tether Size

The diameter of the tether was chosen as $D_t = 6$ mm which is close to the scaled value of $D_t = 6.17$ mm. Before this size was finalized, the maximum expected load was compared with the breaking strength to determine the factor of safety. The breaking strength of the 6 mm tether is 35.6 kN. The minimum safety factor for use with new tethers

recommended by the manufacturer is 3:1 [29], but for our application where the tethers are subject to extended use outdoors, a minimum safety factor of 5 was deemed necessary. To determine the actual safety factor for the 6 mm tether, the maximum tension was estimated from the dynamics model. During operation, the maximum tension in the tethers increases as the zenith angle increases from 0 to 60°. The original system was designed to be operational for wind speeds up to 10 m/s plus turbulent gusts. This scales to a corresponding wind speed of $U = 5.77$ m/s for the scaled system. Therefore, the maximum operational wind speed planned for the scaled system is $U = 6$ m/s. The maximum tension observed during the operation of the system is 6.46 kN which occurs when $\theta_{ze} = \theta_{az} = 60^\circ$ and $\theta_w = 120^\circ$. Therefore, the safety factor during operation is $35.6 \text{ kN} / 6.46 \text{ kN} = 5.5$ which is acceptable.

For occasions when the wind speed exceeds the operational limit, the system will be returned to the symmetrical configuration ($\theta_{ze} = \theta_{az} = 0^\circ$) where the maximum tether tension is observed to be the lowest. From wind speed data recorded at the Penticton airport from Environment Canada, during the period from 1940 to 2000 during the months excluding December and January the wind speed exceed 19.4 m/s only 11 times. For that same period the wind speed never exceeded 22.2 m/s. Higher wind speeds were recorded in December and January, so it is recommended that during these months in particular, aerostat testing only take place during calm periods. The maximum wind speed expected for the aerostat was determined to be 20 m/s. For the case with the system in the symmetrical configuration with a wind speed, $U = 20$ m/s, the maximum tether tension is 7.02 kN. This yields a safety factor of 5.1 which is just above the imposed safety factor limitation. It should also be noted that at wind speeds of 20 m/s, the

survivability of the aerostat itself is questionable. It is recommended that constant attention be given to weather forecasts for the region during testing of the aerostat system to ensure that aerostat is retrieved to a safe location during hazardous weather.

4.2.3 Tether Length and Layout

The dimensions for the length and layout of the perimeter tethers were taken directly from the scaled results given in Table 2.4. The length of the leash however was not directly chosen to correspond with the original leash length for the full system of 100 m, since during the design of the original system this length was chosen arbitrarily. To investigate the effects of using various different leash lengths for the scaled system, the simulation was run for three different lengths of 11.1 m, 33.3 m and 100 m. The results are given in Figure 4.4 for the passive system in the standard symmetrical configuration with turbulence effects included. The response for the tether tension and the error out of the focal plane are relatively similar, but the error in the focal plane differs considerably over the range of leash lengths. The in-focal plane error is greatest for the shortest leash length of 11.1 m and decreases as the leash length increases. It is also interesting to note that there is a significant time shift in the responses, demonstrating that the system responds more slowly to disturbances with the longer leash. Based on these results, it is concluded that longer leash lengths will lead to better performance of the system. There is likely an upper limit to what leash length is manageable with the aerostat launching equipment and procedures, but it is unknown at this time what this limit will be. It is planned to start by testing a 33.3 m leash and then progress to longer leash lengths once the launch and recovery equipment and procedures are established.

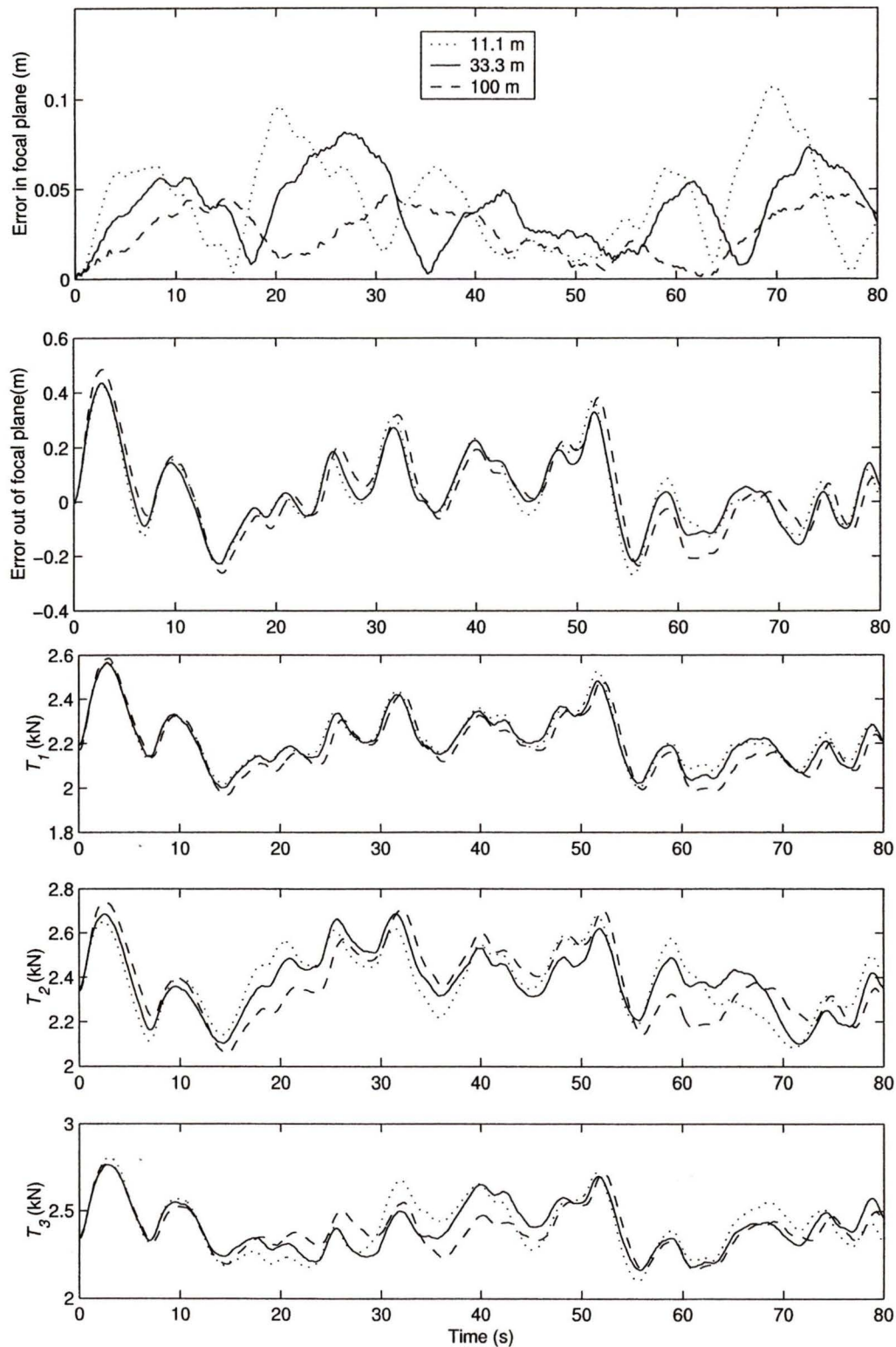


Figure 4.4: Simulation results for payload error and tether tension for three different leash lengths with $U = 6$ m/s in symmetrical configuration (i.e. $\theta_{ze} = \theta_{az} = \theta_w = 0^\circ$).

4.3 Instrument Platform

The instrument platform is located near the confluence point of the tri-tethered structure. It is a circular plate designed to hang freely on all three tethers using hanger fittings placed on the edge of the plate. The top of the instrument platform is shown in Figure 4.5. Because the tether hanger fittings and the actual tether termination points on the ground are arranged in similar equilateral triangles, this ensures that as the system moves to a different configuration and the various tethers change length and orientation, the platform itself remains horizontal. This occurs since any horizontal slice through the three tethers will always be an equilateral triangle and, in the absence of friction, the tether hangers will slide on the tethers until the plate is level.

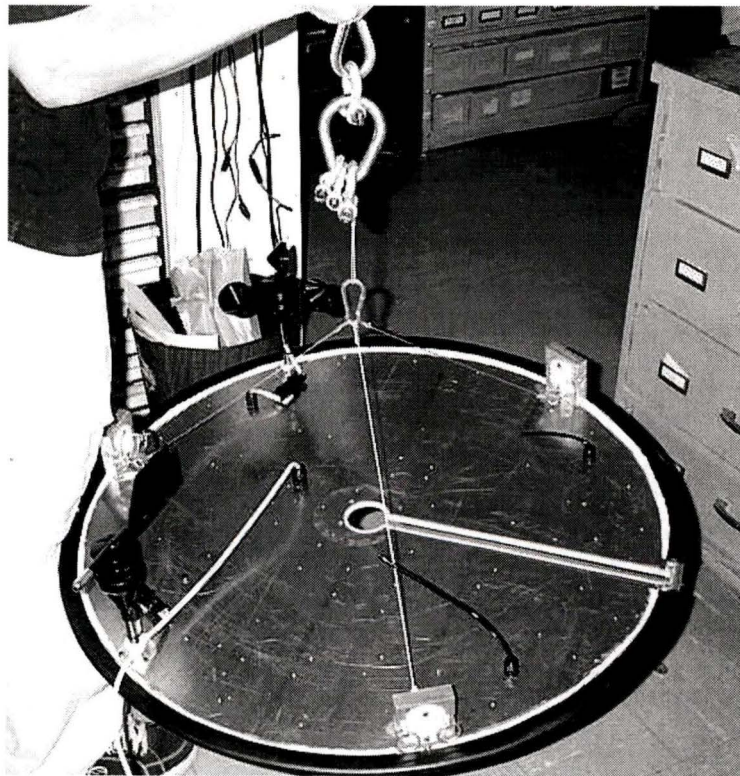


Figure 4.5: Top view of instrument platform with tether hanger fittings, wind speed and wind direction sensors.

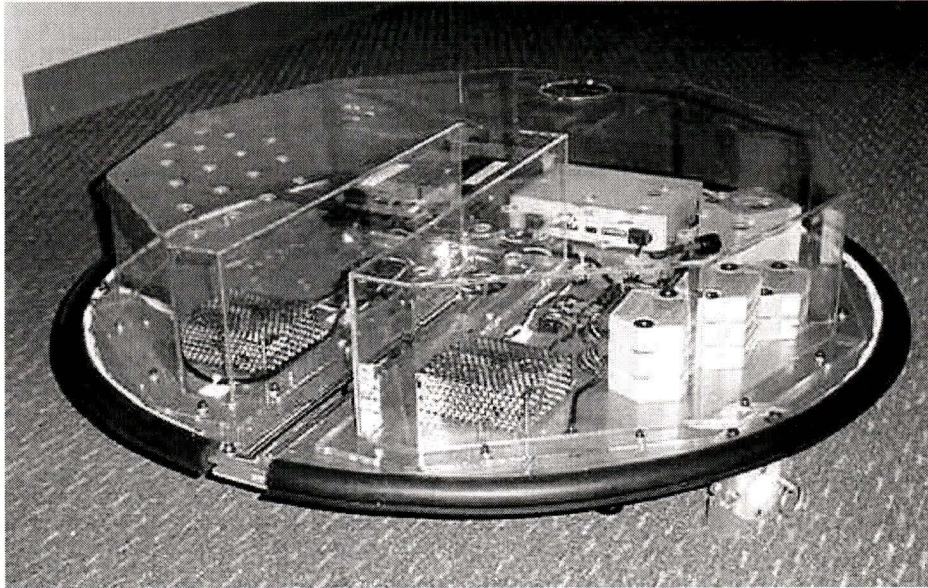


Figure 4.6: Underside of instrument platform.

The onboard sensors are used to collect experimental data that can be used to compare to the simulation results. Therefore, the sensors must accurately measure the environmental conditions as well as the response to the various components of the system. The underside of the platform with its protective cover is shown in Figure 4.6.

The complement of onboard instruments and their functions are summarized as follows:

- 4 load cells – used to measure the tension in the three perimeter tethers and the leash,
- wind sensors – separate sensors to measure the wind speed and wind direction,
- 2-axis tilt sensor – used to measure the tilt of the platform,
- digital compass – measures the heading of the platform,
- differential GPS system – GPS antenna and receiver used to measure the position of the platform; a similar unit on the ground completes the differential system,
- temperature probe – measures air temperature,

- 2 radio modems – transmit data signals to ground computer; one unit for the GPS data and another for all the remaining sensor data.

All the sensors have analog outputs which are converted into digital RS-485 signals using analog to digital converter modules located on the platform. The RS-485 signals are then converted to RS-232 prior to transmission via the radio modem.

4.4 Winch Design

The conceptual design process for the tether winching system for the scaled aerostat system begins with the determination of the required tether motion and tension predicted by the dynamics model. Once these are established, the mechanical components are selected in order to provide these capabilities. The winch system is made up of the four main components: an electric motor, a gearing system, a drum and a frame. The motor drives the drum through the gearing and the frame provides the structure that houses the rest of the components and provides a base for the rotation of the drum. One end of the tether is attached to the drum, so as the drum rotates the tether length changes. The conceptual design of the winching system follows the approach that the system should consist of off the shelf parts wherever possible.

4.4.1 Tether Motion and Tension

The required tether motion and tension for active control of the confluence point can be determined using the dynamics model of the aerostat system with actively controlled tethers. The procedure for determining the winch requirements is summarized as follows:

- numerous combinations of azimuth angle, zenith angle and wind direction were investigated to determine a worst case configuration,
- control gains were chosen to stay within a pre-set maximum power limit,
- results for the tether tension, speed and acceleration are obtained, for the worst case with the chosen control gains.

4.4.1.1 System Configuration

There is a wide range of operating conditions for the tethered aerostat system and it is observed that the behavior of the system varies markedly over this range. The change in behavior is a result of the change in physical layout of the system. As the payload is positioned throughout the operating range, the tether lengths and slopes can vary by as much as a factor of two, thus significantly altering the dynamics of the system. Therefore it is essential to investigate the whole range of operating configurations prior to determining the motion requirements of the winch system. The operating conditions are defined as $0 \leq \theta_{ze} \leq 60^\circ$, $0 \leq \theta_{az} \leq 360^\circ$, $0 \leq \theta_w \leq 360^\circ$ and $0 \leq U \leq 6 \text{ m/s}$. To get an appreciation for which configurations are the most demanding for the winch to control, numerous simulation trials were performed with constant PID gains.

Due to the symmetry of the system, it was only necessary to consider configurations with an azimuth angle, θ_{az} in the range of 0 to 60° , shown as the shaded region in Figure 4.7. It was found that the positioning performance of the system degrades as the zenith angle and wind speed increase. This trend results in the worst performance being observed at the outer boundary of the operating range where the zenith angle is 60° and the wind speed is 6 m/s. The degradation in performance is a

result of an increase in tension in one or more of the tethers. The rise in tension from additional wind loading is easily understood, but the tension increase due to an increasing zenith angle is more complex. To understand why the tension increases with zenith angle, the angle between tether and the applied load must be considered. As the angle between the load on the tether and the tether axis becomes greater, the tension will increase. When the zenith angle increases the tether slope of at least one tether becomes shallower and since the applied load is vertical, the tension in that tether increases. With an increase in tension, the winch has to work harder to control that tether and the performance deteriorates.

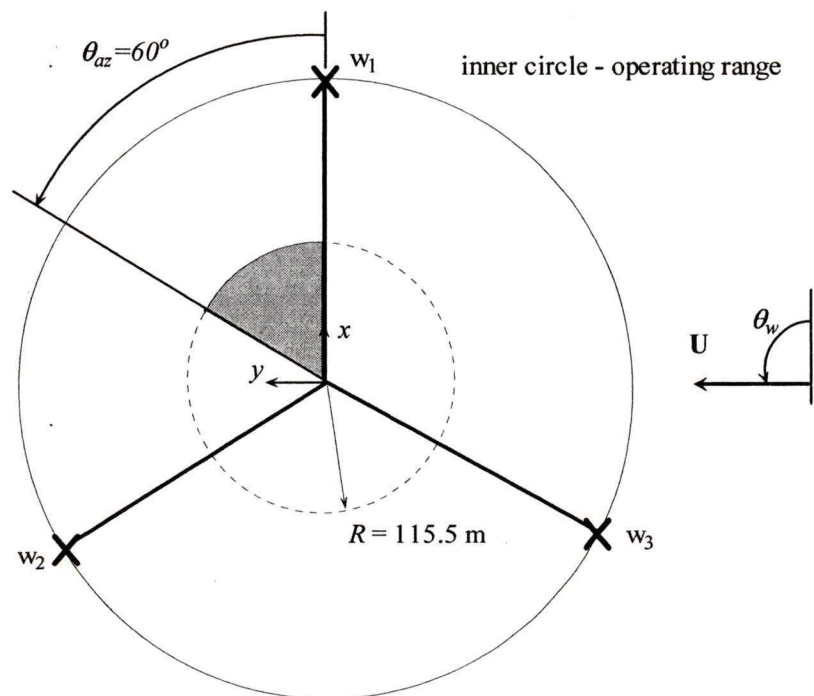


Figure 4.7: Top view of LAR layout; shaded portion of operating range represents region of study.

The two quantities that characterize the performance of the system are the maximum error of the payload, e_{max} , and the maximum power required at one of the winches, P_{max} , over the duration of a particular simulation. These quantities are defined as:

$$e_{max} = \max \|\mathbf{p} - \mathbf{p}_d\|, \quad P_{max} = \max |T_j \cdot \dot{L}_j|$$

where T_j is the tension at the winch of each tether. Table 4.3 presents results for e_{max} and P_{max} at incremental configurations over the full range of operating conditions. The dark shaded regions represent the cases with the maximum power while the lighter shaded regions represent the cases with the largest error.

Table 4.3: Maximum error, e_{max} (cm) / max power, P_{max} (kW) for cases with $\theta_{ze} = 60^\circ$ during 80 s simulation with $k_p = 5$, $k_i = 1.73$, $k_d = 1.73$ and $U = 6$ m/s.

θ_w	θ_{az}				
	0	15	30	45	60
0	0.16 / 0.93	0.16 / 1.25	0.17 / 1.23	0.17 / 1.32	0.19 / 1.23
30	0.16 / 0.89	0.16 / 1.22	0.17 / 1.35	0.17 / 1.42	0.18 / 1.22
60	0.16 / 0.96	0.16 / 1.01	0.17 / 1.16	0.18 / 1.41	0.18 / 1.37
90	0.14 / 1.20	0.16 / 1.00	0.17 / 1.18	0.17 / 1.20	0.18 / 1.27
120	0.11 / 0.96	0.11 / 0.98	0.15 / 1.56	0.18 / 1.24	0.19 / 1.28
150	0.11 / 0.98	0.15 / 1.06	0.12 / 1.22	0.12 / 1.28	0.16 / 1.60
180	0.11 / 0.97	0.11 / 1.08	0.12 / 1.26	0.12 / 1.28	0.12 / 1.25
210	0.11 / 0.98	0.11 / 1.12	0.11 / 1.28	0.12 / 1.31	0.12 / 1.28
240	0.11 / 0.90	0.11 / 1.14	0.12 / 1.27	0.12 / 1.31	0.12 / 1.27
270	0.14 / 1.20	0.11 / 1.14	0.12 / 1.29	0.12 / 1.35	0.12 / 1.29
300	0.16 / 0.92	0.17 / 1.13	0.15 / 1.60	0.12 / 1.32	0.13 / 1.26
330	0.16 / 0.88	0.16 / 1.12	0.17 / 1.24	0.18 / 1.33	0.16 / 1.59

From the perspective of the winch design, the worst case configurations are those with the highest power requirements since that will determine the motor capabilities needed. Thus, the winches will be designed for the cases with $\theta_{az} = 30$, $\theta_w = 300^\circ$ and $\theta_{az} = 60$, $\theta_w = 150^\circ$ on the assumption that they will then have the required power for the entire operating range.

4.4.1.2 PID Gains

It is necessary to find new controller gains for specific maximum power levels that pertain to practical power limits. The maximum electrical power available at the site in Penticton will either be 2 kW or 4 kW per winch (depending on whether 6 or 3 winches are being used). Assuming that the efficiency of the motor and winch is about 75%, the maximum winch output power will be 1.5 kW or 3 kW. PID gains were found by trial and error that provide output power up to these limits for the two worst case configurations in Table 4.3. The results are summarized in Table 4.4. It is noted that the position accuracy of the system improves considerably as the available power level is increased from 1.5 to 3 kW.

Table 4.4: PID gains for worst case configurations for maximum power levels of 1.5 kW and 3 kW.

θ_{ze} (deg)	θ_{az} (deg)	θ_w (deg)	U_w (m/s)	k_p -	k_i (1/s)	k_d (s)	e_{max} (cm)	P_{max} (kW)	P_{rms} (kW)
60	30	300	6	5	1.5	1.5	0.16	1.49	0.40
60	60	150	6	5	1.5	1.5	0.17	1.49	0.40
60	30	300	6	13.5	3	4	0.07	2.96	0.61
60	60	150	6	13.5	3	4	0.08	2.96	0.60

4.4.1.3 Winch Requirements

The tether motion and tension are the simulation's output variables that determine the requirements for the winch. For the sake of brevity, only the results for configuration of $\theta_{az} = 60^\circ$ and $\theta_w = 150^\circ$, which will be termed case 1, are considered from this point on. The results are summarized for this case at both power levels in Table 4.5 and Figure 4.8. The 'max' values in Table 4.5 are the maximum values observed over all three tethers and the 'rms' values represents the rms value for that tether over the 80 s time history. Figure 4.8 shows the simulated time history of the results for tether 1 for which the largest power levels were observed. Both the max and rms values are significant when applied to the winch design because motors are typically characterized by two ratings: the peak rating which it can only sustain for short periods of time, and the continuous rating which represents its sustainable performance.

Table 4.5: Winch performance parameters for case 1 with maximum power levels of 1.5 kW and 3.0 kW.

P_{max} (kW)	P_{rms} (kW)	v_{max} (m/s)	v_{rms} (m/s)	a_{max} (m/s ²)	a_{rms} (m/s ²)	T_{max} (kN)	T_{rms} (kN)
1.49	0.4	0.24	0.074	6.3	0.92	6.14	5.4
2.96	0.61	0.48	0.110	17.1	2.9	6.14	5.4

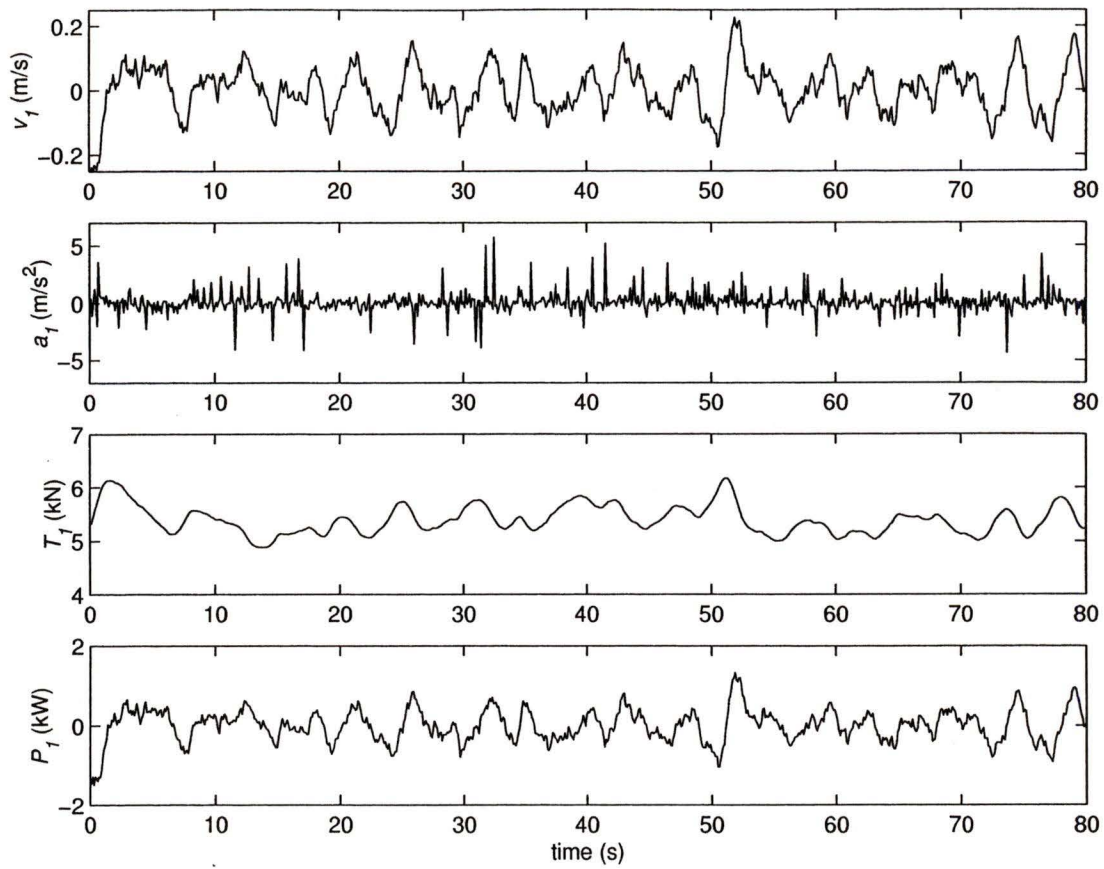


Figure 4.8: Tether speed, acceleration, tension and winch power for tether 1 with $P_{max} = 1.5$ kW, $\theta_{az} = \theta_{ze} = 60^\circ$, $\theta_w = 150^\circ$, $k_p = 5$, $k_i = 1.5$, $k_d = 1.5$ and $U_w = 6$ m/s.

It is interesting to note that the tether tension does not change appreciably between the cases for the two different power levels. This implies that the increase in power is attributable solely to an increase in tether velocity. Also worth noting is that although the maximum values for the power doubled, the rms power levels only increased by a factor of about 1.5.

4.4.2 Drive Components

The velocity, acceleration and tension for tether 1 established above for case 1 will be the basis for the winch design. The overall process for the conceptual design of the winch drive system is summarized as:

- determine standard winch drum characteristics,
- determine drum output for speed, acceleration and torque,
- select motors and gearing system to meet specifications,
- select auxiliary components and communication system for operation of motor.

4.4.2.1 Winch Drum

A standard winch drum consists of a cylindrical core with flanges on its outer edge. The tether wraps around the core and is contained by the flanges on its end. A schematic of a winch drum is shown in Figure 4.9. The amount of tether on the drum at any particular time affects the location of the tether load which in turn affects the torque load on the drum and the speed at which the drum must rotate. Therefore it is essential to estimate both the actual dimensions of the drum and the amount of tether that is wrapped on the drum prior to determining the winch torque and speed requirements.

The design considerations for sizing the drum are based on performance and on practical size limits. The performance measures are the torque and speed required for the drum and these should be minimized.

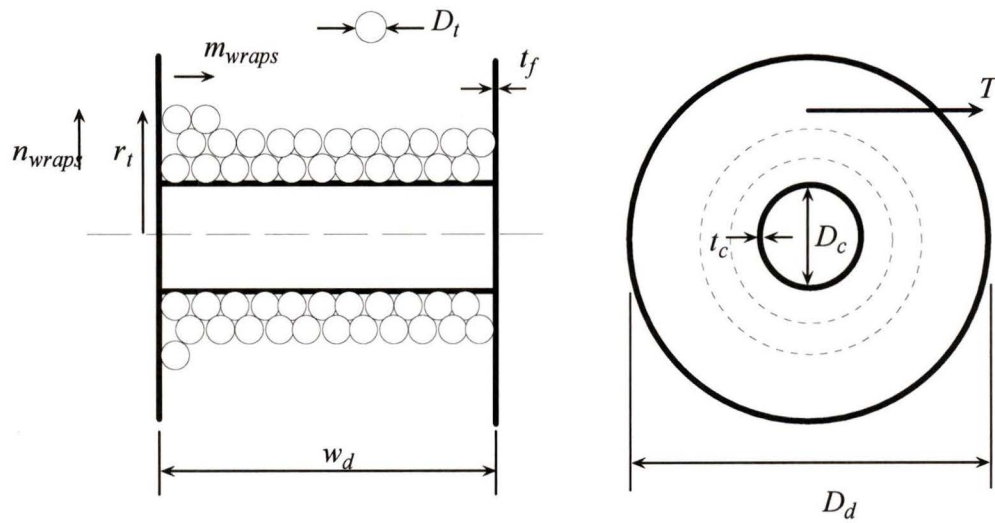


Figure 4.9: Front and side view of winch drum with tether wraps.

To minimize the required torque, the moment of inertia of the drum about its rotational axis, J_d and the moment arm, r_t for the applied tether load, T must be minimized. With this goal in mind, the drum core diameter, D_c should be as small as possible and the drum width, w_d should be as large as possible. However to minimize the required speed of the drum, it is desirable to maximize r_t since the tether speed is equal to the drum rotation speed multiplied by r_t . Therefore, the drum width should be as small as possible to ensure a slower speed. To gain a better understanding of the opposing requirements for the drum width, the motor requirements for two standard drum widths will be compared. In terms of practical size considerations, the diameter of the drum core is limited by the minimum bend radius of the tether as recommended by its manufacturer while the drum width is limited by the practical size limit of the overall winch. The nominal dimensions for two standard drums (widths of 12 and 16 in) are given in Table 4.6.

Table 4.6: Winch drum dimensions.

D_d	406 / 356 mm	D_t	6 mm
D_c	114 mm	t_f	6 mm
w_d	305 / 406 mm	t_c	6 mm

With the drum size specified it is possible to estimate the amount and location of the tether on the drum. Both drums have a capacity to store $L_{total} = 600$ m of tether. The length of tether on the drum, L_d can be found by subtracting the deployed tether length from L_{total} . For case 1, the length of tether on the drum of winch 1 is near the maximum for the operating range. However for the purpose of determining the motor requirements the maximum value for L_d for the all operational configurations will be applied. This emphasizes that the calculated motor requirements will be sufficient for the most demanding conditions since it will have the maximum inertia and moment arm for the operating range. The location of the tether on the drum at any particular time can be calculated using the following relationships:

$$m_{wraps} = \frac{w_d}{D_t}, \quad L_d = \sum_{i=1}^{n_{wraps}} \pi(D_c + i \cdot D_t \cdot m_{wraps}), \quad r_t = \frac{D_c}{2} + n_{wraps} \cdot D_t$$

where m_{wraps} is the number of axial wraps and n_{wraps} is the number of radial wraps; both calculated as whole numbers. For the case shown in Figure 4.9, $n_{wraps} = 3$ and $m_{wraps} = 11$. To determine n_{wraps} , the summation procedure is incremented until the sum reaches the value for L_d and when this occurs, $n_{wraps} = i$. The results for tether 1 of case 1 are shown in Table 4.7.

The rotational moment of inertia for the winch, J_w is found by summing the inertia of the drum, J_d and that of the tether wrapped on the drum, J_t as: $J_w = J_d + J_t$.

The moment of inertia of the drum was found by summing the inertia of the core (first term) and the two flanges (second term) as:

$$J_d = \frac{1}{2} m_c \left(\frac{D_c}{2} \right)^2 + \frac{\rho_{al} t_f \pi}{2^4} (D_d^4 - D_c^4)$$

where m_c and D_c are the mass and diameter of the core. The mass of the drum was calculated assuming it is made from aluminum with a density, $\rho_{al} = 2700 \text{ kg/m}^3$. The moment of inertia for the tether was:

$$J_t = \frac{1}{2} m_t \left(\frac{r_o^4 - r_i^4}{r_o^2 - r_i^2} \right)$$

where m_t is the mass of the tethers on the drum, r_o is the outer tether radius and r_i is the inner radius ($r_i = D_c/2$). The results for the moment of inertia are shown in Table 4.7.

The winch drum speed and acceleration can be calculated using the tether speed, \dot{L} and acceleration, \ddot{L} and the tether location, r_t using the following equations:

$$\omega_d = \frac{\dot{L}}{r_t}, \quad \alpha_d = \frac{\ddot{L}}{r_t}$$

The results for the winch drum with $w_d = 305 \text{ mm}$ for case 1 are shown in Figure 4.10.

Table 4.7: Winch drum characteristics for tether 1 of case 1 for different drum widths.

$w_d = 305 \text{ mm}$		$w_d = 406 \text{ mm}$	
L_d	330 m	L_d	330 m
m_{wraps}	$50.8 \approx 50$	m_{wraps}	$67.7 \approx 67$
n_{wraps}	10	n_{wraps}	8
r_t	0.114 m	r_t	0.102 m
J_d	0.091 kg-m^2	J_d	0.057 kg-m^2
J_t	0.033 kg-m^2	J_t	0.028 kg-m^2
J_w	0.124 kg-m^2	J_w	0.085 kg-m^2

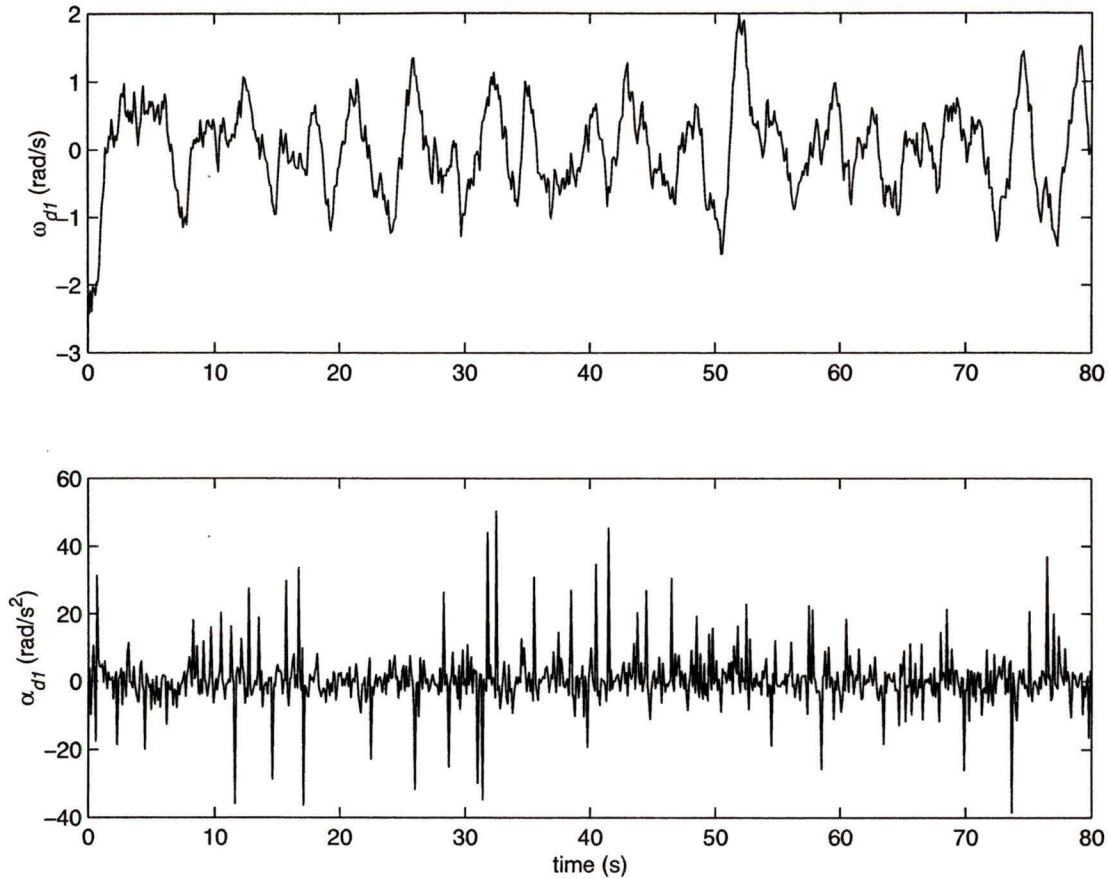


Figure 4.10: Rotational speed and acceleration for drum 1 with $w_d = 305$ mm for case 1 with $P_{max} = 1.5$ kW.

4.4.2.2 General Motor Requirements

With the characteristics of the drum established, the results for the tether motion can now be used to estimate the basic requirements for the motor. The drive system for the winch has three basic mechanical components which are the winch drum, gearing system and the motor. Figure 4.11 shows a diagram of the system.

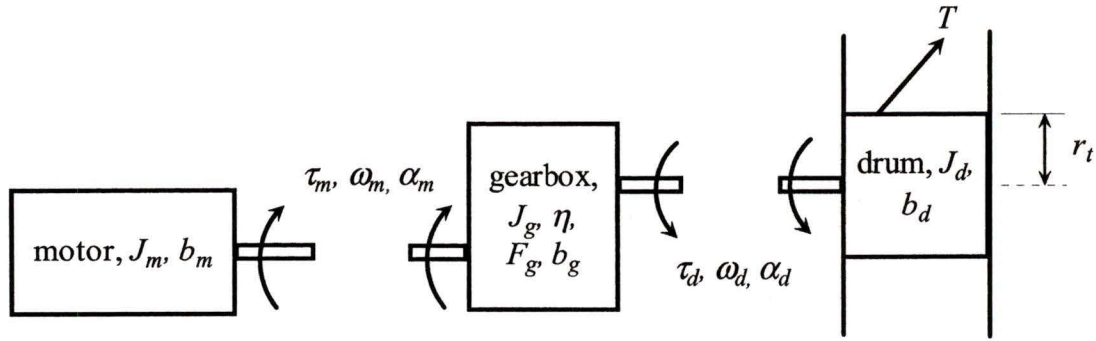


Figure 4.11: Winch motor system.

The equation of motion for the motor output shaft is found by using the rotational equation of motion, $\sum M = J\alpha$ for each component. For the winch drum:

$$\tau_d - Tr_t - b_d\omega_d = J_d\alpha_d$$

where τ_d is the torque applied to the drum, b_d is the friction coefficient for the drum bearing, T is the tether tension, while ω_d and α_d are the angular velocity and acceleration of the drum. Solving for τ_d gives:

$$\tau_d = J_d\alpha_d + Tr_t + b_d\omega_d$$

For the gearbox, the output torque on the drum side, τ_d is divided by both the gear ratio, N and the gear efficiency, η . The equation of motion for the gearbox is:

$$\tau_m - \frac{\tau_d}{\eta N} - F_g - b_g\omega_m = J_g\alpha_m$$

where F_g is the gear static friction torque, b_g is the viscous friction coefficient for the gear, J_g is the moment of inertia for the gear as seen at the input and ω_m and α_m are the angular velocity and acceleration of the motor. Recognizing that $\omega_m = N\omega_d$ and $\alpha_m = N\alpha_d$ and substituting the above expression for τ_d gives the following equation for the motor torque as input to the gearbox:

$$\tau_m = (J_g + \frac{J_d}{\eta N^2})\alpha_m + (b_g + \frac{b_d}{\eta N^2})\omega_m + F_g + \frac{Tr_t}{\eta N}$$

If we consider the electromagnetic torque produced by the motor windings, the motor inertia, J_m and the motor viscous friction coefficient, b_m must be included. Hence, the final equation for τ_m is:

$$\tau_m = (J_m + J_g + \frac{J_d}{\eta N^2})\alpha_m + (b_m + b_g + \frac{b_d}{\eta N^2})\omega_m + F_g + \frac{Tr_t}{\eta N}$$

where τ_m now represents the electromagnetic torque produced, rather than the torque at the output shaft. Alternatively, the torque can be expressed in terms of the previously determined drum speed and acceleration as follows:

$$\tau_m = (J_m + J_g + \frac{J_d}{\eta N^2})N\alpha_d + (b_m + b_g + \frac{b_d}{\eta N^2})N\omega_d + F_g + \frac{Tr_t}{\eta N}$$

At this point very little is known about what gearing or motor will be required so many terms of the above equation are still unknown. Therefore, as a first step, the motor torque will be estimated for a wide range of gear ratios while the following assumptions were made about the motor and gear: $\eta = 0.95$, $J_m = 1.5 \times 10^{-4} \text{ kg-m}^2$, $J_g = 10^{-4} \text{ kg-m}^2$, $F_g = 0.18 \text{ N-m}$ and $b_m = b_g = b_d = 10^{-4} \text{ N-m-s/rad}$. The values for the motor and gear properties are based on average values taken from a Parker Automation catalogue [28]. Results are presented in Table 4.8 for both values of w_d . The values for the motor power, P_m are found by multiplying the rotational speed in rad/s by the torque. The results presented for the motor requirements are for the peak and continuous values taken over the 80 s time history. The continuous values are taken to be the rms values.

From a comparison of the results in Table 4.8 it is apparent that at low gear ratios there is negligible difference in the motor power required for the two drum widths.

However, at higher ratios the power for the wider drum is greater. This suggests that with higher motor speeds and accelerations the additional power required to overcome the inertia and damping effects is more significant than the power reduction due to operating at a lower torque. This trend also explains why the power levels increase as the gear ratio increases. In terms of the design of the winch drum, it appears advantageous to use the narrower drum since this will potentially use less power and reduce the overall size of the complete winch. Therefore, for the remainder of this chapter the winch drum width will be taken as 305 mm.

Table 4.8: Comparison of the rms and peak motor speed, torque and power requirements for two drum widths.

N	$w_d = 305$ mm						$w_d = 406$ mm					
	$(\omega_m)_r$ (rpm)	$(\omega_m)_p$ (rpm)	$(\tau_m)_r$ (N-m)	$(\tau_m)_p$ (N-m)	$(P_m)_r$ (W)	$(P_m)_p$ (W)	$(\omega_m)_r$ (rpm)	$(\omega_m)_p$ (rpm)	$(\tau_m)_r$ (N-m)	$(\tau_m)_p$ (N-m)	$(P_m)_r$ (W)	$(P_m)_p$ (W)
1	6	20	648.3	741.9	419	1577	7	23	580.1	664.0	419	1577
30	185	609	21.8	24.9	422	1591	207	681	19.5	22.4	423	1593
40	247	812	16.4	18.8	424	1597	276	907	14.7	16.8	424	1599
50	309	1015	13.2	15.1	425	1603	345	1134	11.8	13.5	426	1607
60	370	1218	11.0	12.6	426	1610	414	1361	9.9	11.3	427	1615
70	432	1421	9.5	10.9	427	1618	483	1588	8.5	9.9	429	1641
80	494	1624	8.3	9.7	429	1645	552	1815	7.4	8.9	430	1690
90	555	1827	7.4	8.8	430	1689	621	2042	6.6	8.2	432	1745
100	617	2030	6.7	8.2	432	1739	690	2269	6.0	7.6	433	1808
110	679	2233	6.1	7.7	433	1794	759	2496	5.5	7.2	434	1874
120	740	2436	5.6	7.3	434	1852	827	2722	5.0	6.8	437	1947
130	802	2639	5.2	6.9	436	1915	896	2949	4.7	6.6	438	2026
140	864	2842	4.8	6.7	438	1982	965	3176	4.4	6.4	440	2122
150	926	3045	4.5	6.1	439	1951	1034	3403	4.1	6.2	444	2209

To understand the different factors contributing to the motor torque, the various terms are displayed individually for the drum with $w_d = 305$ mm and $N = 100$ at the instant the torque is at its peak value:

$$\text{inertia term: } (J_m + J_g + \frac{J_d}{\eta N^2})N\alpha_d = 1.21 \text{ N-m}$$

$$\text{damping term: } (b_m + b_g + \frac{b_d}{\eta N^2})N\omega_d = 0.01 \text{ N-m}$$

$$\text{gear friction torque: } F_g = 0.18 \text{ N-m}$$

$$\text{tether loading: } \frac{Tr_t}{\eta N} = 6.81 \text{ N-m}$$

$$\text{total: } = 8.21 \text{ N-m}$$

This shows that the tether load is the most dominant influence on the motor torque.

4.4.2.3 Motor Selection

With the first pass completed for estimating the motor requirements, the next step is to examine specific motor technologies in search of a motor capable of fulfilling the requirements. From the results in Figure 4.10 it is clear that the motor must be extremely responsive and capable of changing direction every few seconds. Traditional motion control applications typically employ either stepper or servo motors. Figure 4.12 presents common types of stepper and servo motors.

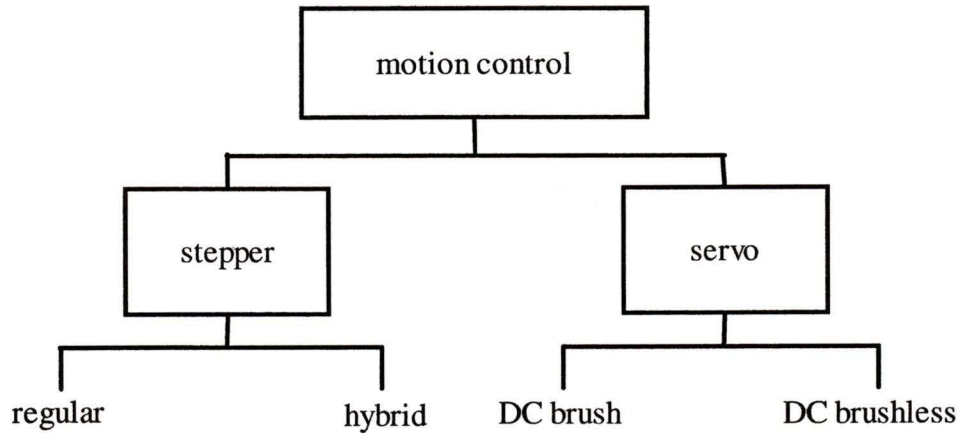


Figure 4.12: Family of motors used for conventional motion control applications.

It is unlikely that a stepper motor can satisfy the demanding dynamic requirements established for our winching system. Stepper motors tend to be cheaper than servos and function well in high torque, low speed, continuous duty applications, but because our application involves rapidly changing motor output, a stepper motor is not suitable. Stepper motors are also less suitable for closed loop control applications. For our application a servo motor is expected to have superior reliability, efficiency and accuracy than a stepper.

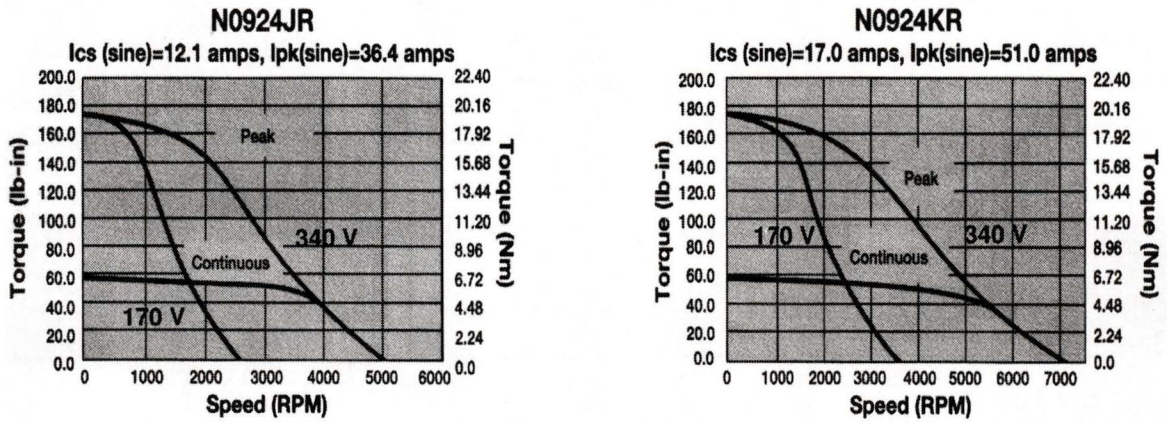
There are two distinct advantages of the DC brushless servo motor over the DC brush servo which are pertinent to our application. The first is that the brushless motor is much more reliable in terms of maintenance free operation since the brushes are susceptible to wear. This is important since the motors will be operated remotely in a large field. Secondly, the brushes can limit the motor's potential for frequent stop, starts and direction changes. This limitation is critical since the performance of our tethered positioning system hinges on the motor's capability to deliver fast and accurate motion that includes frequent direction changes. Therefore, the brushless servo motor appears to be the best solution for our winch system.

4.4.2.4 Off the Shelf Servo Motors

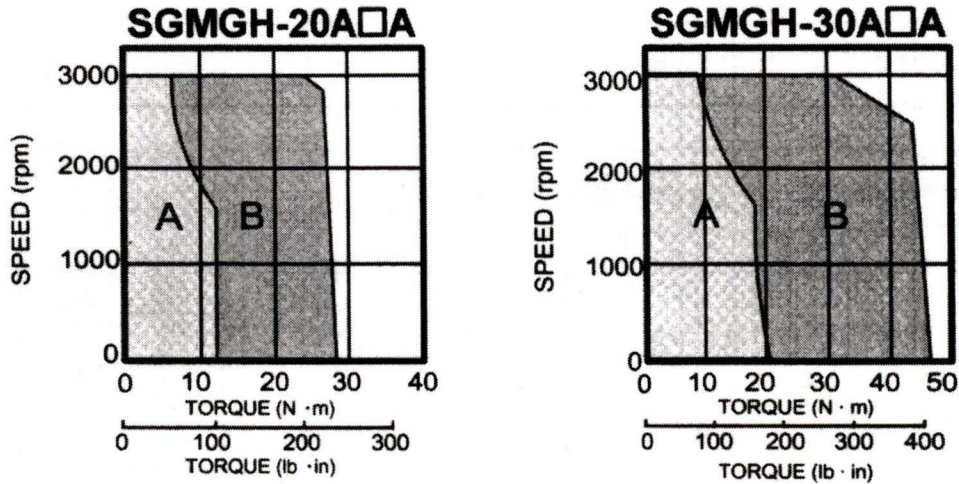
The products of many motor manufacturers and automation groups were reviewed in search of a brushless servo motor that meets the torque and speed specifications presented in Table 4.8. Although most servo motor systems surveyed involved small motors with insufficient power output, several manufacturers were identified with motors that meet and exceed our power requirements. Among these, the search was narrowed further by focusing on large established manufacturers that offer a complete range of auxiliary components such as motor amplifiers and motion control hardware. The premise for this evaluation criterion is that a reliable and integrated motion control system provided by a single manufacturer would reduce the time and effort required for the initial set-up and operation of the system. Also, the availability of comprehensive technical information and assistance was an important factor in selecting a suitable motor manufacturer. Motor performance indicators such as torque to inertia ratio or torque output per Amp of input current were also considered in the selection process.

Motors from two manufacturers, Parker Automation and Yaskawa, were chosen for subsequent evaluation and comparison. The torque vs. speed curves for two motors from each manufacturer are shown in Figure 4.13. The two Parker motors have nearly identical physical parameters as the only difference between the two motors is the type of winding. The difference between the Yaskawa motors is the size and power. The distinctive difference between the motors of the two companies is that the Parker motors deliver lower torque at higher maximum speeds compared to the Yaskawa motors which deliver higher torque but at a lower maximum speed. Table 4.9 lists the specifications for

each motor. Another notable difference between the motors is the rotor inertia. The inertia for the Parker motors is about 20 times less than that of the Yaskawa motors.



a)



b)

Figure 4.13: Speed vs. torque curves for servo motors manufactured by a) Parker Automation (one set of curves for different voltages) [28] and b) Yaskawa [35].

Table 4.9: Specifications for selected servo motors [28] [35].

	NO924JR	NO924KR	SGMGH-20A	SGMGH-30A
stall torque cont. (Nm)	6.84	6.86	11.5	18.6
peak torque (Nm)	20.50	20.58	28.7	45.1
rated speed (rpm)	3600	5200	3000	3000
power at rated speed (kW)	1.97	2.63	2.4	3.9
damping, b (Nm/rad/s)	9.4×10^{-5}	9.4×10^{-5}	N/A	N/A
rotor inertia ($\text{kg}\cdot\text{m}^2$)	1.5×10^{-4}	1.5×10^{-4}	31.7×10^{-4}	46.0×10^{-4}

4.4.2.5 Gearing

The gearing system for the motor is an important consideration when evaluating the various motors. It is obvious that the Parker motors will require a larger gear ratio since they produce less torque while operating at higher speeds than the Yaskawa motors. Both companies market their motors with the option of including a planetary gearhead mounted directly to the motor. The largest gear ratio available in a single stage is $N = 10$. Based on the basic motor requirements estimated previously in Table 4.8 the approximate gear ratio for each motor can be predicted using the continuous torque and speed ratings. For example, for the NO924JR and NO924KR, the continuous torque is 6.84 to 6.86 Nm which necessitates a gear ratio of at least $N = 100$. Similarly, for the SGMGH-20A, $N = 60$ and for the SGMGH-30A, $N = 40$. Therefore it is clear that at least two stages of gearing are required if the inline planetary gearheads are to be used. It is possible to achieve $N = 60$ with a single gear reduction with other gear types, however the size of such a gear would cause mounting problems on the winch.

Typically when the gear ratio for a winch requires a multiple stage reduction, one of these stages is provided by a chain and sprocket system. This is an acceptable option for most winches since rapid, precise movements and direction changes are not required. For our winch, the backlash introduced by a chain would compromise the ability of the winch to react quickly and accurately. Consequently, the winch drive system will be designed to minimize backlash by connecting the gearhead directly to the drum axle.

For the purpose of this analysis it will be assumed that the motor will be accompanied by a planetary gear for the first stage of the gear reduction. There are several different gearing options for the second stage. The basic features of common types of gearing for DC motor applications are given in Table 4.10. The most common gear reducers used with DC motors are worm gears and hence are available with a wide range of speed and torque capabilities, several of which fulfill our requirements. High efficiency and high speeds can be achieved with a hypoid gearhead, however none were found that satisfy the output torque required to drive the winch drum. The same is true for the planetary gearheads manufactured by Parker. Therefore, if a Parker motor is used, a second stage worm gear must be included. Yaskawa manufactures planetary gearheads with adequate output torque and are available in two stages with a gear reduction up to $N = 50$. This suggests that if the 30A model is used, two-stage planetary gearing will suffice.

Table 4.10: Common gearing types for DC motors

gear type	features
planetary	small gear ratio, compact, high efficiency, inline with input, high speed
hypoid	high efficiency, right angle to input, high speed
worm	large gear ratio, non-backdriveable, low efficiency, right angle to input, low speed

The non-backdriveability of a worm gear has potential advantages for the winch system. The term backdriveable relates to the gearheads ability to be turned from the output side. For a worm gear, the input shaft can not be turned by applying a load to the output shaft. This could prove to be a valuable feature as the ability of the winch system to operate in a passive mode where the tether lengths are fixed is essential. It is also possible to use an electronic brake incorporated with the motor to prevent winch motion. However, relying on the worm gear to prevent tether motion is attractive since no electrical or accessory components are required.

4.4.2.6 Advanced Motor Requirements

A more detailed estimation of the motor requirements using the actual characteristics of the Parker and Yaskawa motors with realistic gearhead properties is required before a firm decision can be made for the motor selection. Since two gearing stages are required for each motor the equation of motion must be modified as follows:

$$\tau_m = (J_m + J_{g1} + \frac{J_{g2}}{\eta_1 N_1^2} + \frac{J_d}{\eta N^2}) N \alpha_d + (b_m + b_{g1} + \frac{b_{g2}}{\eta_1 N_1^2} + \frac{b_d}{\eta N^2}) N \omega_d + F_{g1} + \frac{F_{g2}}{\eta_1 N_1^2} + \frac{Tr_t}{\eta N}$$

where $\eta = \eta_1\eta_2$ is the combined efficiency and $N = N_1N_2$ is the combined gear ratio.

The updated motor requirements found using this equation are displayed in Table 4.11 for the case with $P_{max} = 1.5$ kW and in Table 4.12 for the case with $P_{max} = 3.0$ kW . One set of motor requirements was calculated for each motor manufacturer. The motor inertia, J_m used in the equation is listed in Table 4.9. For the Yaskawa results J_m was taken from the -30A model since it is the larger of the two. A conservative estimate for the inertia of each gear stage of $J_{g1} = J_{g2} = 5 \times 10^{-4}$ kgm² was used. This value represents the maximum inertia found for planetary gears of the appropriate size and torque. The remaining parameters correspond to those used previously for generating Table 4.8.

Table 4.11: Motor requirements with actual motor characteristics and multiple gear stages for maximum power case of 1.5 kW.

N_1	N_2	N	$(\omega_m)_r$ (rpm)	$(\omega_m)_p$ (rpm)	$(\tau_m)_r$ (N-m)	$(\tau_m)_p$ (N-m)	$(P_m)_r$ (W)	$(P_m)_p$ (W)
Yaskawa								
3	10	30	185	609	23.1	31.4	447	2000
4	10	40	247	812	17.4	27.8	450	2363
5	10	50	309	1015	14.1	26.9	456	2857
3	20	60	370	1218	12.0	27.3	464	3480
3	25	75	463	1523	10.0	28.9	483	4603
4	20	80	494	1624	9.5	29.5	491	5014
20	4	80	494	1624	9.5	29.3	490	4990
Parker								
10	10	100	617	2030	7.1	10.4	456	2211
4	30	120	740	2436	6.0	10.1	461	2574
5	25	125	771	2538	5.73	9.95	463	2644
5	30	150	926	3045	4.85	9.88	470	3150

Table 4.12: Motor requirements with actual motor characteristics and multiple gear stages for maximum power case of 3 kW.

N_1	N_2	N	$(\omega_m)_r$ (rpm)	$(\omega_m)_p$ (rpm)	$(\tau_m)_r$ (N-m)	$(\tau_m)_p$ (N-m)	$(P_m)_r$ (W)	$(P_m)_p$ (W)
Yaskawa								
3	10	30	275	1206	25.1	46.6	723	5881
4	10	40	367	1608	18.4	46.2	708	7776
5	10	50	459	2010	15.7	49.7	756	10465
3	20	60	551	2412	14.5	54.8	833	13847
3	25	75	689	3015	14.5	54.8	1042	17308
4	20	80	734	3216	14.0	65.9	1079	22200
20	4	80	734	3216	14.0	65.6	1075	22076
Parker								
10	10	100	918	4020	7.3	16.2	704	6837
4	30	120	1102	4824	6.4	17.4	736	8765
5	25	125	1148	5025	6.2	17.4	743	9146
5	30	150	1377	6030	5.5	18.8	799	11852

The order in which the gearing stages are arranged can affect the results as the inertia of the second stage, J_{g1} gets divided by the ratio of the first gear squared, N_1^2 . Since the motors can be equipped with factory planetary gears it is likely that the smaller gear stage will be N_1 . For the case when $N = 80$, the gear order was rearranged to determine what benefit changing the order of the gears would have on the results. A slight decrease in the motor's peak torque is observed, but overall the difference is not significant enough to warrant rearranging the gear order.

The results for the Yaskawa motor show a significant increase in the peak torque from what was observed for the basic motor in Table 4.8. This increase is a result of the increase to the motor inertia by a factor of 30. Although the gear inertia also increased and an additional stage of gearing was included, the large increase in peak torque is attributable mostly to the change in motor inertia. From the quantitative breakdown of torque terms presented in section 4.4.2.3, the term with the motor inertia accounted for 1.21 Nm of the total of 8.21 Nm. With an increase of J_m by a factor of 30, the inertia term for that case would increase to 21.2 Nm. This effect is much more pronounced at higher gear ratios since the angular acceleration increases proportionally with N , which is demonstrated by the rise in peak power as N increases for the Yaskawa results.

The results for the torque and speed of the 3.0 kW case are expectedly higher than for the 1.5 kW case. A very substantial increase to the peak power is observed between the two power levels which is due to the rise in motor speed and acceleration. Comparing the results in Table 4.11 and Table 4.12 to the motor curves in Figure 4.13 the final gear ratio required for each motor can be determined. The results are summarized in Table 4.13 along with the peak power required for that ratio.

Table 4.13: Minimum gear ratio required for each motor at both power levels

motor	min N @ 1.5 kW	$(P_m)_p$ (W)	min N @ 3.0 kW	$(P_m)_p$ (W)
Parker 9024JR	120	2574	N/A	N/A
Parker 9024KR	120	2574	N/A	N/A
Yaskawa SGMGH-20A	75	4603	N/A	N/A
Yaskawa SGMGH-30A	40	2363	40	7776

All four motors meet the torque and speed requirements for the 1.5 kW case however the dramatic increase of requirements observed for the 3.0 kW case preclude the Parker motors and the SGMGH-20A from being used at this power level. The peak power levels are significantly higher than the maximum power limit of 1.5 kW and 3.0 kW established in section 4.4.1.2 using an ideal winch. The inflated peak power levels are the result of losses in the gearing and accounting for the inertia in the system. This trend is most prevalent at the 1.5 kW level for the 20A model which has a peak power of 4.6 kW. This is well beyond the limit of the 2 kW power level set for this case and even exceeds the maximum available site power of 4 kW. Furthermore, the peak power levels of all the motors for the 1.5 kW case are greater than the 2 kW power limit. This suggests that the predicted 75% efficiency between the ideal winch output and the actual motor input was too optimistic. Therefore, if the available power is only 2 kW, the tether motion should be found using the maximum ideal winch power of 1 kW and the motor selection process should be revisited.

Assuming the peak power level of 4 kW is available at the site, either Parker motor or the SGMGH-30A are suitable for our application. The significant advantage of the Parker motors over the 30A is the smaller rotor inertia. The response time of the motor will be shorter for a system with less inertia. However, there is a limit to how small the rotor inertia can be in relation to a particular load inertia in order for the motor to work properly. Parker recommends that the load inertia to motor inertia ratio not exceed 20. For our winch, the load inertia is $J_w = 0.124 \text{ kgm}^2$, but the load inertia as seen by the motor is J_d / N^2 . For $N = 120$ the load inertia at the motor is $0.124 / 120^2 = 8.6 \times 10^{-6}$

which is well below the rotor inertia of the Parker motors and therefore the load to rotor inertia ratio is not a concern.

The final decision for selecting the most suitable motor should be made once a comparison of each motor's transient behavior is performed. However, based on the present work, either Parker motor is recommended for the winch design since it has smaller rotor inertia than the Yaskawa motors. The 90n4KR model may be preferable over the 9024JR since it has higher speed capabilities.

4.4.2.7 Motor Amplifier and Controller

The physical architecture of the motion control system will now be addressed. A PC based control system was chosen because of the PC's versatility and familiarity. Both motor manufacturers offer a range of automation hardware used to control and drive the motors in conjunction with a PC based system. A schematic of the overall control system is displayed in Figure 4.14. The basic operation of the system can be summarized as:

- PC collects data from GPS and other sensors, this data is used by the control algorithm which produces digital commands to the control board of each motor (low frequency, approx. 10 Hz),
- the control board receives commands from the PC and using position and velocity data from the motor, issues analog commands to the amplifier,
- the amplifier supplies the voltage and current required to drive the motor.

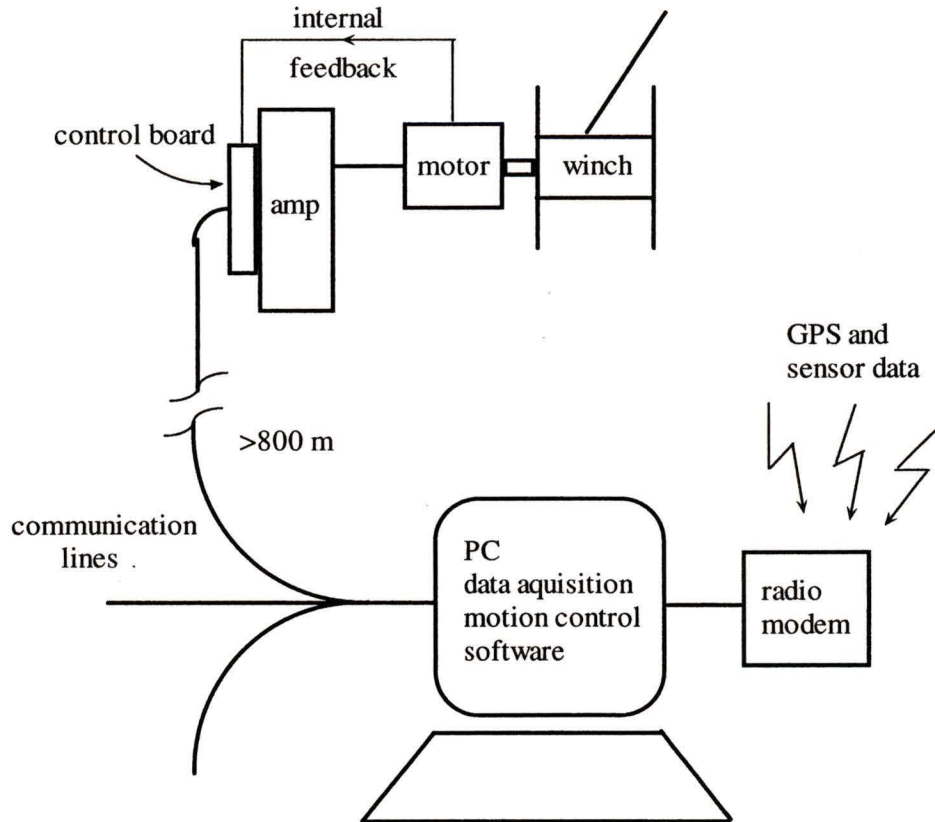


Figure 4.14: Schematic of PC based motion control system for aerostat positioning system.

As mentioned previously in section 2.1, the position of the payload is the outer feedback variable for the winch control system. The GPS onboard the payload will provide position data to the PC at 10 Hz. The control algorithm on the PC will process this data and issue speed commands to the winch motor. The motor has an inner feedback control loop which operates at much higher frequencies of several hundred Hz. The feedback variables for this loop are the motor's position and velocity which are measured by an optical encoder or a magnetic resolver. Depending on the effectiveness of this control strategy certain modifications may be attempted in order to improve performance. For instance, it may prove beneficial to enhance the control algorithm by incorporating

extrapolation and estimation techniques for the position and velocity of the payload for the intervals between the 10 Hz GPS updates.

There are several issues that arise from the long communication distance from the PC to the motor. Each winch is located along the perimeter of an 800 m circle and the PC is located inside a trailer which is just outside the perimeter. Thus, the distance from the PC to any of the motors could exceed 800 m. The output from the control board and amplifier is analog voltage and it is not possible to transmit this type of signal the required 800 m without frequent signal boosting. The maximum recommended connection distance for the amp to the motor is 30 m while for the control board to the amp is 15 m. The communication between the PC and control board is digital and hence much longer distances are possible. For RS-485 protocol, with a regular twisted pair line can, transmission distances can reach up to 1200 m. This limits the possibilities for arranging the components of the motion control system to the configuration shown in Figure 4.14 with the control board and amplifier both located at or near the winch.

Control boards manufactured by Yaskawa and Parker are capable of supporting RS-485 communication and with a maximum baud rate of 9600. The arrangement of the multiple motor communication system will depend on the motor's required data rate for operation. In order to obtain the greatest communication bandwidth between the PC and the control boards, it is suggested that a separate serial port be dedicated to each winch. Since two ports are already being used by the data acquisition system an additional board with at least 3 new ports must be added to the PC. The final configuration of the communication system will be determined once a specific motor is selected and its required communication input is known.

Chapter 5

Conclusions

5.1 Dynamics Model

The dynamic analysis of the scaled tethered aerostat system was based on furthering the development of an earlier dynamics model created by Nahon [25]. The initial step was to obtain the general physical properties of the system applying scaling laws to the original design of the original LAR tethered aerostat system [9]. The relevant dynamic variables of the system were arranged into dimensionless groups using the principles of the Buckingham Pi theorem [19]. Due to the required similarity of certain environmental conditions, it was not physically possible to satisfy all the dimensionless terms. Specifically, the conflicting dimensionless terms that could not be simultaneously satisfied were Reynolds' number, Re and Froude's number, Fr . To investigate which of the two terms is more critical for establishing similarity, the dynamics model was used. A comparison of the simulation results between scaled systems (one with proper Re scaling and one with proper Fr scaling) and the full system indicated that the system with proper

Fr scaling showed much better agreement. The dynamics model of the scaled system was therefore based on the properties provided by scaling the system while maintaining *Fr* and not *Re* similarity.

The damping and elastic properties of the tether required for the dynamics model were determined using an experimental approach. The experimental results were obtained by measuring the tension dissipation in a sample of *Plasma* [29] tether material. The near logarithmic decrement of the measured response establishes credibility for a viscous damping approximation for the tether's internal damping behavior. From the results, estimates for both elastic modulus, $E = 37.4$ GPa and the damping ratio, $\zeta = 0.017$ were obtained. The results for E showed excellent agreement with the published value differing by only 1%. There was no data available for comparison of the damping characteristics of the *Plasma* tether; however, the results for ζ are similar to the damping ratio of 0.015 measured by Hamilton for a different synthetic tether [11].

The dynamics model for a basic spherical aerostat was improved by incorporating realistic vortex shedding oscillations. Previous experimental results from Govardham and Williamson [10] were used to estimate the relationship for amplitude and frequency of the oscillations with respect to wind speed. The oscillatory motion of the aerostat was achieved by applying a transverse sinusoidal force to the aerostat's center of mass. The magnitude of the required force was determined using trial and error with the simulation results. With the vortex shedding oscillations incorporated into the dynamics model, the response of the payload motion was compared with the original aerostat to determine the extent of any performance degradation. The rms value of the in-focal-plane error of the payload increased from 3.1 cm without vortex shedding to 7.2 cm with vortex shedding

for the passive system in the symmetrical configuration. Although the error more than doubled, the error of only 7.2 cm demonstrates the rigidity of the tension structure, especially considering that the amplitude of the aerostat oscillation during the test was 2.64 m. The results for the same case with the control system activated showed that the rms in-plane error would increase from 3.5 mm to 11 mm with the addition of vortex shedding. Even with the increase, the error is considered to be very small considering the magnitude of the overall system.

A second and more complicated aerostat was added to the dynamics model. This aerostat has a streamlined shape with three tail fins for directional stability. The dynamics model was developed by partitioning the aerostat into individual components, including the hull and three tail fins. The aerodynamic influence of each component is included in the equations of motion for the aerostat. Simulation results for the tri-tethered aerostat system in the symmetrical configuration are encouraging as the maximum in-focal-plane error is only 8 mm with a wind speed $U = 6$ m/s.

A detailed investigation of the performance of the streamlined aerostat was accomplished by using the dynamics model to conduct a linear stability analysis. A numerical linearization of the state matrix for the motion of the aerostat on a single tether was performed. The properties of the resulting matrix indicated that the aerostat motion decoupled into traditional longitudinal and lateral motion. Therefore the state matrix was split into separate lateral and longitudinal sub-matrices which were analyzed separately. The eigenvalues and eigenvectors of the state matrix were used to characterize the behavior of the system into identifiable modes. The eigenvalues for every mode possessed negative real parts indicating the system is stable. The frequency of certain

modes was compared with the corresponding analytical frequency for that mode and very good agreement was observed. This provides an initial step towards assessing the general validity of the dynamics model. The linear results were also used to gain insight into the effect of adjusting certain physical features of the aerostat system. The two physical features studied were the tether length and the steady-state pitch angle of the aerostat. From observing the results for tether lengths of 33.3 m, 100 m and 300 m it was found that the stability of the tether modes (*i.e.* axial spring mode and transverse harmonic modes) decrease appreciably as the tether length decreases. This is attributed to the reduction of the damping influence from the wind. For the various pitch angles studied, $\theta_0 = -1^\circ$, -4° and -7° (pitched up) there was little difference between the characteristics of the modes.

5.2 Experimental System Design

The conceptual design for the experimental scaled aerostat system occurred simultaneously with the dynamics model development. Like the dynamic analysis, the starting point of the experimental system design was the scaling results from the original LAR conceptual design [9]. The primary components that were selected during the design process were the aerostat, the tethers and the winching system.

A comparison of the expected performance of three distinct aerostat types; 1) streamlined, 2) spherical and 3) variable lift, was performed in order to choose the most suitable aerostat for this application. The variable lift aerostat demonstrated poor stability and reliability during flight tests and therefore was not considered for further comparison. The streamlined aerostat was chosen as the best option and a 20 m streamlined aerostat

was purchased from Aeros Flightcam of Canoga Park California. This decision was based on the advantages of the aerodynamic shape of the streamlined aerostat. Its wind induced drag is less than half of that of a comparable spherical aerostat. This results in smaller horizontal disturbances to the payload and to a reduced external pressure on the hull which poses less of a threat to its integrity during high winds. It is acknowledged that the ground handling equipment and procedures for the streamlined aerostat are more complicated and cost intensive than for a spherical aerostat. However, the NRC has shown a strong commitment to construct adequate equipment and provide sufficient personnel for operation of the streamlined aerostat.

The selection of the tether material was made based on two factors; strength to weight ratio and stiffness. *Plasma* from Puget Sound Rope was chosen for the tether material since it ranked the highest in both categories. The elastic modulus of *Plasma* is greater than the elastic modulus required by direct scaling of the full scale system, but it was decided to deviate from strict dynamic similarity in favor of obtaining better performance from the system. The safety factor for the break strength of the tether is 5.1 for the expected tether load of 7.02 kN at a maximum wind speed of 20 m/s.

The design of the tether winching system relied heavily on simulation results from the dynamics model. The basic components of the winch are a motor, a gearhead and a winch drum. The complete dynamics model for the tethered system with the Aeros aerostat and actively controlled tethers was used to estimate the required tether motion for operation with wind speeds up to 6 m/s. Many different configurations were studied in order to find which had the most power intensive requirements. The resulting tether motion and tension for this case were used to establish the torque and speed

specifications for the winch. A comparison of several motor and gearing systems was performed. The basis of the comparison was the input power required to achieve the output winch torque and speed. It was found that a DC servo motor with a two stage gear reduction combining an initial planetary gear and a secondary worm gear is most suitable for the winch system.

5.3 Recommendations

The following recommendations pertain to the dynamics model:

- improve the aerodynamic parameter estimation for the aerostat. Specifically, the estimate for the cross-flow drag coefficient, should be based on a more representative shape than a cylinder.
- incorporate realistic time delays into the control system. Specifically the time delays associated with the limited update rate and the latency of the GPS system.

The following recommendations pertain to the experimental system:

- finalize the selection of parts for the winch drive system. Proceed with construction of the winches.
- initiate testing of the multi-tethered system with fixed tether lengths. Validate the dynamics of the passive system before progressing to the complete controlled system.

References

- [1] S. Badesha, S.P. Jones. Aerodynamics of the TCOM 71M Aerostat, *AIAA Paper* 93-4036: 36-42, 1993
- [2] B. Buckham, M. Nahon, M. Seto. Three-Dimensional Dynamics Simulation of a Towed Underwater Vehicle, *Proceedings of 18th International Conference on Offshore Mechanics and Arctic Engineering*, 1-8, 1999.
- [3] B. Carlson *et al.* The Large Adaptive Reflector: a 200-m diameter, wideband, cm-m wave radio telescope. *Proceedings of the SPIE International Symposium on Astronomical Telescopes and Instrumentation*, 33-44, 2000.
- [4] Cortland Cable Company, Inc. Technical Data Sheet 105, 1987.
- [5] J.D. DeLaurier. A stability Analysis for Tethered Aerodynamically Shaped Balloons, *AIAA Journal of Aircraft*, 9(9):646-651, 1972.
- [6] J.D. DeLaurier. Prediction of Tethered-Aerostat Response to Atmospheric Turbulence, *AIAA Journal of Aircraft*, 14(4):407-409, 1977.
- [7] R. Driscoll, M. Nahon. Mathematical Modeling and Simulation of Moored Buoy System, *Proceedings of Oceans*, 1:517-523, 1996.

- [8] B. Etkin. Stability of a Towed Body, *AIAA Journal of Aircraft*, 35(2):197-205, 1998.
- [9] J.T. Fitzsimmons, B. Veidt, P.E. Dewdney. Steady-state analysis of the multi-tethered aerostat platform for the Large Adaptive Reflector telescope. *Proceedings of the SPIE International Symposium on Astronomical Telescopes and Instrumentation*, 476-488, 2000.
- [10] R. Govardham, C.H.K. Williamson. Vortex-induced motions of a tethered sphere, *Journal of Wind Engineering and Industrial Aerodynamics*, 69(71):375-385, 1997.
- [11] J.M. Hamilton. Vibration-Based Techniques for Measuring the Elastic Properties of Ropes and the Added Mass of Submerged Objects, *Journal of Atmospheric and Oceanic Technology*, 17(5):688-697, 2000.
- [12] D. Hopkin, V. den Hertog. The Hydrodynamic Testing and Simulation of an Autonomous Underwater Vehicle. *Proceedings of the Second Canadian Marine Dynamics Conference*, 274-281, 1993.
- [13] D.E. Humphreys. Validation of the Dynamic Characteristics of a Towed, Scaled Aerostat, *Proceedings from the 12th AIAA Lighter-Than-Air Systems Technology Conference*, 227-236, 1997.
- [14] G.W. Jones Jr. Investigation of the Effects of Variations in the Reynolds Number Between 0.4×10^6 and 3.0×10^6 on the Low-speed Aerodynamic Characteristics of Three Low-Aspect-Ratio Symmetrical Wings With Rectangular Plan Forms, *NACA Research Memorandum RM LG2G18:1-13*, 1952.

- [15] S.P. Jones. Nonlinear Dynamic Simulation of a Moored Aerostat, *AIAA 7th Lighter-than-Air Technology Conference*, AIAA-87-2505, 1987.
- [16] S.P. Jones, J.D. DeLaurier. Aerodynamic Estimation Techniques for Aerostat and Airships, *AIAA Journal of Aircraft*, 20(2):120-126, 1983.
- [17] S.P. Jones, J.A. Krausman. Nonlinear Dynamic Simulation of a Tethered Aerostat, *AIAA Journal of Aircraft*, 19(8):679-686, 1982.
- [18] S.P. Jones, L.D. Shroeder. Nonlinear Dynamics Simulation of a Tethered Aerostat: A Fidelity Study, *AIAA Journal of Aircraft*, 38(1):64-68, 2001.
- [19] I.A. Khan. *Fluid Mechanics*, Holt, Rinehart and Winston, New York, NY, 1987.
- [20] C. Lambert, M. Nahon, B. Buckham, M. Seto. Dynamics Simulation of Towed Underwater Vehicle System, Part II: Model Validation and Turn Maneuver Optimization, submitted Oct 2001 for publication in *Journal of Ocean Engineering*.
- [21] R.C. LeClaire, C.B. Rice. The Local Motions of a Payload Supported by a Tritethered Natural Shape Balloon, *US Air Force Report AFCRL-TR-73-0748*, 1-43, 1973.
- [22] T.H. Legg. A proposed new design for a large radio telescope, *Astronomy and Astrophysics Supplement Series*, 130, 369-379, 1998.
- [23] B.W. McCormick. *Aerodynamics, Aeronautics and Flight Mechanics*, John Wiley & Sons, 1995.
- [24] M. Nahon. A Simplified Dynamics Model for Autonomous Underwater Vehicles, *IEEE Proceedings of AUV'96*, 373-379, 1996.

- [25] M. Nahon. Dynamics and Control of a Novel Radio Telescope Antenna, A Collection of the *AIAA Modeling and Simulation Technologies Conference Technical Papers*, 214-222, 1999.
- [26] M. Nahon, G. Gilardi, C. Lambert. Dynamics and Control of a Radio Telescope Receiver Supported by a Tethered Aerostat, submitted Oct 2001 for publication in *AIAA Journal of Guidance, Dynamics and Control*.
- [27] J.N. Newman. *Marine Hydrodynamics*, MIT Press, 1989.
- [28] Parker Hannifin Corporation. Compumotor Motion Control Systems, *Catalog 8000-3/USA*, 1999.
- [29] Puget Sound Rope PLASMA 12 Strand data sheet available at www.psrope.com.
- [30] T. Redd, R. Bland, R.M. Bennet. Stability Analysis and Trend Study of a Balloon Tethered in a Wind, With Experimental Comparisons, NASA TN D-7272, Langley Research Center, 1-109, 1973
- [31] H. Sakamoto, H. Hainu. A study on Vortex Shedding From Spheres in a Uniform Flow, *ASME Journal of Fluids Engineering*, 112:386-392, 1990.
- [32] R. Taylor. The Square Kilometer Array, University of Calgary (<http://www.ras.ucalgary.ca/SKA/>).
- [33] R. van de Weygaert, T.S. van Albada. New Challenges for Cosmology, The Westerbork Observatory, *Continuing Adventure in Radio Astronomy, Astrophysics and Space Science Library* 207:225-259, 1996.
- [34] F.M. White. *Fluid Mechanics*, McGraw-Hill, Inc., 1994.

[35] Yaskawa Electric America Inc. Sigma II Servo System Product Catalog
Supplement, 2000.

Appendix A

Arrangement of Dynamic Parameters into Dimensionless Terms

Step one is to arrange the relevant parameters in an n by m dimensional matrix as follows (n is the number of relevant parameters and m is the number of fundamental units present in the n parameters):

	ρ_e	l	U	m	I	F	ρ	E	b	μ	g	t	f
M	1	0	0	1	1	1	1	1	1	1	0	0	0
L	-3	1	1	0	2	1	-3	-1	0	-1	1	0	0
T	0	0	-1	0	0	-2	0	-2	-1	-1	-2	1	-1

Step two is to choose m repeating variables. The repeating variables must contain among them the m fundamental dimensions. It is also essential that none of the repeating variables be derivable from the other repeating variables. For this procedure, the first three variables, ρ_e , l and U are chosen as the repeating variables.

Step three is to arrange the repeating variable sub-matrix to an identity matrix, by adding or subtracting multiples of the entries in that sub-matrix. When an

operation is performed, the variable at the top of the matrix is changed to reflect the operation. The following set of rules apply:

- multiplication of a column by X raises that variable to the power of X.
- addition of column A to column B multiplies the variable in B by the variable A.
- subtraction of column A from column B divides the variable in B by the variable A.
- columns may be exchanged.

These operations are now carried out on the dimensional matrix:

	$\rho_e l^3$	l	l/U	m	I	F	ρ	E	b	μ	g	t	f
M	1	0	0	1	1	1	1	1	1	1	0	0	0
L	0	1	0	0	2	1	-3	-1	0	-1	1	0	0
T	0	0	1	0	0	-2	0	-2	-1	-1	-2	1	-1

Step four is to reduce the rest of the entries of dimensional matrix to zeros by adding or subtracting various multiples of the columns in the identity sub-matrix. The same rules apply as in step 3. The result of this process is the following matrix:

	$\rho_e l^3$	l	$\frac{l}{U}$	$\frac{m}{\rho_e l^3}$	$\frac{I}{\rho_e l^5}$	$\frac{F}{\rho_e U^2 l^2}$	$\frac{\rho}{\rho_e}$	$\frac{E}{\rho_e U^2}$	$\frac{b}{\rho_e U l^2}$	$\frac{\mu}{\rho_e U l}$	$\frac{g l}{U^2}$	$\frac{t U}{l}$	$\frac{f l}{U}$
M	1	0	0	0	0	0	0	0	0	0	0	0	0
L	0	1	0	0	0	0	0	0	0	0	0	0	0
T	0	0	1	0	0	0	0	0	0	0	0	0	0

The terms to the right of the identity matrix are the $n - m$ dimensionless terms.

Vita

Surname: Lambert

Given Names: Casey Marcel

Place of Birth: Calgary, Alberta, Canada

Date of Birth: August 4, 1975

Educational Institutions Attended:

University of Calgary 1994 to 1999

University of Victoria 2000 to 2002

Degrees Awarded:

B.A.Sc (Mechanical Engineering) University of Calgary 1999

Honours and Awards:

Science Council of BC GREAT Award, University of Victoria 2000 to 2002

Publications:

B. Buckham, M. Nahon, M. Seto, X. Zhao, C. Lambert. Dynamics Simulation of Towed Underwater Vehicle System, Part I: Model Development, submitted Oct 2001 for publication in *Journal of Ocean Engineering*.

C. Lambert, M. Nahon, B. Buckham, M. Seto. Dynamics Simulation of Towed Underwater Vehicle System, Part II: Model Validation and Turn Maneuver Optimization, submitted Oct 2001 for publication in *Journal of Ocean Engineering*.

M. Nahon, G. Gilardi, C. Lambert. Dynamics and Control of a Radio Telescope Receiver Supported by a Tethered Aerostat, submitted Oct 2001 for publication in *AIAA Journal of Guidance, Dynamics and Control*.

M. Nahon, G. Gilardi, C. Lambert, Control of a Radio Telescope Receiver Supported by a Tethered Aerostat, submitted Jan 2002 for presentation at *AIAA Atmospheric Flight Mechanics Conference, 2002*.

Partial Copyright License

I hereby grant the right to lend my thesis to users of the University of Victoria Library, and to make single copies only for such users or in response to a request from the Library of any other university, or similar institution on its behalf or for one of its users. I further agree that permission for extensive copying of this thesis for scholarly purposes may be granted by me or a member of the University designated by me. It is understood that copying or publication of this thesis for financial gain shall not be allowed without my written permission.

Title of Thesis:

Dynamics Modeling and Conceptual Design of a Multi-tethered Aerostat System

Author



Casey Marcel Lambert

January 25, 2002